POLITECNICO DI MILANO

Facoltà di Ingegneria

Dipartimento di Chimica, Materiali e Ingegneria Chimica "G. Natta"

Master's Degree in Chemical Engineering

CFD simulation and emissions prediction from a helicopter engine

Supervisor: Prof. Alessio FRASSOLDATI

Master's thesis of:

Gianluca MOTTA

Matr. N° 837869

Academic Year 2015-2016

Alla mia famiglia,

A chi c'è stato, a chi c'è e a chi ci sarà.

Grazie

Table of Contents

List of Figures

List of Tables

Abstract

The increasing attention on air pollution phenomena such as the direct emission of pollutants and greenhouse gases have led the political authorities to standardize air traffic emissions. The emissions from a gas turbine engine are like those coming from an internal combustion engine. Much attention is paid to the reduction of nitrogen oxides, in line with the ambitious global targets.

To achieve this objective, detailed studies of the conditions which favor the reduction of pollutants are required. The experimental tests are expensive and therefore they are often accompanied by predictive models such as Computational Fluid Dynamics (CFD) codes.

This thesis work has as primary aim to conduct the fluid dynamics simulation of a combustor used in aviation in order to predict flows, temperature fields and emissions. This activity has been carried out using Fluent and a Kinetic Post-Processor (KPP). The analyzed combustor is the RR-Allison 250 C20R model, mounted on many helicopters and small aircrafts.

An experimental campaign, done using the helicopter PZL SW-4, allowed to acquire a large set of data that was used in this work to create reliable boundary conditions and to validate the CFD results.

A 3D combustor model was created and the flow field solved adopting a RANS approach. Special attention was dedicated to the modeling of the spray, the turbulence-chemistry interactions and the fuel properties.

A very difficult challenge was to predict the emissions of CO and unburned hydrocarbons. To pursue this goal, we used a specific Kinetic Post-Processor developed at the Politecnico of Milan.

The comparison with measured emissions and temperature data have shown that the model is able to correctly characterize the combustor exit temperature and emissions as a function of engine power.

Chapter 1 – Introduction

Worldwide the aviation industry consumes about 1.5 billion barrels of traditional jet fuel annually. Although today air transport only produces 2% of man-made CO_2 emissions, this is expected to increase to 3% by 2050 with the continuous and steady traffic growth [1].

Aviation gas turbine engines have been subjected to emission regulations to limit carbon monoxide, hydrocarbon, oxides of nitrogen emissions and exhaust smoke. The NO_x requirements have become progressively more stringent over the last 20 years since EPA (Environmental Protection Agency) and ICAO (International Civil Aviation Organization) first instituted regulations respectively in 1984 and 1986 [2].

The research and development for reducing environmental impact and increasing energy efficiency of the engines requires a multidisciplinary approach with the main aviation industry partners (engine manufacturers, aircraft manufacturers and so on), the fuel industry and research organizations covering a broad spectrum of expertise in aeronautics. Important is also the possibility to carry out comparison tests in realistic conditions.

According to the CAEP (Committee on Aviation Environmental Protection), key technologies/tools that will aid in the advancement of low emissions combustion technology for gas turbines are [3]:

- Increase of the predictive accuracy, relative to current state of the art combustion CFD (Computational Fluid Dynamics) with “no tuning”, of the emissions indices and combustor performance metrics.
- Development of detailed chemical kinetic mechanisms for alternative and current hydrocarbon fuels. From such detailed schemes it is possible to derive reduced mechanisms for numerical analysis of complex combustors.

In order to verify the reliability of different approaches to reach those goals it is necessary to develop a methodology able to proof the real reduction of environmental impact in realistic condition. For this reason, flight test measurements campaigns are needed.

However, to make the results of numerical simulations and test campaign meaningful, standardization of methods and technologies has to be established.

In Clean Sky, a EU-funded research program, a dedicated subproject, Green Rotorcraft (GRC) 5, has been devoted to the development of innovative green flight paths and a specific task to develop a

predictive tool for helicopter engine emission estimation and to perform in-flight flue gas measurements [4].

The RR-Allison Model 250, which is a highly successful turbo-shaft engine family [5], has been studied in detail during the project. In fact, not only this model propels a large number of helicopters (including the Agusta A 109 and PZL SW-4) and small aircrafts, but it is important to note that the helicopter model PZL SW-4 RR250C20R2 (Figure 1.1) has been selected for an experimental campaign by the research team involved in the FP7 CLEAN-SKY project MAEM-R. Therefore, the engine Allison 250 needs to be studied to characterize the formation of pollutants as unburned hydrocarbons, which reduces the combustion efficiency and consequently increase the fuel consumption and NOx.

Figure 1.1 *Helicopter model PZL SW-4 RR250C20R2 [4]*

This analysis first requires CFD modeling of the engine and then the use of a Post-Processor to characterize the formation of CO, NO_x and unburned hydrocarbons. Due to the large number of the cells of the computational grid, this analysis takes advantage of the parallel version of the two software tools used.

1.1 Gas turbine engine

A gas turbine, also called a combustion turbine, is a type of internal combustion engine. It has an upstream rotating compressor coupled to a downstream turbine, and a combustion chamber in between [6].

We can easily resume below the basic stages for a generic turbine. Fresh atmospheric air flows through a compressor, axial or centrifugal, that brings it to higher pressure. Energy is then added by spraying fuel into the air and igniting it so that the combustion generates a high-temperature flow. This high-temperature high-pressure gas enters a turbine, where it expands till the exhaust pressure, producing a shaft work output in the process. The turbine shaft work is used to drive the compressor and other devices. The energy that is not used for shaft work remains in the exhaust gases, so these have either a high temperature or a high velocity [7].

There are different turbine engines configurations, depending on usage and power required. The main equipment, common for all types, are compressor, combustor and turbine, necessary to achieve mechanical energy by the Brayton open thermodynamic cycle (Figure 1.2).

Line 1-2 represents compression stage, 2-3 combustion, 3-4 expansion and 4-1 cooling. Numbers with apexes represent the real cycle, that is not isentropic.

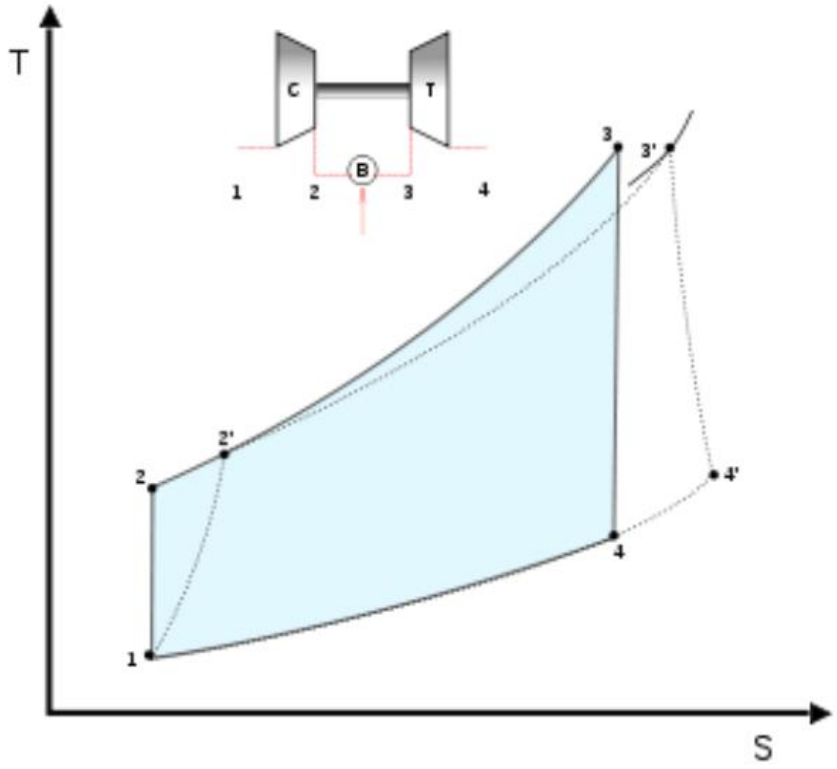

Figure 1.2 *Brayton thermodynamic cycle. Line 1-2 represents compression, 2-3 combustion, 3-4 expansion and 4-1 cooling. Numbers with apexes represent the real cycle, not isentropic [5]*

The power delivered by the turbine depends mainly on the inlet temperature, which can be varied by altering fuel/air ratio or, alternatively, by increasing compression ratio. In any case, because of resistance problems and erosion of turbine blades, it should not be exceeding a temperature of 1500 K [7]. Special materials allow to overcome this limit in specific applications.

In jet turbine engines, mainly used for passenger and goods aircraft transport or for military jet, the mechanical energy supplied by the turbine is required only to provide enough power to let the compressor and electrical equipment working, while the power required to fly is given by propulsion thrust. This thrust is obtained through the passage of exhausted gases leaving the turbine in a nozzle.

Jet engines switched from classic motors turbo-jet just described (Figure 1.3), to turbo-fan engines which, unlike the previous ones, are also equipped with one or more airscrews, positioned in the air intake inside the engine. These airscrews are necessary to circulate additional air (bypass ratio) that will be pushed directly into the nozzle so as to increase the propulsion thrust, proportional to the mass of ejected gas (m_g), using the following equation:

$$F_p = m_g(u_g - u_a) \tag{1.1}$$

Where u_g is the jet speed and u_a is the aircraft speed. The airscrews work like fans and they are connected to the drive shaft of the turbine.

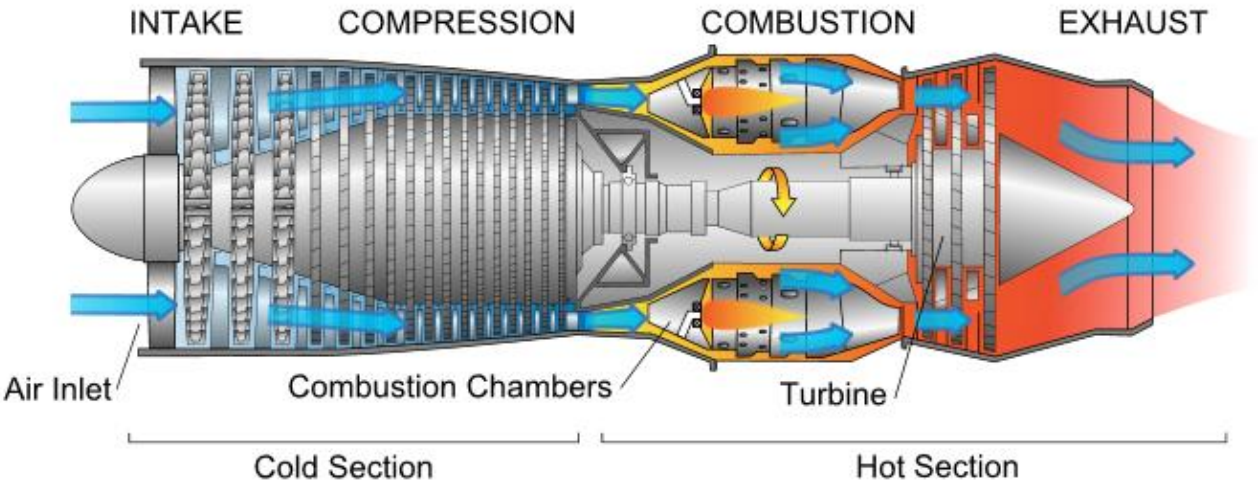

Figure 1.3 *Structure of a gas turbine engine [8]*

Turbine engines have been mainly used in large aircraft, and only from the 50's, adopted also on helicopters due to the greater power density in respect to piston engines. They allow mounting of the motor above the passenger compartment, recovering a substantial amount of space and increasing the global performance.

The energy produced by the turbine is, in a helicopter, used to spin two rotors: the main rotor and the secondary rotor, linked to a certain number of blades.

The main rotor has two types of rotation [9]:

- Parallel Rotation: blades rotate at a high speed by developing a vertical thrust, bigger and opposite to the gravitational force, which will lift the helicopter;
- Rotation angle: fast rotation of blades develops a lift which has a vertical and a horizontal thrust. In general, the rotor tilts in the direction in which it moves.

The helicopter, in reaction to the rotation of the main rotor, tends to turn in the opposite direction. So a vertical secondary rotor located in the tail develops a compensating thrust to stabilize the helicopter. The secondary rotor is also useful for rapid maneuvers (Figure 1.4).

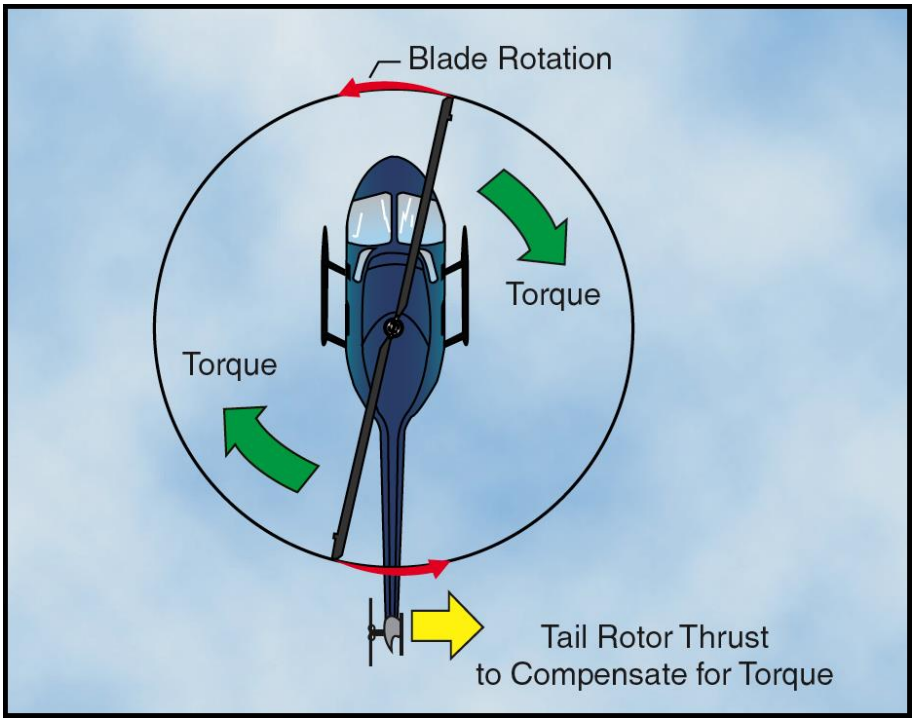

Figure 1.4 *Representation of the main and the secondary rotor movement [5]*

1.2 Framework of the Allison 250 engine

This model is one of the most successful small turbine engines ever developed. Originally grown in the early 1960s, the Allison Model 250, now known as the Rolls-Royce 250, equips over 130 different aircraft types, 80 of which are still flying today. More than 30.000 model 250 engines have been built over years with nearly 17.000 still in service today.

Originally designed to meet a military requirement for a 250 hp light turbine, the Model 250 as gone on to spawn a range of both military and civil variants with power ratings up to 715 hp [10].

An important design feature of the C20 engine was its modular construction (Figure 1.5) which greatly simplified maintenance and repair activity.

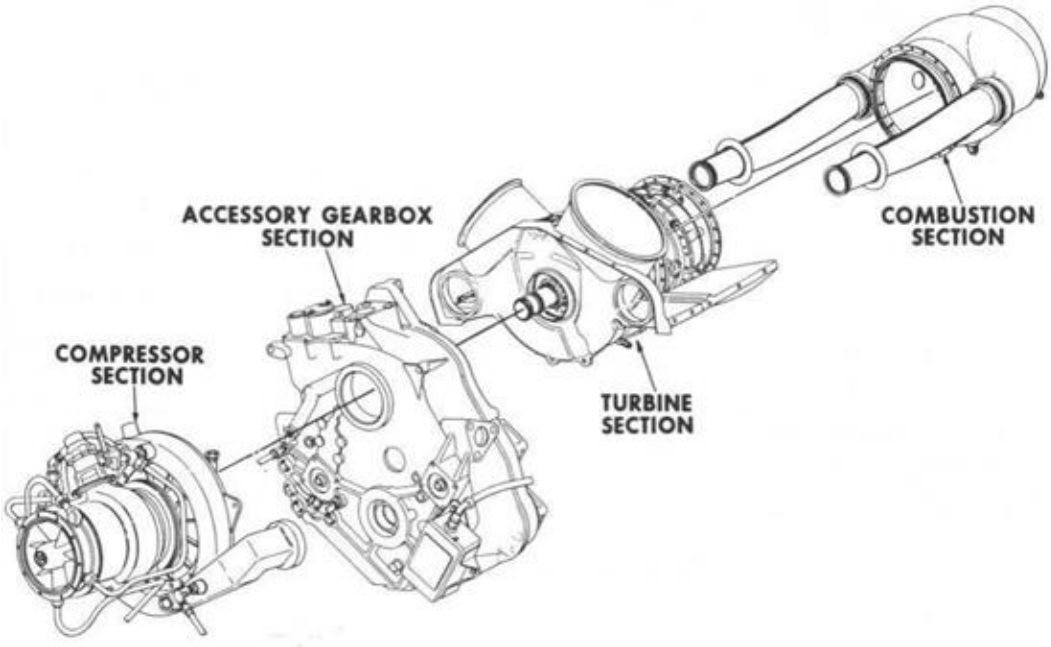

Figure 1.5 *Modular construction of the Allison 250 C20 [10]*

The specific models studied in the current thesis work are the Roll-Royce Allison 250 C20B (see the following section 1.3) and the newer version C20R; the latter is the engine used in the experimental campaign.

The C20R engine is based on the proven design of the C20B engine. The C20R model respect to the C20B one features an advanced compressor with two less stages and a higher pressure ratio.

Additional improvements include an enhanced power turbine that provides up to a five percent increase in power and a two percent reduction in specific fuel consumption. Gearbox lip-seals and shaft journals have also been improved to help reduce oil consumption [11].

These upgrades decreased the direct operating cost while increasing the value of the helicopters.

The basic engine specifications at sea level are reported in the following table (Table 1):

Model 250	C20R	C20B
Weight	173 lb (78 kg)	158 lb (72 kg)
Power	450 hp (335 kW)	420 hp (331 kW)
Airflow	3.82 lb/s (1.733 kg/s)	3.3 lb/s /1.50 kg/s)
Pressure ratio	7.9:1	7.2:1
Power output shaft	6016 rpm	6016 rpm
Power turbine rotor	34955 rpm	33290 rpm
Length	38.8 in (0.99 m)	38.8 in (0.99 m)
Diameter	20.9 in (0.53 m)	19 in (0.48 m)
Height	23.2 in (0.59 m)	22.4 in (0.57 m)
Compressor	4HP + 1 CFHP	6 HP + 1 CFHP
Turbine	2HP, 2PT	2HP, 2PT

Table 1 *C20R vs C20B engine specifications [8]*

The RR-Allison 250 is a twin spools engine with a single-can combustor located at the aft end of the engine for easy accessibility for liner, fuel nozzle and igniter maintenance or replacement during battlefield operations. As shown in Figure 1.6, the engine has a unique back-to-front combustion flow design. In addition, the unique reverse flow design provided for easy of hot section maintenance.

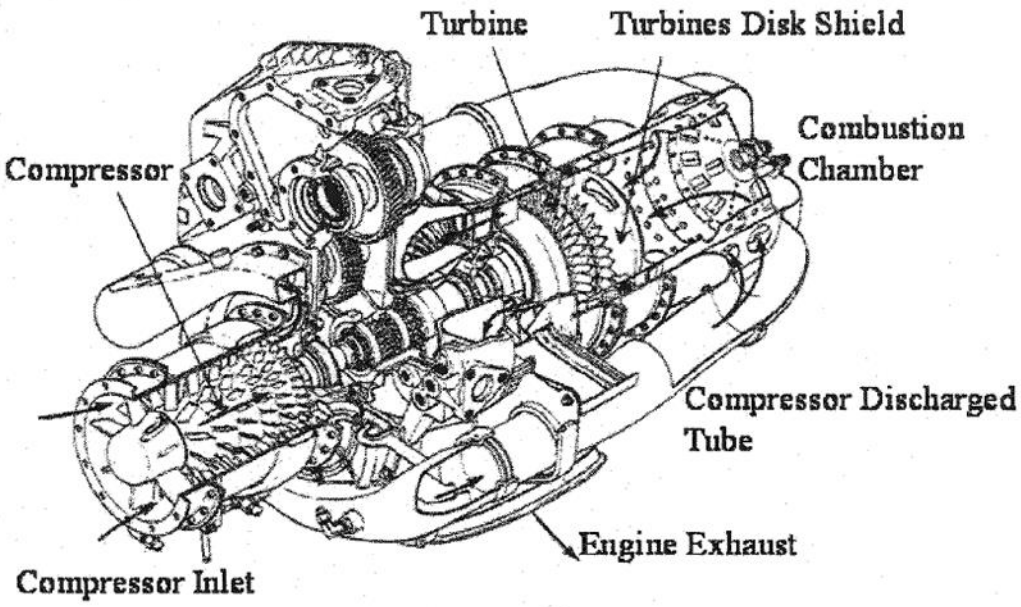

Figure 1.6 *Allison 250 C20 engine [10]*

Air enters the engine through the compressor inlet and is compressed by six axial compressor stages, as said before two less for the C20R variant. The compressed air is discharged into two ducts on both sides of the engine, which deliver the air into the single-can combustion section.

The combustion system consists of the outer casing and the combustion liner with the outlet facing the front of the engine. Air enters the combustor liner through holes in the liner dome and skin, mixed with fuel sprayed from the fuel nozzle mounted at the aft end of the engine, and combusted. Combustion hot gases move forward, expand through the two stage power turbine that is mounted in the mid-section of the engine, and air discharged through the twin ducts exhaust collector. A two-stage helical and spur gear set is used to reduce rotational speed at the power turbine from 33290 rpm (34955 for the C20R type) to 6016 rpm at the output drive spline.

The approach adopted to cool combustor liner walls is based on film cooling. Only part of the compressor air is use for the flame and the remaining is injected to cool walls by means of a film (Figure 1.7) [12]. Additional diversion of air, to primary and secondary dilution air holes, allows operation above the lean extinction limit and post-flame tailoring of the temperature profile. In this way it is also possible to control the temperature of the exhaust gases entering the turbine.

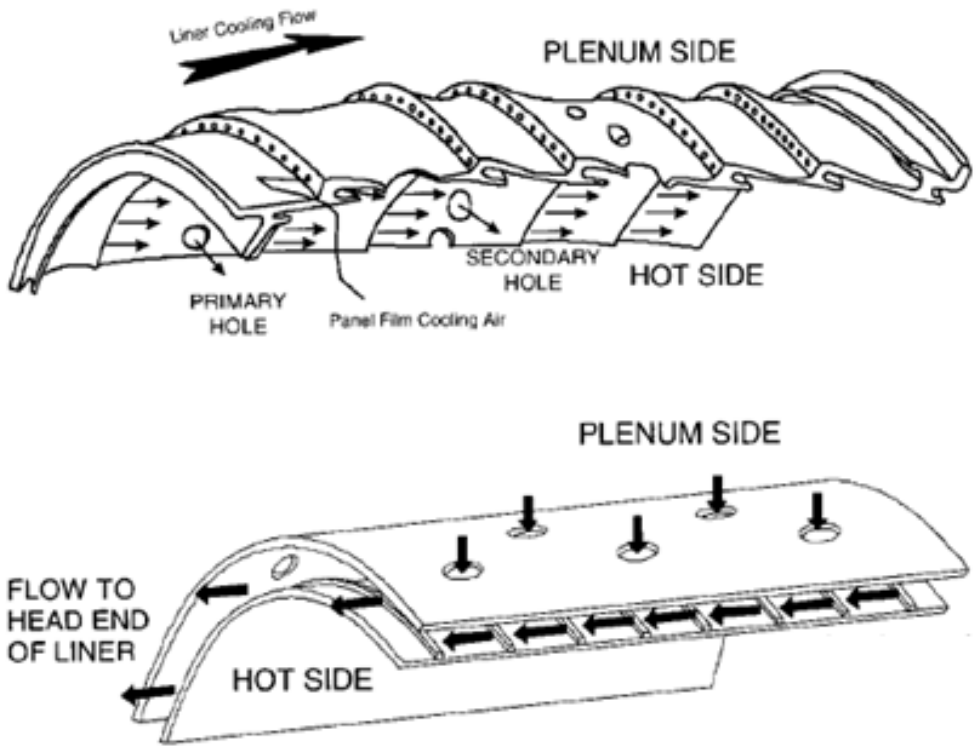

Figure 1.7 *Film-cooled and convectively cooled combustor liners [12]*

1.3 Emicopter project

The Emicopter project [4], supported by CLEAN SKY, aimed to develop an effective and predictive methodology for the prediction of NO_x in turbulent non-premixed flames of helicopter engines by using computational fluid dynamics (CFD). The work was carried out in the field of combustion kinetics, fluid dynamics, spray modeling, numerical analysis (parallel computation) and emissions evaluation. Thanks to literature analysis, it was possible to almost completely characterize the boundary conditions of the combustor for different power settings, in terms of fuel and air flow rates, air pressure, temperature and air distribution. Based on available information, a series of CFD simulations were performed to characterize temperature and flow fields.

The literature based data refers to research activity on the 250-C20B/R engine models developed respectively by Golden [13] and Hendrick [14]. Further information was collected also thanks to Islin [15] trials.

Just after the project conclusion, a campaign for collection of experimental data was completed. Therefore, it is now possible to study the emissions from helicopters equipped with the Allison 250 engine with more detail and wider range of operating conditions.

Chapter 2 – Theoretical Basis

Fluid (gas and liquid) flows are governed by partial differential equations which represent conservation laws for the mass, momentum, and energy. To better understand the CFD model used in this work, first, we analyze the mathematical and physical laws on which simulations are based. To perform our simulation, we use one of the most-powerful computational fluid dynamics software tool available: Ansys Fluent (contained inside Ansys Workbench platform).

2.1 Turbulence model

Turbulence occurs when inertia forces in the fluid become significant compared to viscous forces, and is characterized by a high Reynolds Number (2.1).

$$R_e = \frac{\rho < v > L}{\mu} \tag{2.1}$$

Where L is a characteristic linear dimension, <v> is the maximum velocity of the object relative to the fluid, ρ is the density of the fluid and μ is the dynamic viscosity of the fluid.

The Navier-Stokes equations (NS) are able to fully describe any fluid flow, even turbulent. In particular, for a turbulent flow the numerical calculation approach is generally called direct simulation.

The direct simulation is preferable to modeling but the barriers are insurmountable for complicated, dense meshes which are necessary in order to resolve the range of length and time scales that exist in a fully turbulent flow, even more with the added complexity of chemical reactions. The NS equations are then used in their time-averaged or ensemble-averaged form, which gives rise to extra 'Reynolds stress' terms which require modeling in order to 'close' the set of equations that describe the turbulent flow field [16].

So, there are three types of approaches to solve the NS equations in turbulent regime:

- DNS (Direct Numerical Simulation): Conservation equations are solved without any kind of simplification. In order to apply this approach, it is necessary to follow all the scales of

evolution of turbulent eddies, achievable only with the use of very dense grids. It is a very expensive method in terms of calculation time and with little applicative interest;

- LES (Large Eddy Simulation): The scales of the smallest vortices are modeled by appropriate closing terms, while the scales of the largest ones are resolved directly;

- RANS (Reynolds Average Navier Stokes): Conservation equations are solved in their averaged form. The effect of turbulence is entirely modeled through the use of suitable turbulence closure models.

Despite the simplifications, RANS turbulence models are able to provide good results with reasonable calculation time and so are the only used in this thesis work. A brief description is contained in the following paragraph.

2.1.1 RANS model

The Reynolds-Averaged-Navier–Stokes equations (or RANS equations) are time-averaged equations of motion for fluid flow.

RANS turbulence models are accurate for simple flows and can give reasonably good predictions of the main flow characteristics such as pressure fields, temperature and speed. However, the disadvantages of empiricism involved in the formulation of these models, the defects of the one size-fits-all simulations approach have become clear and clear as the level of resolution required increased due to the need for accuracy at very low levels, for example, chemical species predictions, turbulence intensities, scalar dissipation rates, etc [17].

To a first approximation, RANS turbulence models split the flow field into a “mean” part and a “fluctuating” part, and a statistical model is used in conjunction with the assumption of an isotropic turbulent eddy viscosity and thus closes the Reynolds stress terms in the Navier Stokes Equations.

RANS turbulence models deal with the issue of closure of the stress terms in the NS equations by making simplifying assumptions such as the Boussinesq hypothesis (used in several 'two-equation'

models such as the k-ε, k-ω types). The Boussinesq assumption simply postulates that the momentum transfer, caused by turbulent eddies, can be modeled with an eddy viscosity.

Two equation turbulence models are one of the most common types of turbulence models. Models like the k-ε model and the k-ω model have become industry standard models and are commonly used for most types of engineering problems. Two equation turbulence models are also still an active area of applied research and new refined two-equation models are still being developed. By definition, two equation models include two extra transport equations to represent the turbulent properties of the flow. This allows models to account for effects like convection and diffusion of turbulent energy [18].

A brief description of standard k-ε model (without reactions, body forces and gravitational effects) is shown below as used in Fluent, version 16.2.

The Continuity Equation:

$$\frac{\partial}{\partial x_i}(\rho u_i) = S_m \tag{2.2}$$

The Navier Stokes Equations:

$$\frac{\partial}{\partial t}(\rho u_i) + \frac{\partial}{\partial x_j}(\rho u_i u_j) = \frac{\partial}{\partial x_j}\left(\mu \frac{\partial \tau_{ij}}{\partial x_j}\right) - \frac{\partial p}{\partial x_i} \tag{2.3}$$

where the Boussinesq assumption is used to model the stress tensor, τ_{ij}.

$$\tau_{ij} = \left[\mu\left(\frac{\partial u_i}{\partial x_j} + \frac{\partial u_j}{\partial x_i}\right)\right] - \frac{2}{3}\mu \frac{\partial u_I}{\partial x_I} I \tag{2.4}$$

Turbulent Kinetic Energy:

$$\frac{\partial}{\partial t}(\rho k) + \frac{\partial}{\partial x_i}(\rho k u_i) = \frac{\partial}{\partial x_j}\left(\left(\mu + \frac{\mu_t}{\sigma_k}\right)\frac{\partial k}{\partial x_j}\right) + G_k + G_b - Y_M + S_k \tag{2.5}$$

Eddy Dissipation Rate (the rate of turbulent kinetic energy dissipation):

$$\frac{\partial}{\partial t}(\rho\varepsilon) + \frac{\partial}{\partial x_i}(\rho\varepsilon u_i) = \frac{\partial}{\partial x_j}\left(\left(\mu + \frac{\mu_t}{\sigma_\varepsilon}\right)\frac{\partial \varepsilon}{\partial x_j}\right) + C_{1\varepsilon}\frac{\varepsilon}{k}(G_k + C_{3\varepsilon}G_b) - C_{2\varepsilon}\rho\frac{\varepsilon^2}{k} + S_\varepsilon \quad (2.6)$$

The Turbulent Viscosity, μ_t, is modeled as:

$$\mu_t = C_\mu \rho \frac{k^2}{\varepsilon} \quad (2.7)$$

which assumes the "linear" nature of the eddy viscosity.

Several constants that are required for this model:

$C_{1\varepsilon}$, $C_{2\varepsilon}$, $C_{3\varepsilon}$, C_μ, σ_k, σ_ε take values of 1.44, 1.92, 0.09, 1.0, 1.3 respectively.

One of the main objections to using this turbulence model is its inherent tendency to overestimate the turbulent diffusion, especially in the presence of heat released, failing to accurately capture the physics of the flow [19].

There are variants of this model, notably, the realizable k-ε model by Shih [20] which is much more accurate in predicting flows with streamline curvature and recirculation and the RNG k-ε model, developed by Yahkot and Orszag [21], grown from first principles using renormalization group theory, which can include swirl effects.

The realizable k−ε model is just an improvement over the standard k−ε model and is what we have chosen for this thesis work due to his superior ability to capture the mean flow of the complex structures, in accordance with Shih [20].

The realizable k−ε model contains a new formulation for the turbulent viscosity and a new transport equation for the dissipation rate, ε, that is derived from an exact equation for the transport of the mean-square vorticity fluctuation. The term "realizable" means that the model satisfies certain mathematical constraints on the Reynolds stresses, consistent with the physics of turbulent flows.

The transport equation for the turbulent kinetic energy dissipation rate is reproduced below:

$$\frac{\partial}{\partial t}(\rho\varepsilon) + \frac{\partial}{\partial x_j}(\rho\varepsilon u_j) = \frac{\partial}{\partial x_j}\left(\left(\mu + \frac{\mu_t}{\sigma_\varepsilon}\right)\frac{\partial \varepsilon}{\partial x_j}\right) + \rho C_1 S\varepsilon - C_2\rho\frac{\varepsilon^2}{k+\sqrt{v\varepsilon}} + G_{1\varepsilon}\frac{\varepsilon}{k}C_{3\varepsilon}G_b + S_\varepsilon \quad (2.8)$$

Where:

$$C_1 = \max\left[0.43\frac{\eta}{\eta+5}\right] \tag{2.9}$$

$$\eta = S\frac{k}{\varepsilon}\ and\ S = \sqrt{2S_{ij}S_{ij}} \tag{2.10}$$

However, the C_μ term is now variable (unlike in the standard k-ε model, where it is constant at 0.09 from an empirical value taken from equilibrium boundary layers) and is a function of "the mean strain and rotation rates, the angular velocity of the system rotation", and the turbulence fields (k and ε) and is computed from:

$$C_\mu = \frac{1}{A_0 + A_S\frac{kU^*}{\varepsilon}} \tag{2.11}$$

$$U^* = \sqrt{S_{ij}S_{ij} + \Omega'_{ij}\Omega'_{ij}} \tag{2.12}$$

$$\Omega'_{ij} = \Omega_{ij} - 2\varepsilon_{ijk}\omega_k \tag{2.13}$$

$$\Omega_{ij} = \Omega^{average}{}_{ij} - 2\varepsilon_{ijk}\omega_k \tag{2.14}$$

$$A_0 = 4.04\ and\ A_S = \sqrt{6}\cos\phi \tag{2.15}$$

$\Omega^{average}{}_{ij}$ is the mean rate-of-rotation tensor with angular velocity ω_k and:

$$\phi = \frac{1}{3}\cos^{-1}(\sqrt{6}\,W) \tag{2.16}$$

$$W = \frac{S_{ij}S_{jk}S_{ki}}{S'^3} \tag{2.17}$$

$$S' = \sqrt{S_{ij}S_{ij}} \tag{2.18}$$

$$S_{ij} = \frac{1}{2}\left(\frac{\partial u_j}{\partial x_i} + \frac{\partial u_i}{\partial x_j}\right) \tag{2.19}$$

2.2 Spray model

Sprays belong to a specific type of two-phase flows which are characterized by a dominating direction of motion and involve liquid phase in a discrete form of droplets and/or ligaments and the gas phase as the continuum. Regardless of applications, sprays are the results of high pressure-driven liquid jets injected through one or several injector nozzle orifices into a combustion chamber. The jet atomizes into different liquid fragments, and, finally, into droplets, which evaporate producing vapor which mixes with oxidizer (air) forming a combustible mixture which burns and sustains the combustion process [22].

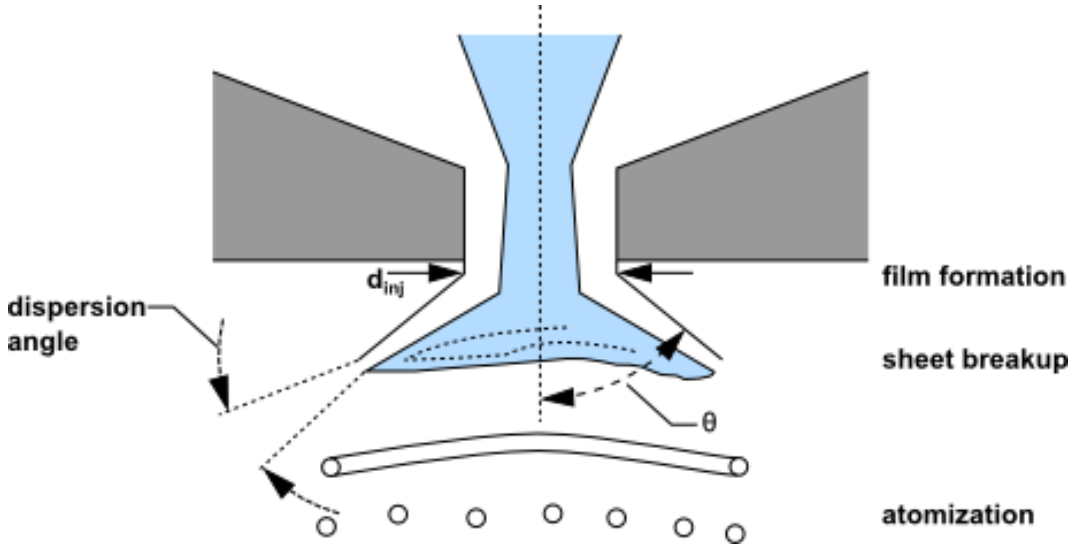

Figure 2.1 *Simple sketch of the theoretical progression from the Internal atomizer flow to the external spray [23]*

Most of the spray models are based on what can be called “kinetic approach”, in the form of Boltzmann type spray equation for probability droplet number density function [24]. At this level, the connection between Lagrangian particle methods based on the ensemble average and the Eulerian spray equation based on the space or time average is straightforward [25].

Since the spatial resolution on a scale comparable to a droplet size is impossible, there is no way to know exact droplet locations at each moment of time and only a probabilistic approach is relevant to the problem. In term of this approach, the spray is constituted of spherical droplets characterized by e.g., one geometry parameter $\phi=\alpha R^{\alpha}$, one velocity u_l and one temperature T_l, and can be described by a distribution function f^{ϕ}, so that it is possible to calculate the probable number of droplets at time t in the phase elementary volume. By definition, ϕ can be the droplet radius, the droplet surface or the droplet volume.

The distribution function satisfies the "kinetic type" transport equation:

$$\partial_t f^{\phi} + \partial_x\left(u_i f^{\phi}\right) + \partial_{u_l}\left(F_{l,i} f^{\phi}\right) + \partial_{\phi}\left(R_{\phi} f^{\phi}\right) + \partial_{T_l}(T_l f^{\phi}) = \Gamma + Q \tag{2.20}$$

where F is the drag force applied by gas on the droplet, R is the rate of change of the droplet size caused by evaporation, T is the heat exchange rate between two phases, Γ and Q stand for single (breakup) and binary (collision) processes.

The characteristics of the partial differential equation of hyperbolic type, Eq. (2.20), defining particle paths in the phase space, are given by:

$$\frac{\partial x_i^{(\phi)}}{\partial t} = u_{l,i} \tag{2.21}$$

$$\frac{\partial u_{l,i}^{(\phi)}}{\partial t} = F_{l,i} \tag{2.22}$$

$$\frac{\partial r^{(\phi)}}{\partial t} = R_{\phi} \tag{2.23}$$

$$\frac{\partial T_l^{(\phi)}}{\partial t} = T_{l,\phi} \tag{2.24}$$

The gas and liquid phases are coupled through the dependence of $F_{l,i}$, R_{ϕ} and $T_{l,\phi}$ on the local gas velocity, composition and temperature. These variables are the time rates of change attributed to the individual droplet, to its velocity, radius, etc.

2.2.1 Collision model

The difficulty in any collision calculation is that for N droplets, each droplet has N-1 possible collision partners. Thus, the number of possible collision pairs is approximately $\frac{1}{2}N^2$. The factor of ½ appears because droplet A colliding with droplet B is identical to droplet B colliding with droplet A. This symmetry reduces the number of possible collision events by half.

An important consideration is that the collision algorithm must calculate $\frac{1}{2}N^2$ possible collision events at every time step. Since a spray can consist of several million droplets, the computational cost of a collision calculation from first principles is prohibitive. This motivates the concept of parcels. Parcels are statistical representations of a number of individual droplets. Because the cost

of the collision calculation still scales with the square of N, the reduction of cost is significant; however, the effort to calculate the possible intersection of so many parcel trajectories would still be prohibitively expensive.

The algorithm of O'Rourke [26] efficiently reduces the computational cost of the spray calculation. Rather than using geometry to see if parcel paths intersect, O'Rourke's method is a stochastic estimate of collisions. O'Rourke also makes the assumption that two parcels may collide only if they are located in the same continuous-phase cell. These two assumptions are valid only when the continuous-phase cell size is small compared to the size of the spray.

The concept of parcels together with the algorithm of O'Rourke makes the calculation of collision possible for practical spray problems.

Once it is decided that two parcels of droplets collide, the algorithm further determines the type of collision. Only coalescence and bouncing outcomes are considered. The probability of each outcome is calculated from the collisional Weber number (We_c) and a fit to experimental observations.

$$We_c = \frac{\rho U_{rel}^2 \overline{D}}{\sigma} \tag{2.25}$$

where U is the relative velocity between two parcels and $\overline{D}$ is the arithmetic mean diameter of the two parcels. The state of the two colliding parcels is modified based on the outcome of the collision.

2.2.2 Breakup model

There are two droplet breakup models available in the Fluent code: the Taylor analogy breakup (TAB) model and the wave model. The TAB model is recommended for low-Weber-number injections and is well suited for low-speed sprays into a standard atmosphere. For Weber numbers greater than 100, the wave model is more applicable. The wave model is popular for use in high-speed fuel-injection applications. Details for each model are provided below.

The Taylor analogy breakup (TAB) model is a classic method for calculating droplet breakup, which is applicable to many engineering sprays. This method is based upon Taylor's analogy [27] between an oscillating and distorting droplet and a spring mass system.

The resulting TAB model equation set, which governs the oscillating and distorting droplet, can be solved to determine the droplet oscillation and distortion at any given time. When the droplet oscillations grow to a critical value the "parent" droplet will break up into a number of smaller "child" droplets. As a droplet is distorted from a spherical shape, the drag coefficient changes.

As said before, the TAB model is best for low Weber-number sprays. Extremely high Weber number sprays result in shattering of droplets, which is not described well by the spring-mass analogy.

An alternative to the TAB model that is appropriate for high Weber number flows is the wave breakup model of Reitz [28], which considers the breakup of the droplets to be induced by the relative velocity between the gas and liquid phases. The model assumes that the time of breakup and the resulting droplet size are related to the fastest-growing Kelvin-Helmholtz instability, derived from the jet stability analysis described below. The wavelength and growth rate of this instability are used to predict details of the newly-formed droplets.

The wave model is appropriate for high-speed injections, where the Kelvin-Helmholtz instability is believed to dominate droplet breakup (We_c >100). Because this breakup model can increase the number of computational parcels, you may wish to inject a modest number of droplets initially.

If the breakup and collisional processes in Eq. (2.20) are neglected, the model describes so-called thin sprays.

In accordance with Lee [29], the TAB model has been used due to his superior capacity to correctly represent particles break up behavior in liquid jet injection.

2.3 Drag model

In fluid dynamics, drag refers to forces acting on a body in the direction relative to the speed. Especially in the dense area of the spray it is not easily determined [30]. In general, the coefficient C_d decreases if compared with a single particle and can be related with the void fraction. It is also reasonable to assume that C_d varies in presence of an evaporating particle because of changes of the flow field, precisely given by the outlet material flow. Moreover, in presence of combustion the viscosity of the flue gas is lower than that of air at the same temperature, this factor can influence drag too.

The drag can be of two types:

- Pressure-drag: The shape and dimensions of the object are the most important parameters. The greater is the impact area with the dispersed phase and greater is the force that opposes the motion. This force increases with the square of speed and so, obviously, is significant at high speeds;
- Skin-fraction: It grows with increasing interaction between the gaseous fluid and the liquid interface.

The drag coefficient is very dependent on the shape of particles, which tends to change along the path due to the interaction of particle with the gaseous phase. It is possible to take account of changes of the shape of particles on the calculation of drag coefficient by the following relationship, in which aerodynamic resistance value varies linearly between lower (sphere) and upper (disc) limit values [31]:

$$C_d = C_{d,sphere}(1 + C_{dist}y) \tag{2.26}$$

C_{dist} is a constant value equal to 2.63 while y is the dimensionless deviation.

The particle shape may significantly deviate from spherical shape, approaching in the most extreme case the disc shape.

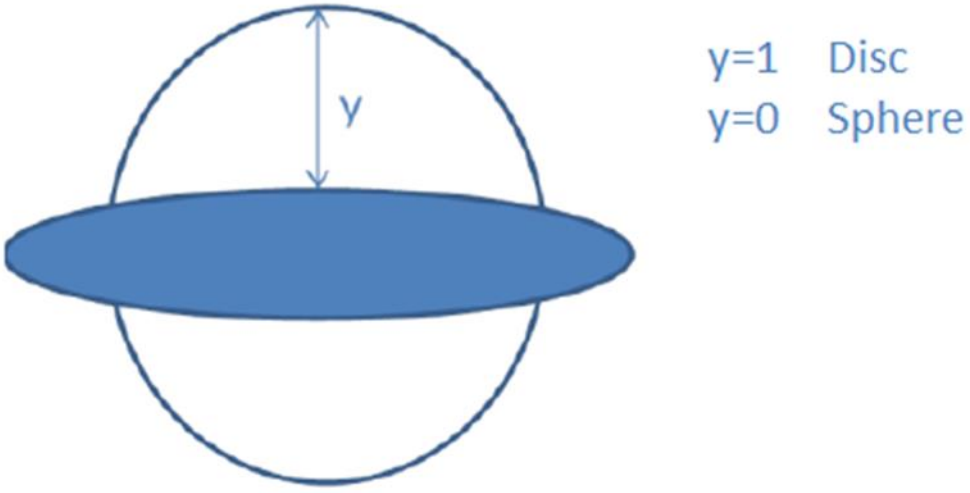

Figure 2.2 *Deviation from the spherical shape of a particle placed in a gaseous flow. Y indicate the dimensionless deviation*

At the end, we it possible to affirm that the drag force is proportional to the difference between gas velocity and particle velocity:

$$F_{drag} = C_D \cdot (u - u_{particle}) \tag{2.27}$$

2.4 Evaporation model

Several phenomena affect the evaporation of a spray particle: heat and mass exchange between liquid and gas phase have to be taken into account, as sketched in Figures 2.3 and 2.4.

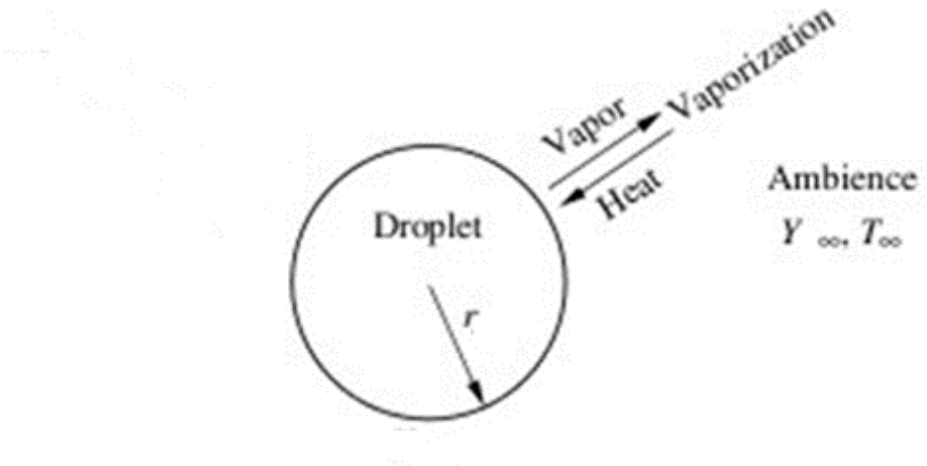

Figure 2.3 *Heat and mass exchange between the liquid and the gas phase [32]*

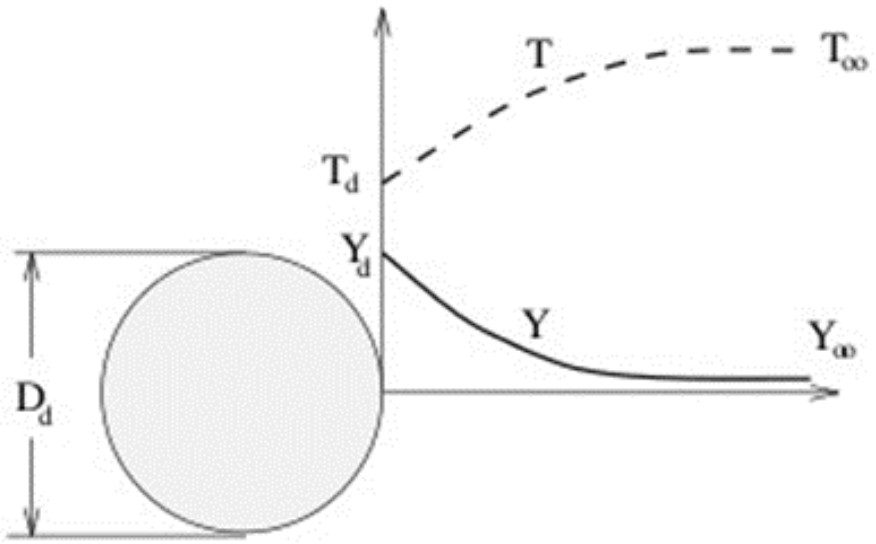

Figure 2.4 *T and Y changing along the particle [32]*

Evaporation of the fluid is calculated by the CFD code on the basis of chemical-physical properties such as vapor pressure of the fluid and its boiling temperature. The liquid droplet evaporation rate depends on local gas phase conditions and droplet temperature. Different evaporation laws are used accordingly. In the following, equations used are described.

The model always assumes a state of uniform temperature within the droplet. In general, the temperature of the droplet is calculated using an enthalpy balance which takes into account heat transfer (convective and radiative) and latent heat of evaporation:

$$m_p C_p \frac{dT_p}{dt} = hA_p\left(T_\infty - T_p\right) + \frac{dm_p}{dt} h_{fg} + A_p \varepsilon_p \sigma\left(\theta_R^4 - T_p^4\right) \tag{2.28}$$

Heat transfer coefficient is evaluated using Ranz and Marshall [32] correlation:

$$Nu = \frac{hd_p}{k_\infty} = 2 + 0.60 {Re_d}^{1/2} Pr^{1/3} \tag{2.29}$$

An evaporation law is used when the temperature of the droplet is lower than the boiling point. Evaporation is limited by diffusion in the gas phase, which is proportional to the concentration gradient between the surface of the droplet and the "bulk" of the gas phase.

$$N_i = k_c\left(C_{i,s} - C_{i,\infty}\right) = k_c C_{tot}\left(Y_{i,s} - Y_{i,\infty}\right) \tag{2.30}$$

Vapor concentration at the interface between the droplet and the gas phase is calculated assuming that its partial pressure is equal to the vapor pressure at the temperature of the liquid droplet.

$$C_{i,s} = \frac{P_{sat}(T_p)}{RT_p} \tag{2.31}$$

Where R is the gas constant, T_p is the droplet temperature and P_{sat} is the saturation pressure calculated at the droplet temperature.

The bulk concentration in the gas phase depends on cell local composition which contains the droplet.

The material transfer coefficient is calculated by the Sherwood number:

$$Sh_{AB} = \frac{k_c d_p}{D_{i,mix}} = 2 + 0.60 {Re_d}^{1/2} Sc^{1/3} \tag{2.32}$$

Finally, a boiling law (boiling droplet) is applied when the temperature of the droplet reaches the boiling point:

$$-\frac{d(d_p)}{dt} = \frac{2}{\rho_p h_{fg}} \left[\frac{2k_\infty \left(1 + 0.23\sqrt{\mathrm{Re}_d}\right)}{d_p} \left(T_\infty - T_p\right) + \varepsilon_p \sigma \left(\theta_R^4 - T_p^4\right) \right] \tag{2.33}$$

2.5 Combustion model

Combustion is defined as a chemical reaction in which a hydrocarbon fuel reacts with an oxidant to form products, accompanied with the release of energy in the form of heat.

The mixing between oxidant and fuel in the domain controls the decision of which model can be applied. Combustion modeling has seen approaches that seek to focus on perfectly premixed combustion, non-premixed combustion as well as models applicable to the more challenging situation of partially-premixed combustion.

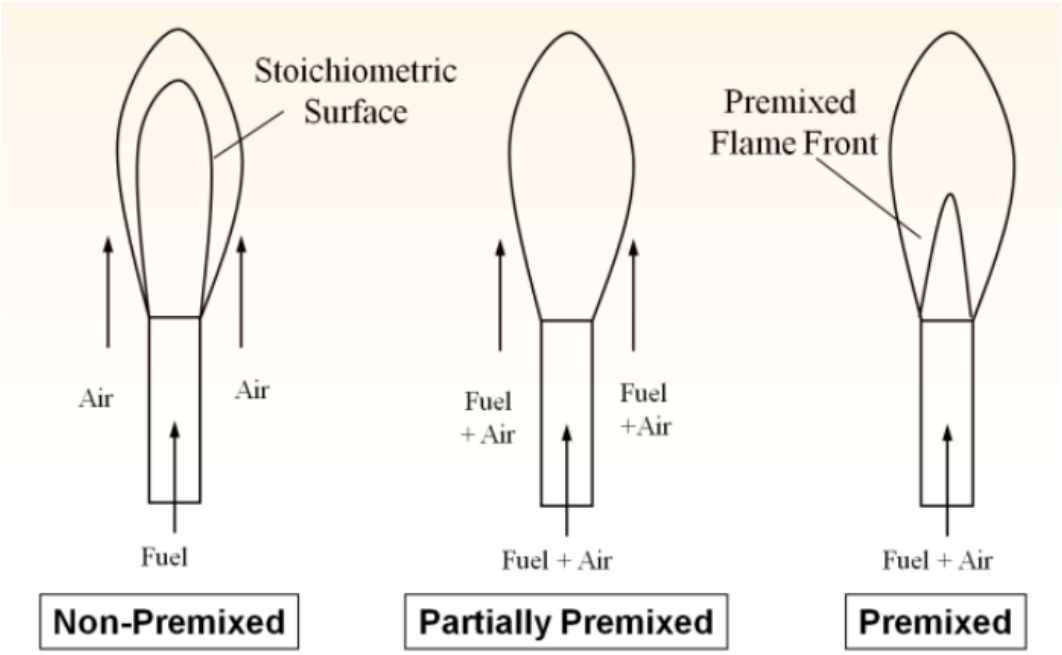

Figure 2.5 *Non-Premixed, Partially Premixed and Premixed flames [33]*

Similar to the turbulence closure problem for the Reynolds stresses, combustion modelers face a closure problem for the chemical source term in the species mass fraction transport equation, which accounts for the convection, diffusion, production and destruction of chemical species formed as a result of the reactions.

A further complexity, is the introduction of widely varying chemical timescales due to species reaction rates ranging from very fast to very slow. Still aggravating, is the chemical process itself, which does not work through single step global reactions, but must proceed through often hundreds of intermediate reaction steps, that involve typically hundreds of radicals and molecules.

The reaction rate is directly influenced by the mixing processes and thus dependent on very accurate predictions of turbulence. The standard way of dealing with the chemistry effects, with the least amount of modeling, is to introduce a general scalar transport equation for each of the species and attempt to model the source term. This is clearly impossible due to the number of species involved and further modeling is necessary to bring down the "dimensionality" of the problem with simplifying assumptions such as infinitely fast chemistry.

Often a good combustion model works very poorly due to incorrect modeling of the main mixing regions. The solution is to keep boundary conditions far away from the region of interest, as well as have a well-validated cold flow prediction prior to a reacting flow simulation [17].

Hence, the following discussion presents a general outline of the various models adopted in this thesis work that involves mainly the use of non-premixed combustion.

2.5.1 Species transport

We used this model just in early stages to analyze the mesh sensitivity but we want likewise to describe briefly how it works.

This model solves the conservation equations for convection, diffusion, and reaction sources for multiple component species.

$$\frac{\partial}{\partial t}(\rho Y_i) + \nabla(\rho v Y_i) = -\nabla J_i + R_i + S_i \tag{2.34}$$

This conservation equation describes the convection and diffusion of the local mass fraction of a species Y_i.

R_i is the rate of production by chemical reaction, and S_i is the rate of creation by addition from the dispersed phase and user-defined sources. R_i also considers turbulence-chemistry interactions.

The diffusion flux J_i occurs due to gradients of concentration and temperature. Fick's law is the default:

$$J_i = -\rho D_{i,m} \nabla Y_i - D_{T,i} \frac{\nabla T}{T} \tag{2.35}$$

where $D_{i,m}$ is the mass diffusion coefficient and $D_{T,i}$ is the thermal diffusion coefficient. This approximation is generally good.

With turbulence, further accommodation is necessary because mixing must be explicitly included as a function of turbulence at small length scales.

$$J_i = -(\rho D_{i,m} + \frac{\mu_t}{S_{ct}}) \nabla Y_i - D_{T,i} \frac{\nabla T}{T} \tag{2.36}$$

Naturally, multicomponent transport introduces a number of significant physical effects into the system, including diffusion, enthalpy transport, and temperature gradients.

2.5.2 Non-Premixed

In non-premixed combustion, fuel and oxidizer enter the reaction zone in distinct streams. This is in contrast with premixed systems, in which reactants are mixed at the molecular level before burning.

Under certain assumptions, the thermochemistry can be reduced to a single parameter: the mixture fraction [34]. The mixture fraction, denoted by *f,* is the mass fraction that originated from the fuel stream. In other words, it is the local mass fraction of burnt and unburnt fuel stream elements (C, H, etc.) in all the species (CO_2, H_2O, O_2, etc.).

In turn, the mixture fraction is a conserved scalar quantity, and therefore its governing transport equation does not have a source term. Combustion is simplified to a mixing problem, and the

difficulties associated with closing non-linear mean reaction rates are avoided. Once mixed, the chemistry can be modeled as in chemical equilibrium (not in our case), or near chemical equilibrium with the laminar flamelet model. Interaction of turbulence and chemistry is accounted for with a probability density function (PDF).

2.5.2.1 Probability density function (PDF)

The pdf transport model should be used when you are interested in simulating finite-rate chemical kinetic effects in turbulent reacting flows. With an appropriate chemical mechanism, kinetically-controlled species such as CO and NO_x, as well as flame extinction and ignition, can be predicted. Pdf transport simulations are computationally very expensive.

It is possible to account for the effects of intermediates and radical species on the main temperature field, by considering their instantaneous fractions to be linear functions of a conserved scalar which simply is a measure of the local equivalence ratio. The diffusion of all species is assumed to be equal, implying a Lewis number of unity. In such a case, only the mean and variance of this scalar, *f*, needs to be calculated. The mean mass fraction of the species in question is found by weighting the integral with the probability of *f* occurring with a specific value during a specific period of time. The probability considered, defined by an assumed-shape probability density function of the samples (fluctuations), is shown below (Figure 2.6).

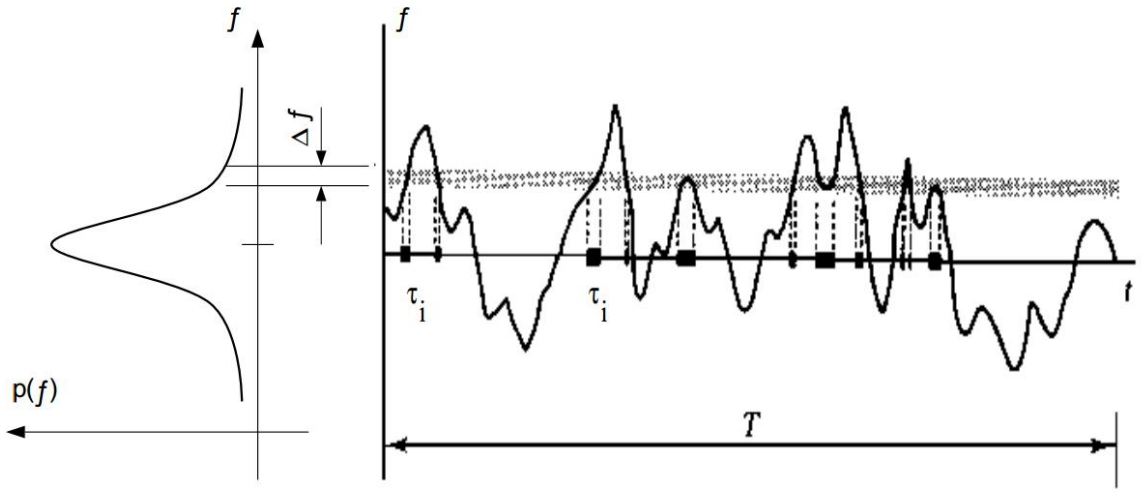

Figure 2.6 *Graphical description of the Probability Density Function, p(f). The fluctuating value of f, plotted on the right side of the figure, spends some fraction of time in the range denoted as Δf. p(f), plotted on the left side of the figure, takes on values such that the area under its curve in the band denoted, Δf, is equal to the fraction of time that f spends in this range [34]*

A great saving in computational effort is achieved, due to the nature of obtaining these mass fractions by creating a look-up table of these values, prior to the solution run-time [33]. At run time, the mean species mass fractions are calculated by looking up this table and interpolating accordingly as values of the mean, variance of *f* are obtained from their transport equations. If there are heat losses/gains to the system, the mass fraction of the species is a function of the enthalpy too. In which case a transport equation for the enthalpy, rather than the usual energy equation, is solved. Results are shown in a three-dimensional look-up table (Figure 2.7).

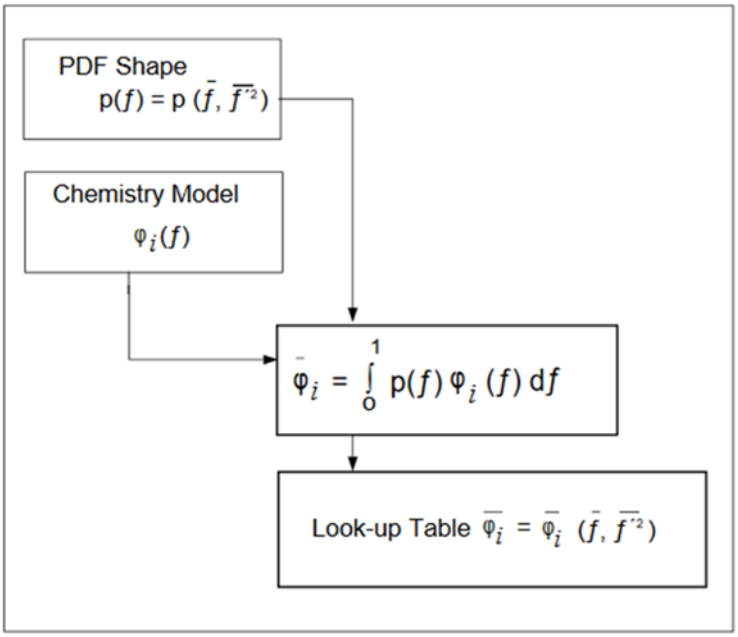

Figure 2.7 *The loop used to calculate the mass fraction of specie i as a function of mean variance and enthalpy [34]*

2.5.2.2 Mixture fraction

The mixture fraction can be defined in various ways [35], however the Fluent implementation states it to be the "elemental mass fraction that originated from the fuel stream".

$$f = \frac{Z_i - Z_{i,ox}}{Z_{i,fuel} - Z_{i,ox}} \tag{2.37}$$

The mixture fraction is directly related to the local equivalence ratio, ϕ, as:

$$f = \frac{\phi}{\phi + r} \; and \; \phi = \frac{FAR}{FAR_{stoich}} \tag{2.38}$$

where FAR stands for Fuel-Air Ratio and r is the number of moles of oxidizer required for stoichiometric burning of the fuel.

In a turbulent flow, the diffusion due to turbulence is assumed to overcome the diffusion due to material (molecular) diffusivity. This enables to use the simplifying assumption of equal diffusivities for all species and thus reduce the species equations to a single equation for the mixture fraction

The equations that describes the transport of the mixture fraction and its variance are defined as:

$$\frac{\partial}{\partial t}\left(\rho\,\overline{\mathrm{f}}\,\right)+\nabla\left(\rho v\,\overline{\mathrm{f}}\,\right)=\nabla\left(\frac{\mu_t}{\sigma_t}\nabla\,\overline{\mathrm{f}}\,\right) \tag{2.39}$$

$$\frac{\partial}{\partial t}\left(\rho\,\overline{\mathrm{f}}^{\,2}\right)+\nabla\left(\rho v\,\overline{\mathrm{f}}^{\,2}\right)=\nabla\left(\frac{\mu_t}{\sigma_t}\nabla\,\overline{\mathrm{f}}\,\right)+C_g\left(\nabla\,\overline{\mathrm{f}}\,\right)-{C_d}^2\rho\frac{\varepsilon}{k}\,\overline{\mathrm{f}}^{\,2} \tag{2.40}$$

Where σ_t, C_g and C_d are constants that take default values of 0.85, 2.86 and 2.0 respectively. σ_t, is the turbulent Schmidt number.

The probability density function that describes the fluctuations of the mixture fraction is defined in non-adiabatic equation for density-weighted species mass fraction, ϕ_i

$$\overline{\Phi}_{\,i}=\int_0^1 p(f)\phi_i\left(f,\,\overline{\mathrm{H}}\,\right)\mathrm{df} \tag{2.41}$$

Where:

$$p(f)=\frac{f^{\alpha-1}(1-f)^{\beta-1}}{\int f^{\alpha-1}(1-f)^{\beta-1}df} \tag{2.42}$$

$$\alpha=\overline{\mathrm{f}}\left[\frac{\overline{\mathrm{f}}\left(1-\overline{\mathrm{f}}\right)}{\overline{\mathrm{f}}^{\,2}}-1\right] \tag{2.43}$$

$$\beta=\left(1-\overline{\mathrm{f}}\right)\left[\frac{\overline{\mathrm{f}}\left(1-\overline{\mathrm{f}}\right)}{\overline{\mathrm{f}}^{\,2}}-1\right] \tag{2.44}$$

The transport equation of mean enthalpy is given by:

$$\frac{\partial}{\partial t}\left(\rho\,\overline{\mathrm{H}}\,\right)+\nabla\left(\rho v\,\overline{\mathrm{H}}\,\right)=\nabla\left(\frac{k_t}{C_p}\nabla\,\overline{\mathrm{H}}\,\right)+S_h \tag{2.45}$$

2.5.2.3 Flamelet

The flamelet concept considers the turbulent flame as an aggregate of thin, laminar (Re<2000), locally one-dimensional flamelet structures present within the turbulent flow field. Counterflow diffusion flame is a common laminar flame which is used to represent a flamelet in a turbulent flow. Its geometry consists of opposed and axi-symmetric fuel and oxidizer jets. As the distance between the jets is decreased and/or the velocity of the jets is increased, the flame is strained and departs from its chemical equilibrium until it eventually extinguishes. The mass fraction of species and temperature fields can be measured or calculated in laminar counterflow diffusion flame experiments. When calculated, a self-similar solution exists, and the governing equations can be simplified to only one dimension i.e. along the axis of the fuel and oxidizer jets. It is in this direction where complex chemistry calculations can be performed affordably.

Non-equilibrium phenomena, due to aerodynamic strain, can be incorporated into the pdf model by assuming combustion to take place in thin one-dimensional and time-dependent layers called “flamelets” by Peters [36] which make up the turbulent flame brush. A non-dimensional number, the Damkohler (Da), exists to relate the timescales of diffusion and chemical kinetics as a ratio. It expresses the ratio between the characteristic mixing time and the characteristic time of the chemical.

$$Da=\frac{\tau_{mix}}{\tau_c} \tag{2.46}$$

Peters [36] used asymptotic methods to expand the Da of the rate determining reaction (of the multi-step kinetics) and proved that this assumption is valid. An additional variable, the mixture fraction scalar dissipation rate, is introduced to represent the effect of flame stretch on the local flow-field. Accordingly, over a range of scalar dissipation rates, the flame is considered to burn and at high dissipation rates, to extinguish, thus emulating the physical observation of the phenomena that occurs in flames strained in opposed flow configurations, that are gradually increased in velocity until strain increases to the point where it is impossible for the flow to sustain a flame.

Flamelets are used differently in non-premixed and premixed conditions due to their different strengths of interaction with the main flow field.

The ensemble of laminar flamelets is considered to make up a turbulent flame brush. How exactly this is made up is by defining the probability density function of the instantaneous mixture fraction and its scalar dissipation rate (χ_{xt}). Thus, modifying the original pdf equation 2.41, we get the equation for the density-weighted mean mass fraction of a particular chemical species as:

$$\overline{\Phi} = \int\int \phi\left(f, \chi_{xt}, \overline{\mathrm{H}}\right) p(f, \chi_{xt}) \mathrm{d}f \, \mathrm{d}\chi_{xt} \tag{2.47}$$

Where:

$$\chi_{xt} = \frac{a_s exp(-2[erfc^{-1}(2f_{st})]^2)}{\pi} \tag{2.48}$$

$$\chi = 2D|\nabla f|^2 \tag{2.49}$$

χ_{xt} can be computationally demanding and would require a transport equation for the variance of the scalar dissipation rate, so a simplifying assumption of statistical independence between the mixture fraction and the scalar dissipation rate is made, thus ignoring the fluctuations in χ_{xt} and using a delta function for its assumed pdf shape.

A steady flamelets library is generated according to the following equations in mixture fraction space (f is the independent variable) [37]:

$$\rho \frac{\partial Y_i}{\partial t} = \frac{1}{2}\rho\chi \frac{\partial^2 Y_i}{\partial f^2} + S_i \quad \text{for each i species.} \tag{2.50}$$

$$\rho \frac{\partial T}{\partial t} = \frac{1}{2}\rho\chi \frac{\partial^2 T}{\partial f^2} - \frac{1}{2C_p}\rho\chi \left[\frac{\partial C_p}{\partial f} + \sum_i C_{p,i} \frac{\partial Y_i}{\partial f}\right] \frac{\partial T}{\partial f} \tag{2.51}$$

$$\chi(f) = \frac{a_s}{4\pi} \frac{3\left(\sqrt{\rho_\infty/\rho} + 1\right)^2}{2\sqrt{\rho_\infty/\rho} + 1} exp(-2[erfc^{-1}(2f)] \tag{2.52}$$

With these definitions, flamelets are generated accounting for the varying scalar dissipation/strain rates as:

$$\chi_i = \begin{cases} 10\chi_{i-1} & \text{for } \chi_{i-1} < 1/s \\ \chi_{i-1} + \Delta\chi & \text{for } \chi_{i-1} \geq 1/s \end{cases} \tag{2.53}$$

Until the flame extinguishes at high strain rates, the corresponding extinguished flamelet is the first excluded from the flamelet library.

2.6 Emissions modeling as a post-processing step

Steady RANS simulations routinely predict with inaccuracy predictions of CO and NO_x since both species cannot be considered in equilibrium instantaneously as the reactions proceed [36]. For this reason, special post-processing of the flow field is done to include the history of mixing and time-dependent methods are used to arrive at more accurate predictions.

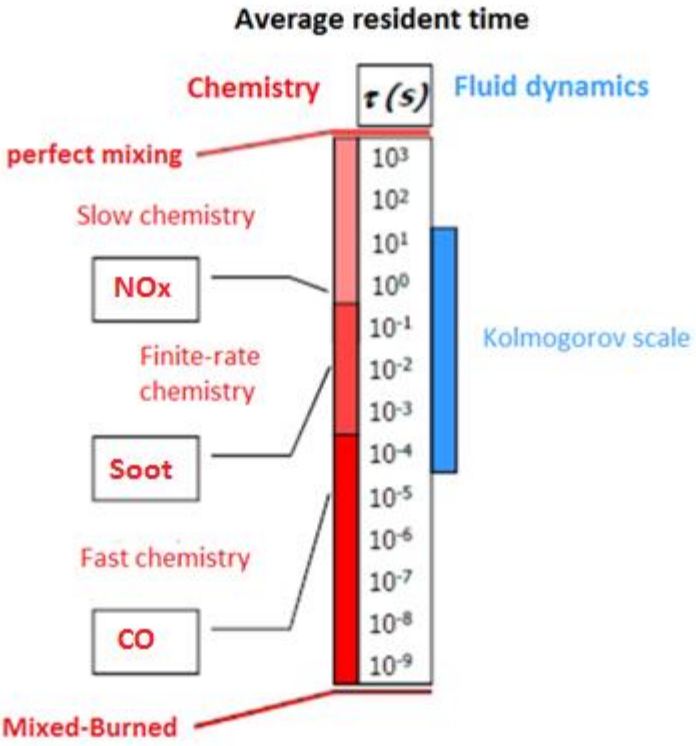

Figure 2.8 *Characteristic times of Chemistry and turbulent eddies within a combustion system [38]*

CO emissions are characterized by very fast chemistry that bring a rapid formation while consumption can be quite slow at relatively low temperature thus as leading a very imprecise

prediction. Instead, NO_x emissions are very slow species compared to the others and can never be considered using fast chemistry approaches (Figure 2.8).

Kinetic reaction rates are used to model the source terms of the NO_x transport equations, accordingly as thermal, prompt and fuel NO_x is considered. In this section a little background will be provided with some brief comments on the use of these methods.

2.6.1 The unsteady laminar flamelet

The steady laminar flamelet, described in section 2.5, models local chemical non-equilibrium due to the straining effect of turbulence. In many combustors, the strain is small at the outlet and the steady flamelet model predicts all species, including slow and fast forming species, to be near equilibrium, which is often inaccurate. The cause of this inaccuracy is the disparity between the flamelet time-scale, which is the inverse of the scalar dissipation, and the slow-forming species time-scale, which is the residence time since the species started accumulating after mixing in the combustor [23].

In the steady flamelet equations, the scalar dissipation is modeled as a function of the mixture fraction. This is no longer the case with the unsteady flamelet method, where the scalar dissipation and the mixture fraction are treated as independent variables.

The flamelet library computed for the steady flamelet analysis is considered in the context of trying to find a specific flamelet at a particular point in space and instant in time by solving a transport equation for a so-called probability marker for particles that represent the flamelets [34]. The initial positions are determined based on their deviation towards the rich side from the stoichiometric mixture fraction. This generally places the initial positions of the particles in the vicinity of the fuel injectors. As these particles processed through the domain, the characteristics of the flamelets that they represent can be obtained as function of the local flow properties that have been obtained already through the steady-flamelet method. These are used to update the species mass fractions and temperature.

This probability marker and the unsteady flamelet equations are time marched until the particles have left the domain. The transient species mass fractions and temperatures are calculated and averaged over time thus leading to different means of these parameters than the steady flamelet prediction. The equations that describe this process are detailed below.

Transport equation for the Probability Marker:

$$\frac{\partial I}{\partial t}(\rho \mathrm{I}) + \nabla(\rho v \mathrm{I}) = \nabla\left(\frac{\mu_t}{\sigma_t}\nabla \mathrm{I}\right) \tag{2.54}$$

$$I = \begin{cases} 1 & \text{for } \overline{\mathrm{f}} \geq f_{init} \\ 0 & \text{for } \overline{\mathrm{f}} < f_{init} \end{cases} \tag{2.55}$$

Scalar Dissipation is expressed as a volume weighted function of the local stoichiometry calculated from the steady flamelet method prior.

$$\chi_{st}(t) = \frac{\int_V I\left(\overline{\mathrm{x}}, \mathrm{t}\right)\rho\left(\overline{\mathrm{x}}\right)\overline{\chi}_{st}^{3/2}\left(\overline{\mathrm{x}}\right)\mathrm{dV}}{\int_V I\left(\overline{\mathrm{x}}, \mathrm{t}\right)\rho\left(\overline{\mathrm{x}}\right)\overline{\chi}_{st}^{1/2}\left(\overline{\mathrm{x}}\right)\mathrm{dV}} \tag{2.56}$$

The Temperature is calculated at each instant as a function of the local mixture fraction obtained from the solution of the steady flamelet method.

$$T(f,t) = T^{adiabatic}(f,t)\xi(f,t) \tag{2.57}$$

Where:

$$\xi(f,t) = \frac{\int_V I\rho T(\overline{\mathrm{x}}\,|\mathrm{f}) \Big/ T^{adiabatic}(f,t)\, dV}{\int_V I\rho dV} \quad \text{for non-adiabatic cases} \tag{2.58}$$

The unsteady flamelet mean species mass fraction are obtained as:

$$\overline{\mathrm{Y}}_k^{ufla} = \frac{\int_0^1 I\rho[\int_0^1 Y_k(f,t)P(f)df]\,dt}{\int_0^1 I\rho dt} \tag{2.59}$$

It's important, however, to specify that in this work the unsteady flamelet model has been used to predict only the CO fraction, given that the NO_x species are not included in the kinetic scheme. For the nitrogen-containing species, a Post-processor method has been adopted.

An example of monitoring the probability marker progress through the domain is shown in Figure 2.9 below.

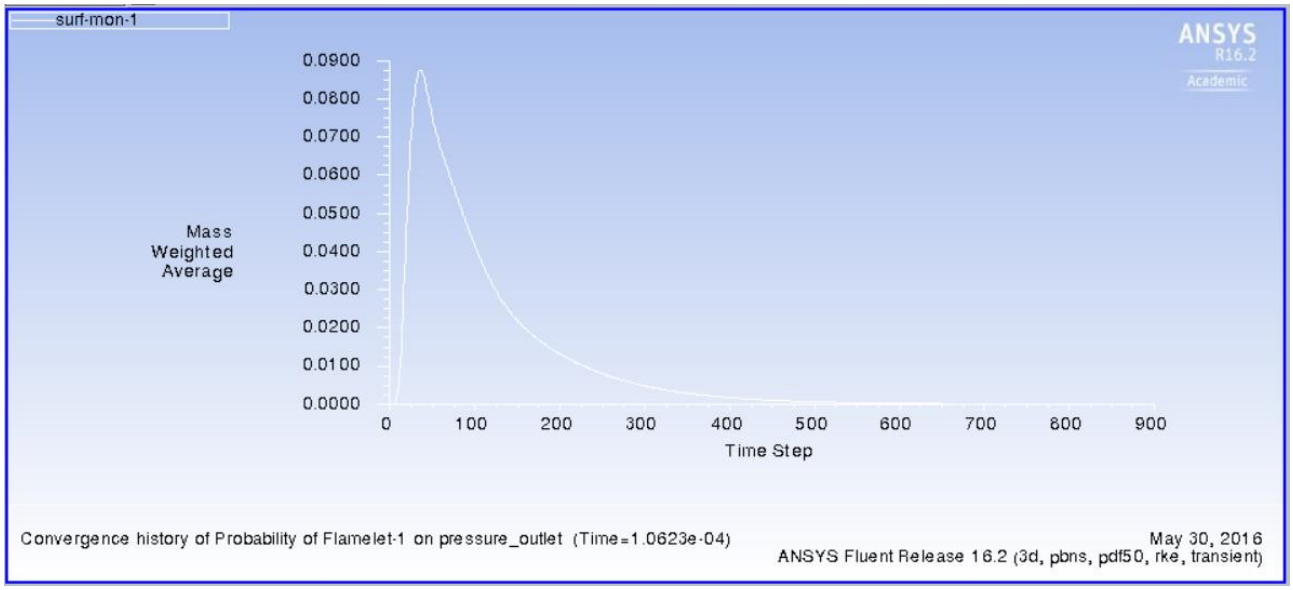

Figure 2.9 *Probability marker progress through the domain*

In Figure 2.9 the exit of the domain has been monitored. The time-step is adaptive and the equations have been solved till reaching convergence, that is to say when the probability marker has completely left the domain (going to a zero value). As expected, the total time needed is similar to the fluid residence time of the combustor.

Unfortunately, as we will see in Chapter 4 section 4.3.2 and 4.3.3, this model doesn't produce satisfactory results for CO in this combustor. For this reason, it was not adopted for NO_x.

2.6.2 Post-processing for NO_x

NO_x is a generic term for the mono-nitrogen oxides NO and NO_2. NO_x forms either due to nitrogen fixing in the fuel, rich mixtures, high temperatures, intermediate radical formations, re-burn by reduction of NO by CH_x radicals to produce hydrogen cyanides (Figure 2.10). Lean-premixed combustion further implies an oxygen surplus, which gives rise to the effect of intermediate N_2O formations that could account for as much as 30% of the NO_x production from molecular N_2 in gas turbine combustors [39].

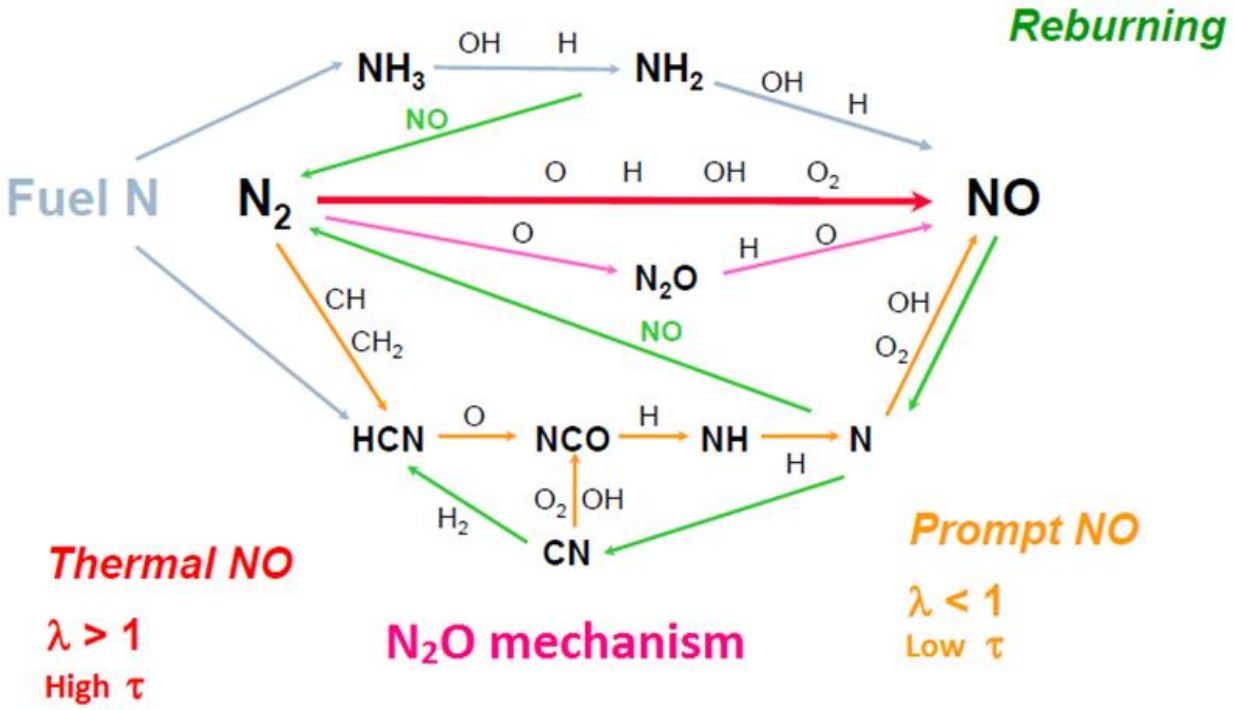

Figure 2.10 *Formation mechanisms of NOx*

Thermal NO_x is formed through high temperature oxidation of the diatomic nitrogen found in combustion air. The formation rate is primarily a function of temperature and residence time of nitrogen at that temperature. At high temperatures, usually above 1900 K, molecular nitrogen (N_2) and oxygen (O_2) in the combustion air dissociate into their atomic states and participate in a series of reactions.

Prompt NO_x - also called Fenimore NO_x - are attributed to the reaction of atmospheric nitrogen, N_2, with radicals such as C, CH, and CH_2 fragments derived from fuel, where this cannot be explained by either the aforementioned thermal processes. Occurring in the earliest stage of combustion, this results in the formation of fixed species of nitrogen such as NH, HCN, H_2CN and CN which can oxidize to NO. Prompt NO_x can be a major source on formation of NO_x at low temperature combustion of oxygenated fuels. Prompt NO_x is also proportional to the number of carbon atoms present per unit volume.

Fuel NO_x is of concern when the fuels considered contain nitrogen. Typically, solid and liquid fuels are examples of this. The intermediates formed (HCN, NH_3, N, CN, NH etc.,) during the pathways leading to NO_x production are important and their transport effects need to be considered. This leads to additional complications in modeling, especially since the reaction rates required to model

the source terms of the production of these radicals is still not well understood. There are two primary paths of formation. The first involves the oxidation of volatile nitrogen species during the initial stages of combustion while the second involves the combustion of nitrogen contained in the char matrix during the combustion of the char portion of the fuels. This reaction occurs much more slowly than the volatile phase. The real kerosene has been characterized in the MAEM-RO project and the analysis has showed that the amount of N is negligible. For this reason, in this thesis work an ideal kerosene fuel is used and fuel NO_x has not been taken into account.

Reburn has been considered and the turbulence chemistry interaction is modeled using a presumed pdf approach which will be detailed in the following description of the equations used.

The post-processing step starts by obtaining a converged flow field. Transport equations are solved for NO and the individual contributions of thermal, prompt, and N_2O intermediates are taken into account through the NO source term. Re-burn was considered by considering the reduction of NO_x to HCN by considering the predictions of CH, CH_2 and CH_3 radicals obtained from the converged solution.

The pathways of NO_x production considered in the calculations in this work are detailed below along with the source term details. There are several approaches to calculate the source terms which involve the use of predicted mass fractions of O_2, O, CH, CH_2, CH_3, etc; however, only the ones with the greatest possible accuracy were used, which in the context of the simulations undertaken in this thesis, took advantage of the accurate predictions of fast radicals from the instantaneous solutions rather than use the partial-equilibrium or equilibrium approaches.

Transport Equations:

For NO

$$\frac{\partial I}{\partial t}(\rho \mathrm{Y}_{NO}) + \nabla(\rho v \mathrm{Y}_{NO}) = \nabla(\rho D Y_{NO}) + S_{NO} \tag{2.60}$$

For N_2O

$$\frac{\partial I}{\partial t}\left(\rho \mathrm{Y}_{N_2O}\right) + \nabla\left(\rho v \mathrm{Y}_{N_2O}\right) = \nabla\left(\rho D \mathrm{Y}_{N_2O}\right) + \mathrm{S}_{N_2O} \tag{2.61}$$

If fuel NO_x is considered, similar equations are used to track HCN and NH_3. The source terms in equations over are evaluated separately for different NO_x mechanisms.

A brief description of each of the mechanisms used for the simulations is detailed below and the section concludes with the details of how these kinetic mechanisms are convoluted with the fluctuations in temperature and species due to turbulence-chemistry interaction, accounted for by a probability density function methods like the one used for mixture fraction calculations in the non-premixed approach.

2.6.2.1 Thermal NO_x formation

The original Z'eldovich mechanism contributes to the source term of equation 2.60, which is significant at near-stoichiometric conditions and in moderately fuel-lean mixtures:

$$O + N_2 \rightleftharpoons N + NO$$

$$O + O_2 \rightleftharpoons O + NO$$

$$N + OH \rightleftharpoons H + NO$$

The net rate of formation of NO through this mechanism is given by:

$$\frac{d\,[NO]}{dt} = k_{f,1}[O][N_2] + k_{f,2}[N][O_2] + k_{f,3}[N][OH] - k_{b,1}[NO][N] - k_{f,2}[NO][O] - k_{f,3}[NO][H] \tag{2.62}$$

From this, the source term is expressed as:

$$S_{thermal,NO} = M_{w,NO}\frac{d\,[NO]}{dt} \tag{2.63}$$

f and b denote forward and backward rate constants for each of the reactions. Experimental data is used to determine these constants (Hanson and Salimian [40]). The concentrations of O, N_2, N, OH, and H are retrieved from the steady flamelet calculations. Since the underlying assumption of fast response to scalar dissipation changes is valid for these species, the accuracy in their predictions is

high and can so be used without resorting to equilibrium or quasi-steady methods, which would otherwise have to be used. Of special importance is the O radical's concentration changes due to its third body reactions which lead to higher concentrations at equilibrium.

2.6.2.2 Prompt/Fenimore NO_x formation

Usually the contribution of prompt NO_x formation to the overall NO concentration is small when compared to thermal NO_x, especially when the mixture is lean.

The route to NO formation is expressed as a set of global reactions:

$$CH + N_2 \rightleftharpoons HCN + N$$

$$N + O_2 \rightleftharpoons NO + O$$

$$HCN + OH \rightleftharpoons CN + H_2O$$

$$CH + O_2 \rightleftharpoons NO + CO$$

Of these equation, the first one is the most dominant reaction near the flame front and is subsequently modeled as a global rate reaction controlling the formation of the overall prompt NO_x. However, due to uncertainties in the reaction rate, a global rate constant was derived by De Soete [41] by considering the rate of production of NO from prompt NO_x is equal to the prompt NO_x rate of reaction that remains after the overall N_2 formation is removed. This is justifiable since the O radical prefers to oxidize nitrogen to NO rather than allowing N_2 to form.

Thus, the reaction rate is expressed as:

$$\frac{d[NO]}{dt} = k_{pr}[O_2]^a[N_2][FUEL]e^{-E_a/RT} \tag{2.64}$$

The model has been observed to exhibit inaccuracy for high pressures and higher hydrocarbons when tested against by Backmier [42].

In order to reduce this inaccuracy, the model includes a correction term which takes into account the overall equivalence ratio and the number of carbon atoms per volume since prompt NO formation is directly proportional to these factors rather than to the hydrocarbon fuel composition.

The modified De Soete [41] model is detailed below, incorporating the correction factor and a pressure dependent rate constant.

$$\frac{d[NO]}{dt} = k_{pr}{}'[O_2]^a[N_2][FUEL]e^{-E_a/RT} \tag{2.65}$$

where the modified rate constant k_{pr}' is expressed as:

$$k_{pr}{}' = 6.4 \text{ x } 10^6 \left(\frac{RT}{p}\right)^{a+1} \tag{2.66}$$

With an activation energy equal to Ea = 303474.125 J/gmol

The correction factor is expressed as a curve fit, valid for equivalence ratios between 0.6 and 1.6 for alkane hydrocarbons:

$$f = 4.75 + 0.0819n - 23.2\phi + 32\phi^2 - 12.2\phi^3 \tag{2.67}$$

The oxygen reaction order, a is expressed as the following ranges according to De Soete [41]:

$$a = \begin{cases} 1 & \text{for } X_{O_2} \leq 4.1 \text{ x } 10^{-3} \\ -3.95 - 0.9\ln(X_{O_2}) & \text{for } 4.1 \text{ x } 10^{-3} \leq X_{O_2} \leq 1.11 \text{ x } 10^{-2} \\ -3.95 - 0.1\ln(X_{O_2}) & \text{for } 1.11 \text{ x } 10^{-2} \leq X_{O_2} \leq 0.03 \\ 0 & \text{for } X_{O_2} \geq 0.03 \end{cases} \tag{2.68}$$

The concentration of O_2 is directly calculated from the steady flamelet solution.

The prompt NO source term is expressed as:

$$S_{prompt,NO} = M_{w,NO} \frac{d\,[NO]}{dt} \tag{2.69}$$

2.6.2.3 Intermediate N_2O pathways to NO_x formation

NO_x formation due to recombination reactions between nitrogen and oxygen and subsequent oxidation of nitrous oxide to NO is important and it has been found to be a significant contributor to the overall NO formation in the current simulations.

Melte and Pratt [43] first proposed this mechanism, deemed important in the presence of high ambient pressures and oxygen excess. The contribution can be very important in case of diluted systems.

Two reactions are considered as its global pathway:

$$N_2 + O + M \rightleftharpoons N_2O + M$$

$$N_2O + O \rightleftharpoons 2NO$$

M is a third body, chemically inert species, that becomes significant at high pressures and temperatures, increasing the collision frequency of various atoms. Here it facilitates the recombination of N_2 and O. Furthermore, the O radical makes the reactions favorable being highly reactive species and in abundance due to the oxygen rich environment in lean premixed combustion regimes. Taken together, the production of NO_x from subsequent oxidation of N_2O becomes highly favored.

The rate of reaction is expressed as:

$$\frac{d[NO]}{dt} = 2\left(k_{f,2}[N_2O][O] - k_{b,2}[NO]^2\right) \tag{2.70}$$

The concentration of N_2O is obtained by considering its rate of reaction as quasisteady and consequently accounting only for its transport without production when solved for with a transport equation.

The concentration can be obtained as follows:

$$[N_2O] = \frac{k_{f,1}[N_2][O][M] + k_{b,2}[NO]^2}{k_{b,1}[M] + k_{f,2}[O]} \tag{2.71}$$

2.6.2.4 NO reduction through reburn

NO_x can deplete due to its reduction by CH_x radicals to hydrogen cyanides. However, these reactions occur within a narrow band of temperature and Fluent considers the following mechanism to be valid between 1600K and 2100K.

The mechanism is hence reported:

$$CH + NO \rightleftharpoons HCN + O$$

$$CH_2 + NO \rightleftharpoons HCN + OH$$

$$CH_3 + NO \rightleftharpoons HCN + H_2O$$

The NO destruction rate is calculated as a sink term to the overall NO transport equation:

$$-\frac{d[NO]}{dt} = k_1[CH] + [NO] + k_2[CH_2] + [NO] + k_3[CH_3] + [NO] \quad (2.72)$$

The reburn NO source term is expressed as:

$$S_{reburn,NO} = -M_{w,NO}\frac{d\,[NO]}{dt} \quad (2.73)$$

The concentrations of the CH_x radicals are taken directly from the computed values from the steady flamelet method.

Where temperatures are outside the aforementioned range the NO formation due to reburn contribution is not computed.

2.6.2.5 NO chemistry - Turbulence interaction

Relying on experimental datasets from analysis of laminar flame speeds and shock tube studies [44], the equations seen until now, cannot be directly used in the context of turbulent flames with a RANS approach. In order to account for the significant effects of fluctuations in temperature and species mass fractions due to turbulence, a pdf method is used to obtain the mean turbulent reaction rate.

The probability distribution function takes into account the temperature and, in these simulations, the oxygen radical species, considering an instantaneous reaction rate.

Thus, the following procedure is used to obtain the mean source term of NO in turbulent flows:

$$\overline{\mathrm{S}}_{NO} = \int \int S_{NO}(T,[O])P(T)P([O])dTd([O]) \tag{2.74}$$

assuming statistical independence of T and [O].

The presumed shape (beta-pdf) is used and while no special treatment is required for species mass fraction of O (since it lies between 0 and 1), the temperature is normalized so that its mean lies between these limits and thus valid for use within a beta function. The calculation of variance is not computed using a transport equation but instead is approximated to:

$$\sigma^2 = \frac{\mu_t}{\rho}\frac{k}{\varepsilon}\frac{C_g}{C_d}\left(\nabla \overline{\mathrm{m}}\right)^2 \tag{2.75}$$

Chapter 3 – Engine geometry and CFD simulation

The purpose of the experimental campaign (MAEM-RO project [45]) was to measure gaseous emissions and main engine parameters during flight tests with the aim of producing a database of the pollutant emissions in different operating conditions to validate the numerical combustion model.

MAEM-RO project has been successfully completed in December 2013. Numerous flight missions have been performed in different environmental conditions to verify the measurement methodology and the equipment installed on board. A methodology suitable for flue gas concentrations measurement during flight tests must be designed and, of course, verified in meaningful tests. In order to develop such a methodology, the standard procedures used in the automotive and heavy duty gas turbines fields were taken into account.

The test sequence, done using the PZL SW-4 helicopter, includes a steady-states flight (No. 1734), a baseline mission profile (No. 1735) and an alternative mission profile (No. 1736).

The analyzer Gasmet DX-4000 FT-IR, which is able to measure several components (reported below) in about 1 second, has been chosen:

SO_2	N_2O	C_2H_4
CO	HCl	C_2H_6
CO_2	H_2O	HCOH
NO	HF	O_2
NO_2	CH_4	

This analyzer meets all the requirements for flight test. The sampling probe has been welded on the stack according to qualified TIG (Tungsten Inert Gas) welding procedures.

A new set of boundary conditions, based on experimental data, has been created and, thanks to more details about the engine geometry, the CAD model of the combustor liner has been improved too.

Moreover, a new type of fuel was introduced and a new set of results has been performed.

The data from the flight test campaign have been used to populate a database for predictive tool validation.

3.1 CFD simulation logic path

In general, Computation Fluid Dynamics (CFD) could be viewed as a computer program that simulates the fluid flowfield of an engineering device for design purposes and research interest [46]. The basic structure of a typical CFD model could be represented as in figure 3.1.

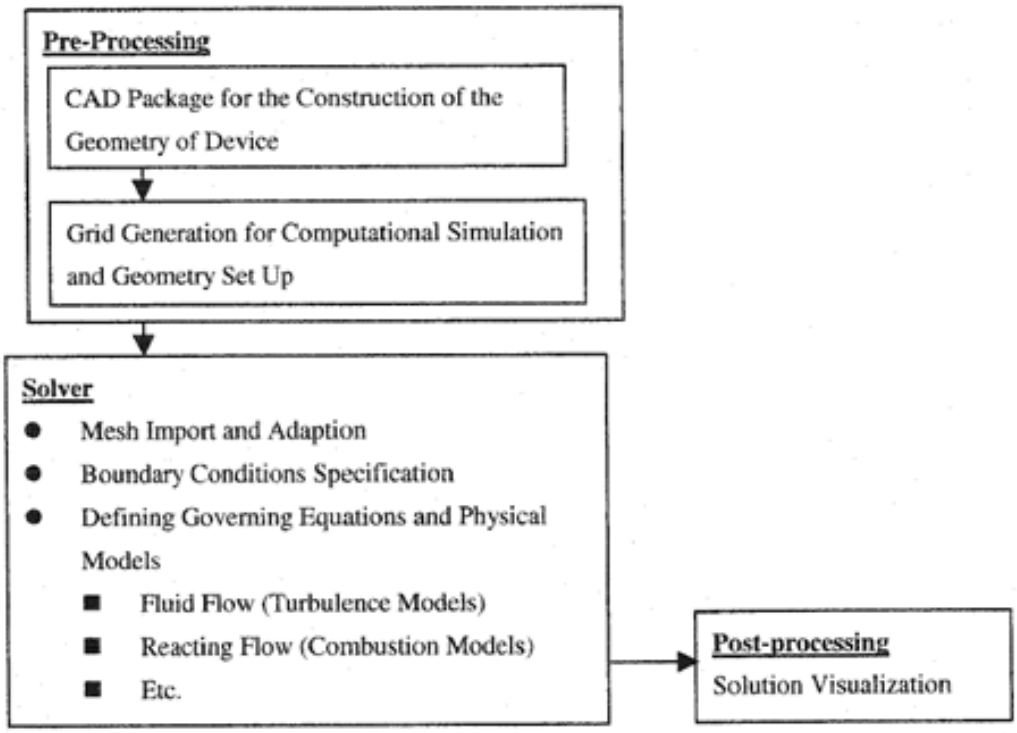

Figure 3.1 *General structure of CFD modeling [46]*

The geometry of the device is constructed in pre-processing with a CAD software and is subsequently meshed with computational grids for numerical simulations. These processes require engineering justifications for device geometry simplifications and grid generation methods to obtain an accurate CFD simulation while retaining a reasonable computation time.

In solving the problem, the appropriate physical models must be selected carefully in order to not underestimate the limitations that these models could have.

Results of the simulation are compared against scientific or technical data to ensure their validity.

3.2 Combustor chamber geometry

A 3D solid model has been built for the CFD combustion simulations of the Allison 250 combustor.

Some simplifications have been done while retaining the important features on the liner and the combustion flowfield:

- The model was built to simulate the internal flowfield of the combustion liner;
- Liner thickness was not included in the model;
- Complex dome-swirler and cooling slots flow path were simplified.

Three zones, the dome-swirler zone, primary zone, and dilution zone, as shown in Figure 3.2, can describe the liner.

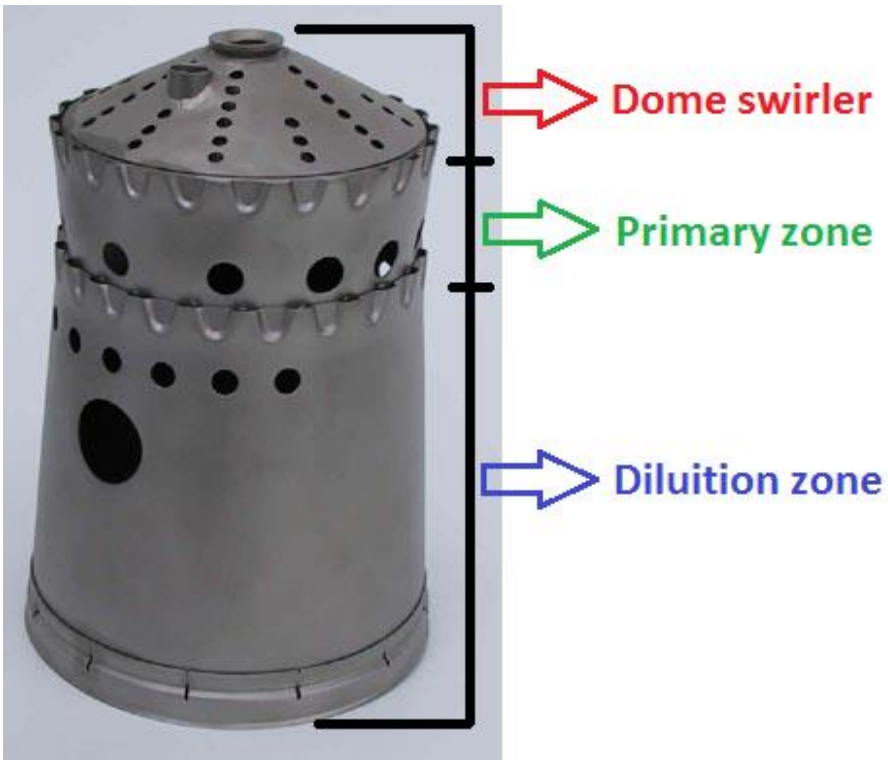

Figure 3.2 *Allison 250 Gas Turbine Engine Combustor Liner*

The dome swirler zone consists of the mounting ports for the fuel injection nozzle and igniter, and the dome swirler wall orifices. The primary zone starts with a wiggle strip cooling slot and 12 primary injection holes. A similar cooling slot is used on the dilution zone, followed by 14 dilution holes and 2 dilution holes.

The dimensions of the outline of combustor liner are shown in Figures 3.3 and 3.4. The cooling slots are 0,25 cm width, and the injection port is 0,5 cm in depth and 1,6 cm in diameter.

The solid model has been later refined to better simulate the inlet and outlet boundaries of the combustor.

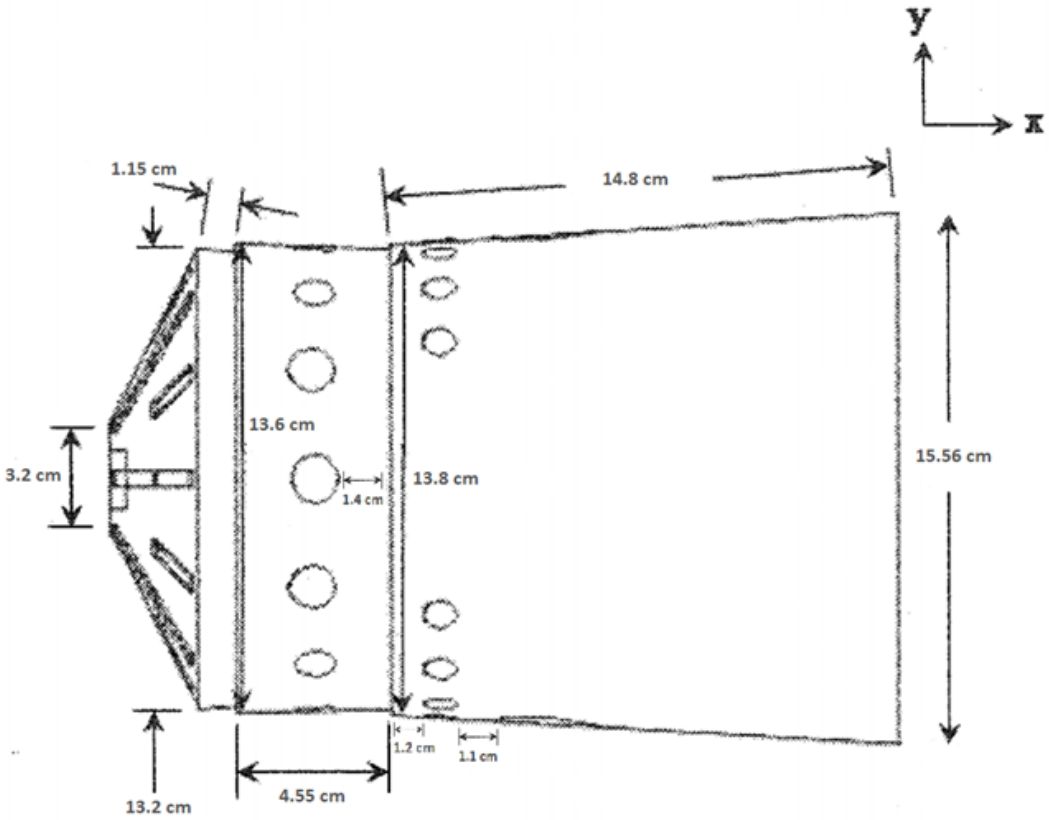

Figure 3.3 *Allison 250 Gas Turbine Engine Combustion Chamber Geometry, adapted from [46]*

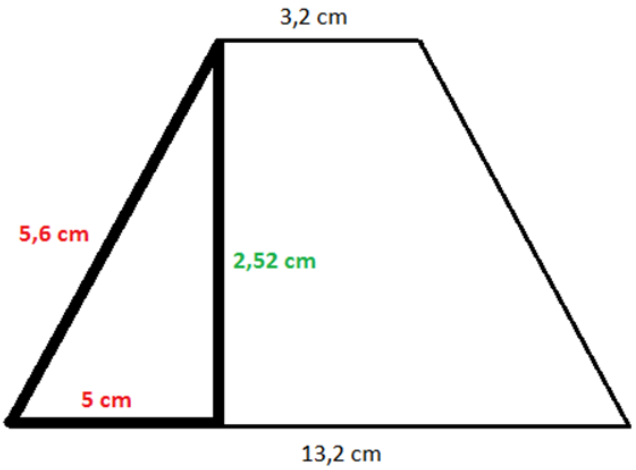

Figure 3.4 *Swirler dome plan section*

The distributions of the hole are shown in Figures 3.5 and 3.6; we can note the combustor symmetry in xy-plane with the origin at the beginning of the centerline of the combustor.

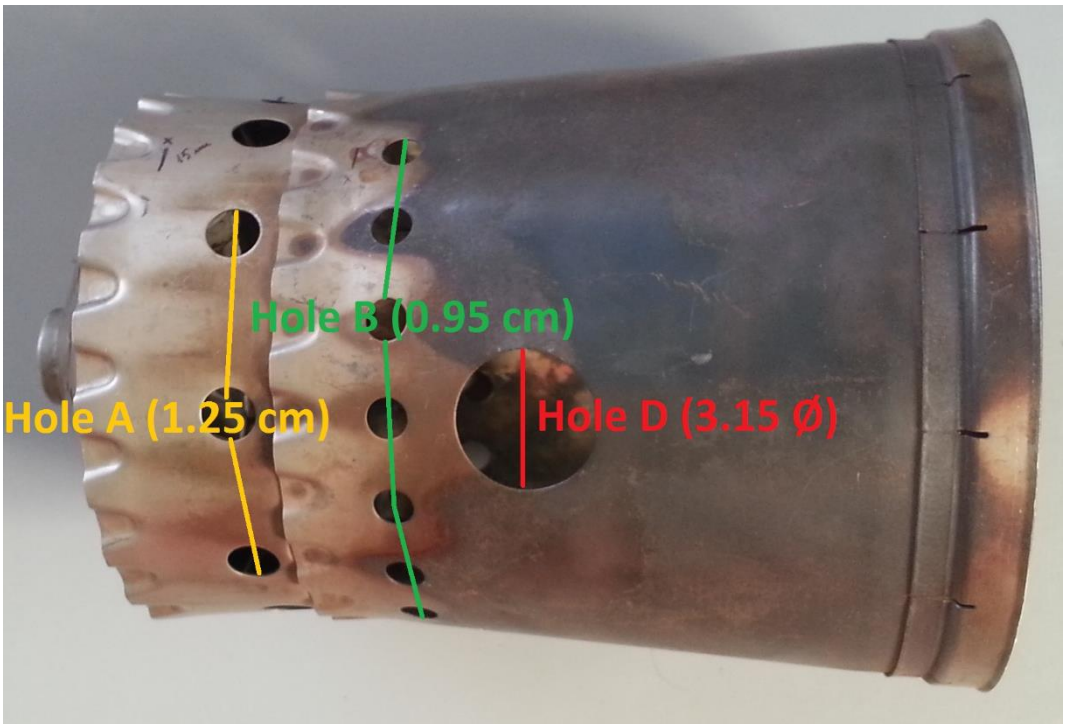

Figure 3.5 *Layout of liner injection holes A-C-D*

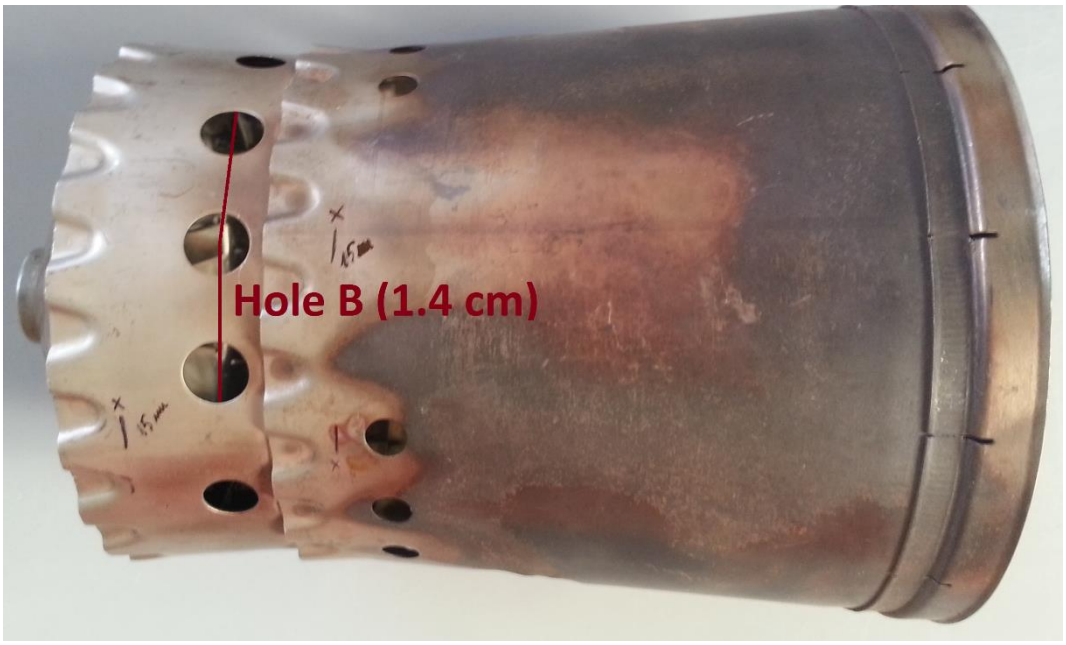

Figure 3.6 *Layout of liner injection holes B*

Three Hole A, seven Hole C and a Hole D are found on each side of the xz-plane and three Hole B are found on each side of the xy-plane. The angles between Hole A are 36° with respect to the x-axis in the yz-plane, 20° for Hole B and 18,4° for Hole C.

A turbine disk protecting shield is present at the outlet. It is important to include its geometry to simulate the realistic outflow boundary condition of the combustor. The complex profile of the turbine disk shield (Figures 3.7 and Table 2) in xy-plane is measured as:

x (cm)	0	0,1538	3,076	6,614	6,152	6,531
y (cm)	4,071	3,89	3,709	3,347	2,171	1,266

Table 2 *Construction points for turbine disk shield*

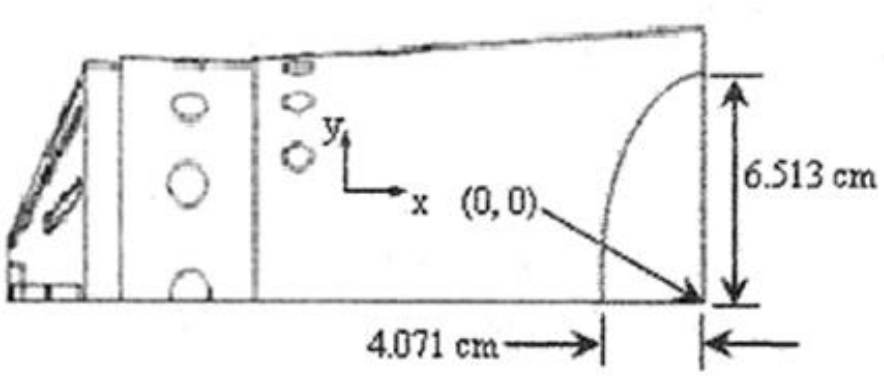

Figure 3.7 *Geometry of turbine disk shield [46]*

In this geometry, the dome wall orifices have been replaced by rectangular “cut-out” to simulate the injections of the swirled flow that is generated by the louver plates (Figure 3.8). The injection slots are distributed evenly on the dome wall with 0,5 cm away from the side of the dome wall as shown in Figure 3.8. Since the wall thickness is not included in the model, the cut outs on the dome wall are 4,95 cm in length, 1 cm in width and 0,2 cm in depth to represent the injection Plane 1 to Plane 5. It should be noted that the injection plane 3 is 0,15 cm wide.

The cooling slots have been simplified to continuous circumferential slots, as this seems to yield better description for the inlet boundaries of the cooling films from the wiggle strip slots. A fuel nozzle port has been added to the solid model for more accurate specification of the position of the fuel injection.

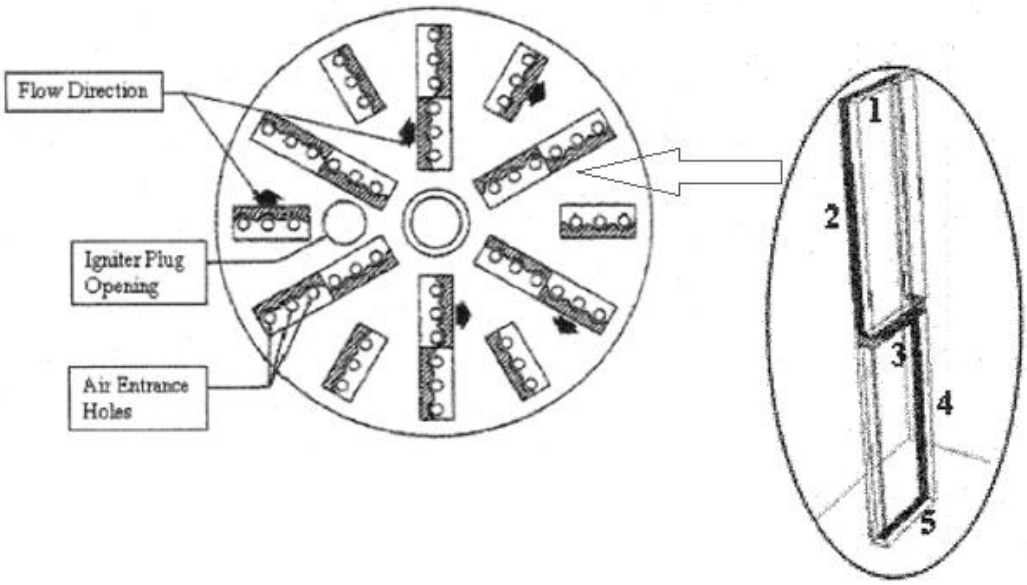

Figure 3.8 *Dome swirler holes distribution and swirled flow direction [46]*

By real photos, thanks to Bertacin R., Ph.D of the Forlì aerospace engineering campus (also see figures 3.5 and 3.6), we could see and verify that assumptions made until now and various dimensions considered are all correct. There is especially confirmation of the actual design of the swirler plan, as we can see in Figure 3.9 below.

Figure 3.9 *Real photo of the swirler plan*

The 3D combustor model has been generated, as shown in Figures 3.10 and 3.11, with the Design Modeler, a CAD tool included in Ansys Workbench.

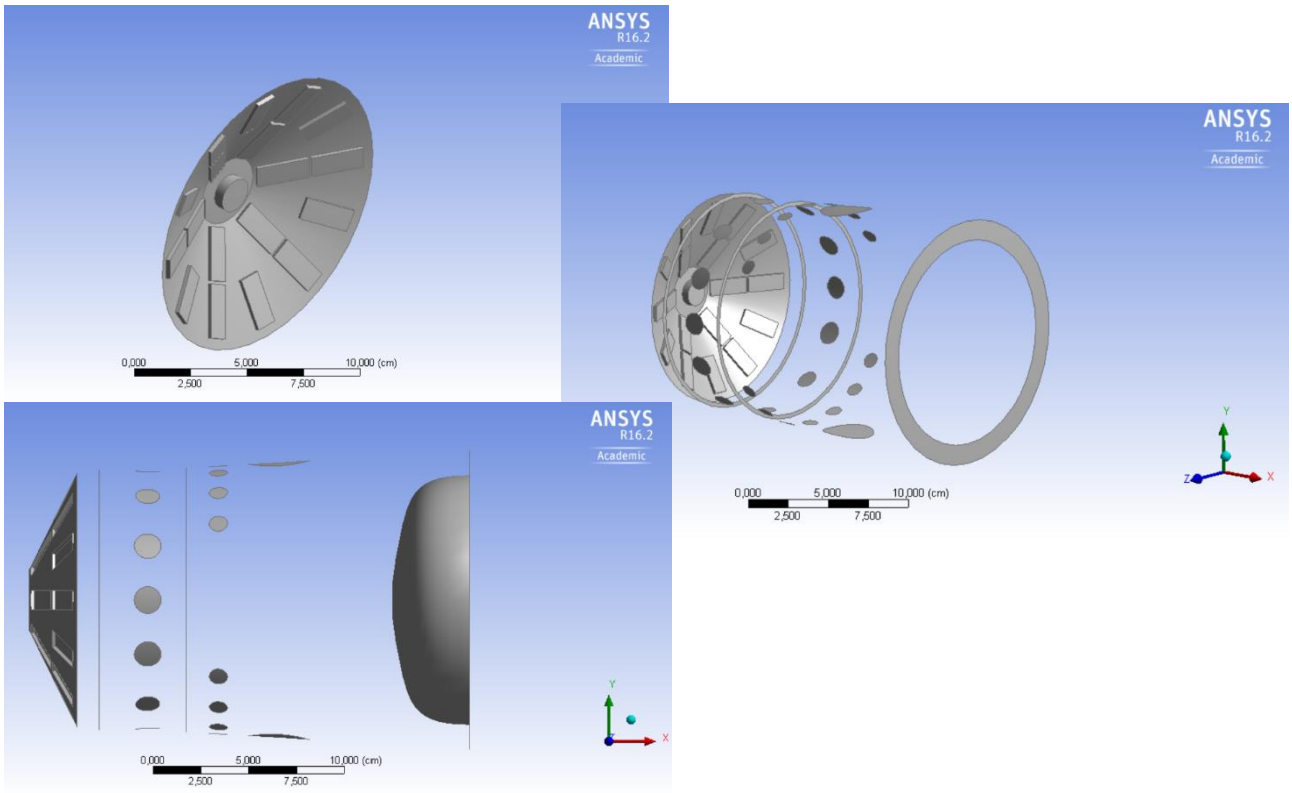

Figure 3.10 *3D combustor liner (1)*

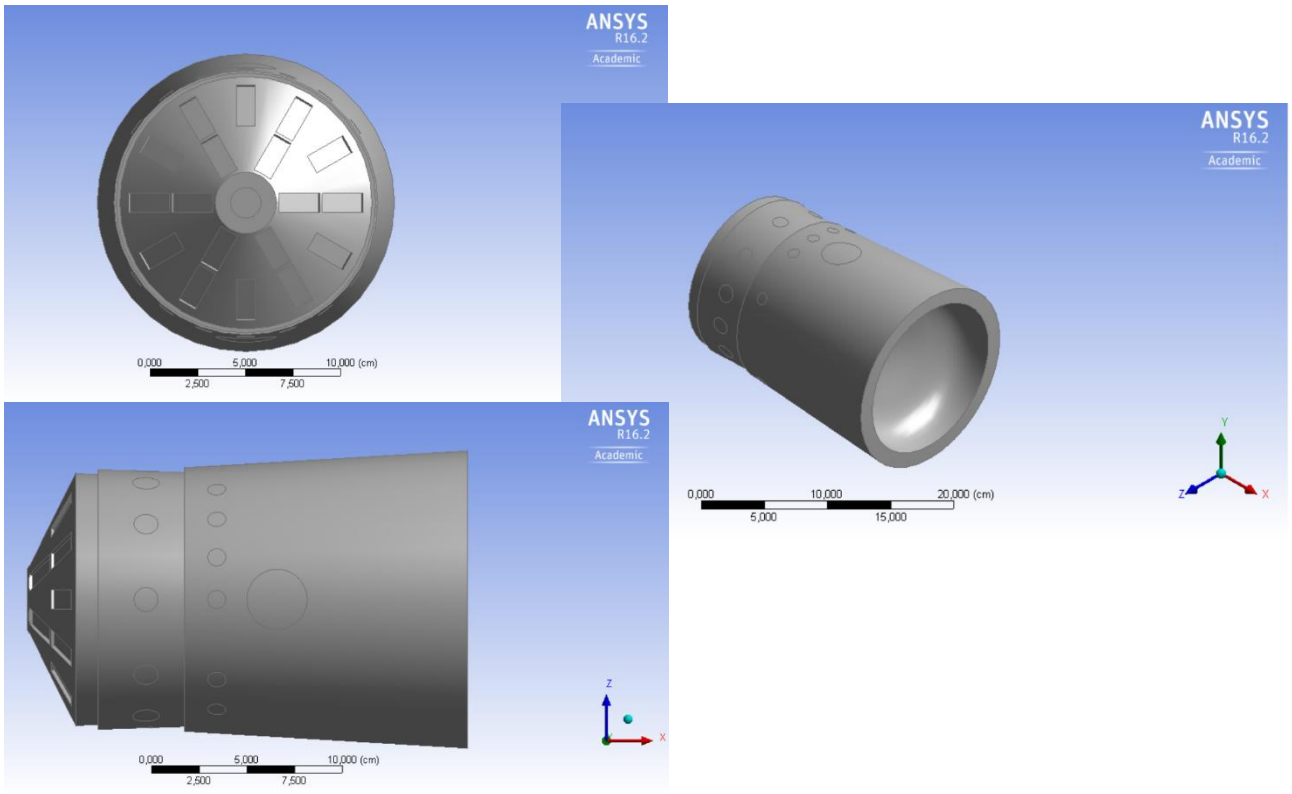

Figure 3.11 *3D combustor liner (2)*

The planes (XY, ZX) and the center line, used as reference for result reports, are reported in the Figure 3.12. The center line is particularly useful to analyzed the variation of some parameters along itself understanding so the quality of the simulation performed (see the following section 3.3.1).

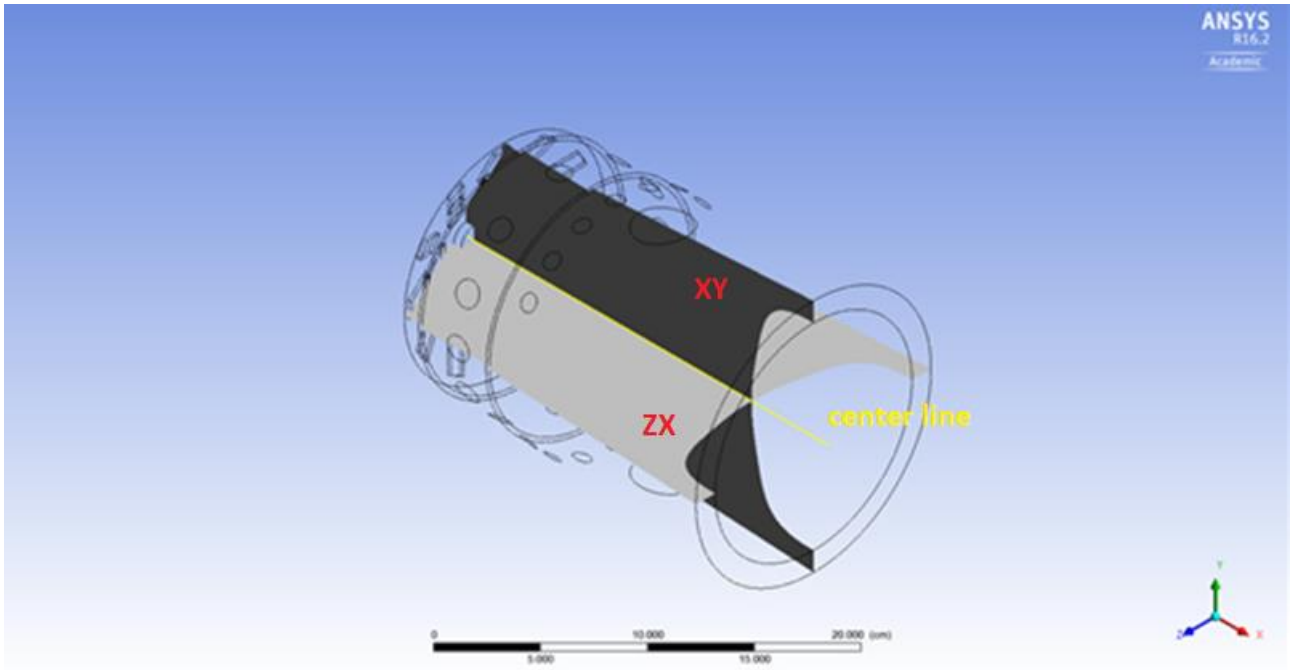

Figure 3.12 *The planes (XY, ZX) and the center lines*

3.3 Grid generation

The Fluent Pre-Processor Meshing package has been used for the grid generation of the combustor model.

Unstructured grids have been used for meshing the solid model because this technique is easier to be applied in defining the geometry of the combustor and allows the use of grid adaption for grid density refinement. Advance size function has been set on proximity and curvature option to improve grid refinement near combustor orifices and curvatures. A growth rate of 1,075 has been set and thus a dense grid of 3 Million cells has been generated (Figures 3.13 and 3.14).

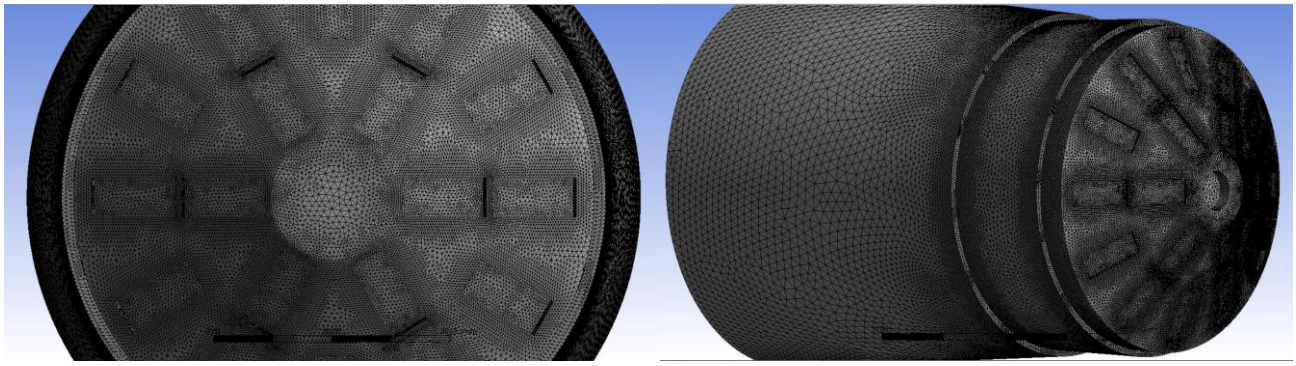

Figure 3.13 *Detail of the liner mesh*

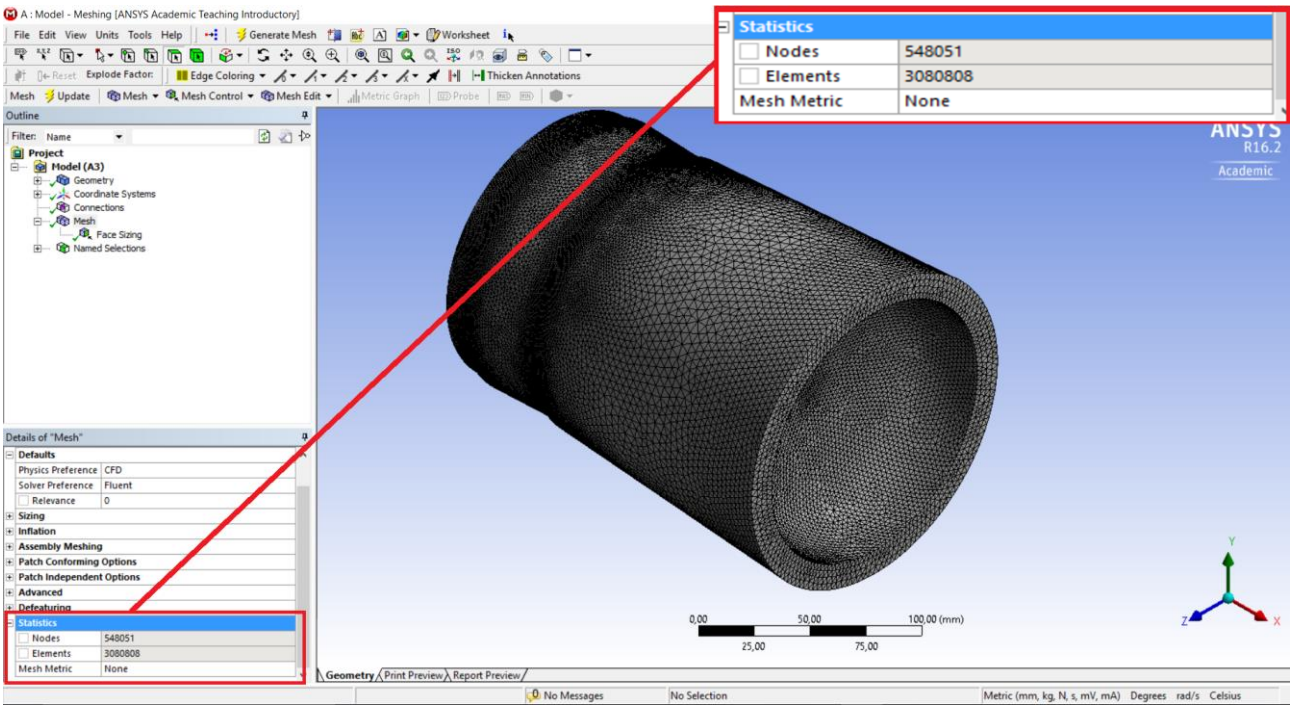

Figure 3.14 *Number of cells of the final combustor mesh*

The final mesh of the combustor has a high density at the region of dome-swirler and near the liner injection, where strong interaction and mixing of the flow occurred.

3.3.1 Mesh sensitivity

To choose an appropriate number of cells, good enough for simulations and able to minimize the computation time, a sensitivity analysis has been performed.

A sensitivity analysis is a technique used to determine how different values of an independent variable impact on a particular dependent variable under a given set of assumptions. This technique is used within specific boundaries that depend on one or more input variables.

For this analysis, we used a simple case using a 1-step kinetic scheme for kerosene as fuel and species transport as species model. The simplicity of these assumptions, however, should not affect the reliability of our conclusions. The basic idea is just understanding the best compromise between accuracy and computational efforts.

The evaluation has been made plotting temperature and velocity profiles along the center line for mesh with different number of cells (Figures 3.12 and 3.13) for a reference power of 191 hp.

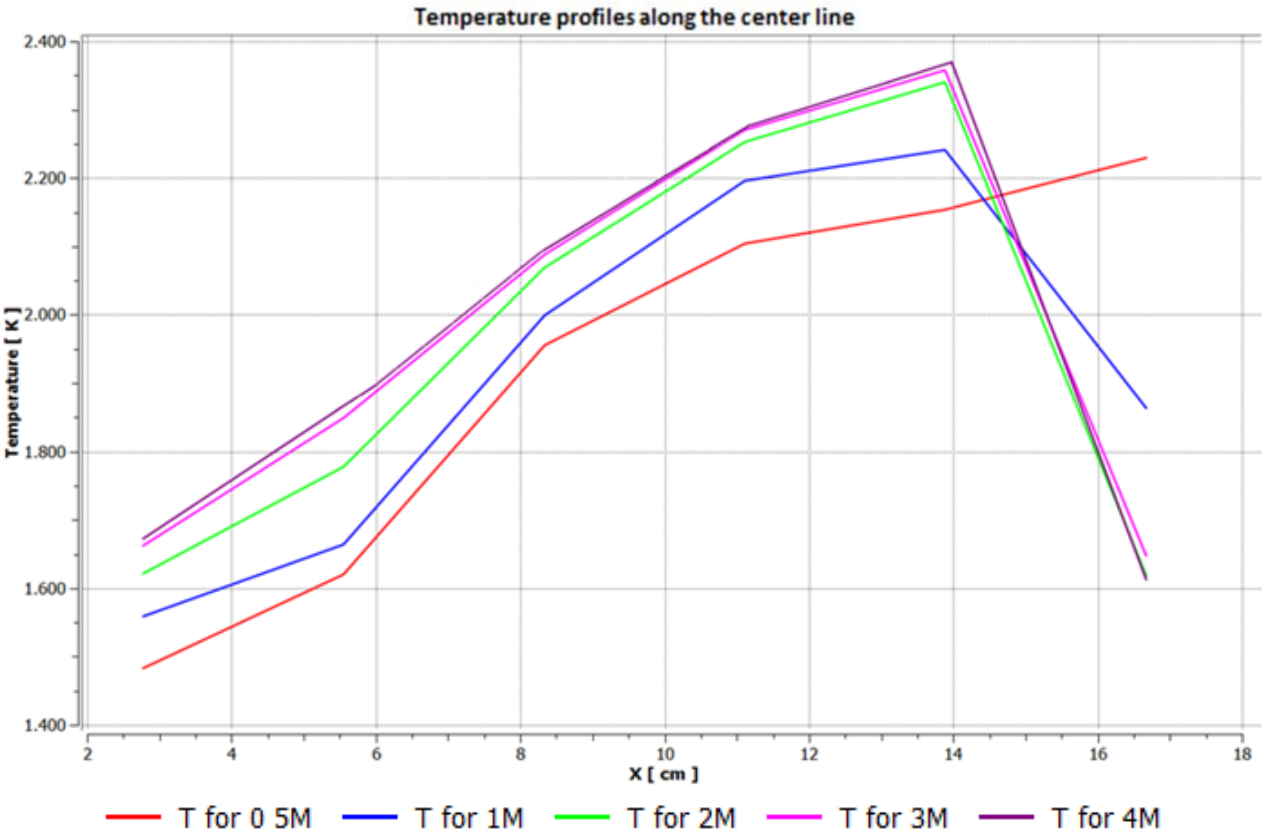

Figure 3.14 *Temperature profiles along the center line for mesh with 0.5, 1, 2, 3, 4 Million cells @191 hp*

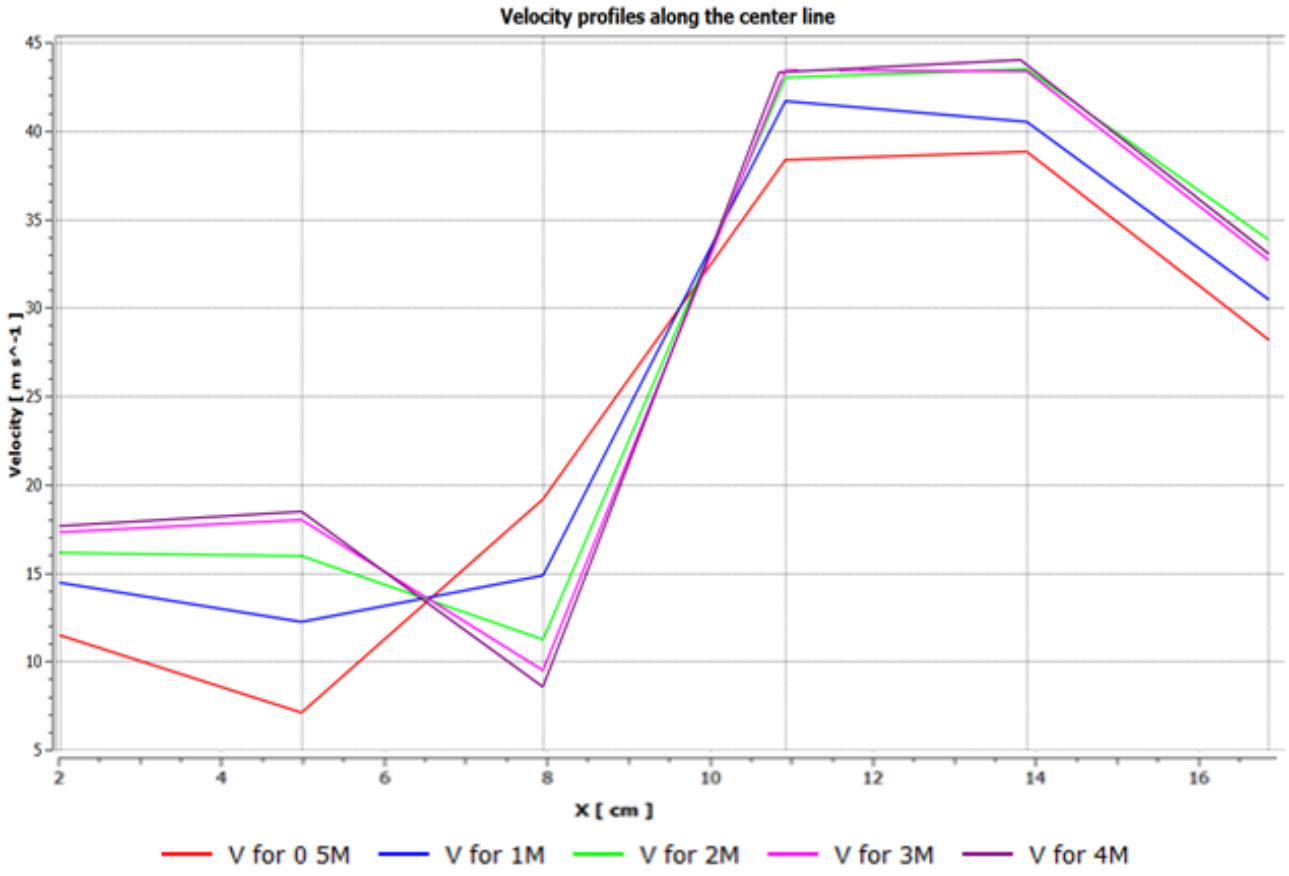

Figure 3.15 *Velocity profiles along the center line for mesh with 0.5, 1, 2, 3, 4 Million cells @191 hp*

As we can easily see, a grid of 3 million cells is a good compromise between maintaining low computation time and having good accuracy. Using only 500 thousand cells the error we get is pretty big, both for temperature and velocity profiles. Increasing gradually the mesh quality, values closer and closer to each other are reached.

Similar observations could be also made by analyzing other profiles in different areas of the combustion chamber.

3.3.2 Named selections

The boundary conditions must be applied to different zone types. The zone types are defined from the zone names. So, we have named all the surfaces and orifices in accordance with this principle (Figure 3.16). The Figure will also make easier the zone types identification when we speak about the air flow distribution in section 3.4.3.

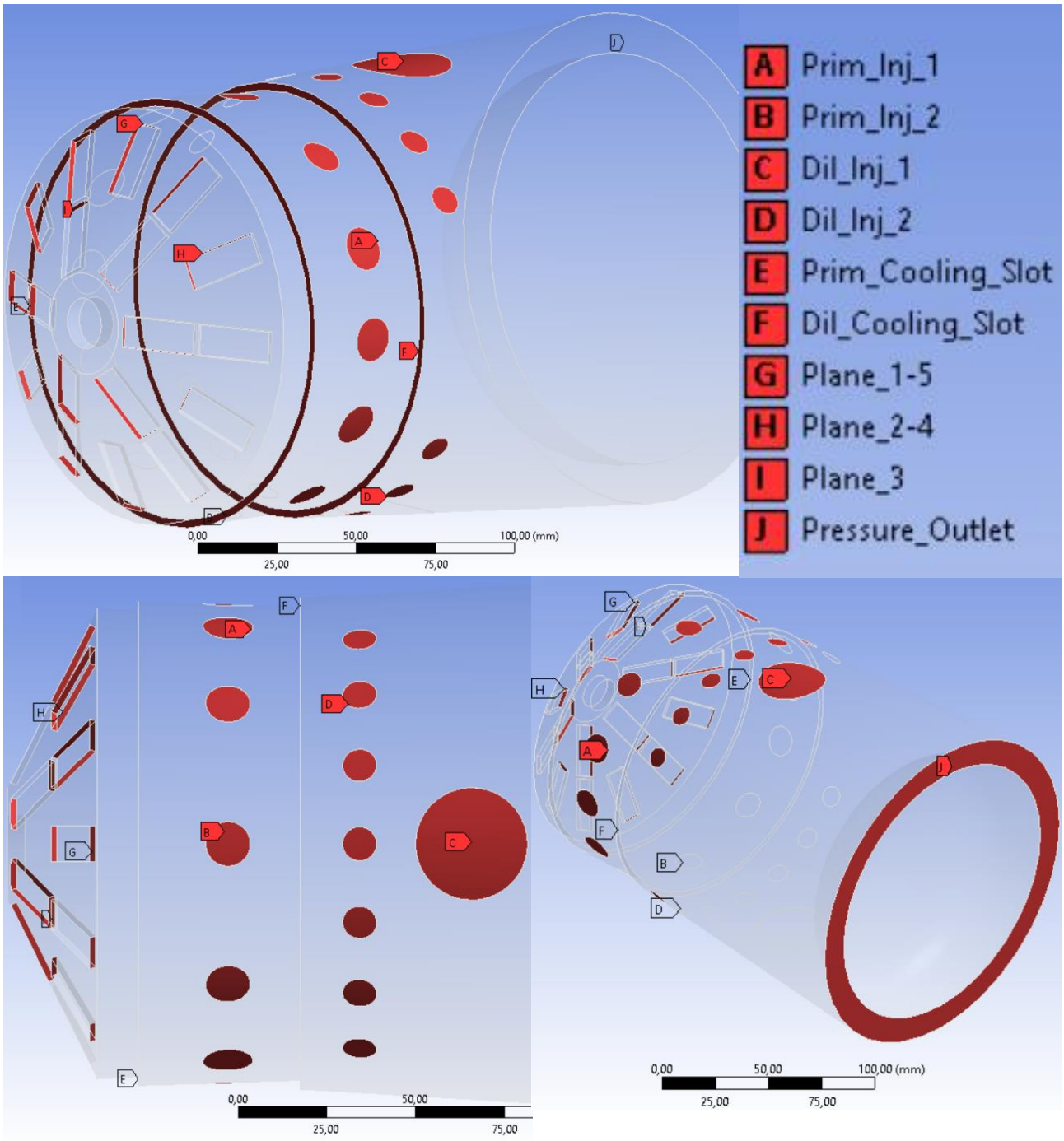

Figure 3.16 *Names of the surfaces and orifice on which the boundary condition must be set*

3.4 Boundary conditions

New experimental data imply new fuel flows, air flows, compressor exit temperatures, compressor exit pressures and different reference powers. All the data chosen for this thesis work as boundary conditions are resumed in table 3a-e. We have chosen five cases with powers very close to the literature data used in the Emicopter project [4] to produce results easier to compare.

a) SHP=26 hp	***Imperial***		***Metric***	
Airflow Rate	1,543	lb/s	0,7	kg/s
Fuel Flow rate	0,0176	lb/s	0,008	kg/s
Air Fuel Ratio (AFR)	87,67	-	87,67	-
Power	26,8	SHP	20	kW
Compressor exit Temperature	875	°R	415	K
Compressor exit Pressure	747	Psia	2,54	atm
Combustor exit Temperature	1530.0	°R	850	K

b) SHP=191 hp	***Imperial***		***Metric***	
Airflow Rate	2,69	lb/s	1,22	kg/s
Fuel Flow rate	0,0432	lb/s	0,0196	kg/s
Air Fuel Ratio (AFR)	62,39	-	62,39	-
Power	191	SHP	144	kW
Compressor exit Temperature	935	°R	519	K
Compressor exit Pressure	74	Psia	5,04	atm
Combustor exit Temperature	1956.6	°R	1087	K

c) SHP=323 hp	***Imperial***		***Metric***	
Airflow Rate	3,25	lb/s	1,48	kg/s
Fuel Flow rate	0,0596	lb/s	0,027	kg/s
Air Fuel Ratio (AFR)	54,60	-	54,60	-
Power	323	SHP	244	kW
Compressor exit Temperature	995	°R	552	K
Compressor exit Pressure	95,3	Psia	6,49	atm
Combustor exit Temperature	2160	°R	1200	K

d) SHP=414 hp	***Imperial***		***Metric***	
Airflow Rate	3,62	lb/s	1,64	kg/s
Fuel Flow rate	0,0711	lb/s	0,0323	kg/s
Air Fuel Ratio (AFR)	50,89	-	50,89	-
Power	414	SHP	312	kW
Compressor exit Temperature	1030	°R	572	K
Compressor exit Pressure	109,1	Psia	7,42	atm
Combustor exit Temperature	2331	°R	1295	K

e) SHP=450 hp	*Imperial*		*Metric*	
Airflow Rate	3,82	lb/s	1,73	kg/s
Fuel Flow rate	0,0766	lb/s	0,0347	kg/s
Air Fuel Ratio (AFR)	49,87	-	49.87	-
Power	450	SHP	335	kW
Compressor exit Temperature	1039	°R	577	K
Compressor exit Pressure	116	Psia	7,9	atm
Combustor exit Temperature	2430	°R	1350	K

Table 3a-e *Operating and boundary conditions of the test cases studied*

To better understand improvements, we compared these new data (marked as New in plots) with old ones coming from the literature (Emicopter project [4]).

As we can easily see in the Figures 3.17a-e below, now the boundary conditions fitted perfectly the experimental data (flights 1734–1735–1736). The whole engine efficiency gets a well fitted trend as well. The experimental data collected over 1000 ft has been omitted to have a clearer view on the figures.

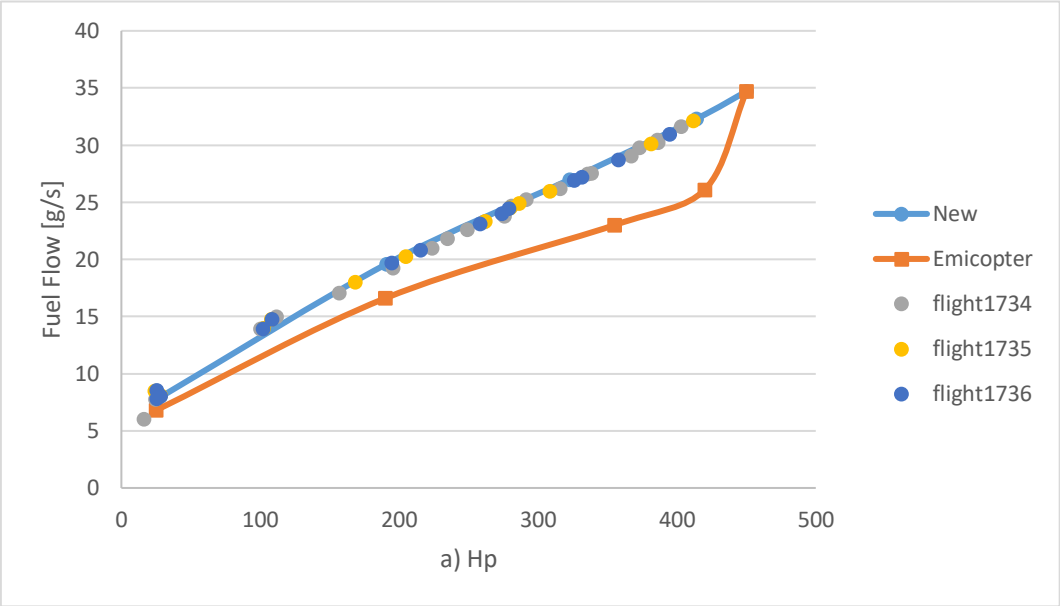

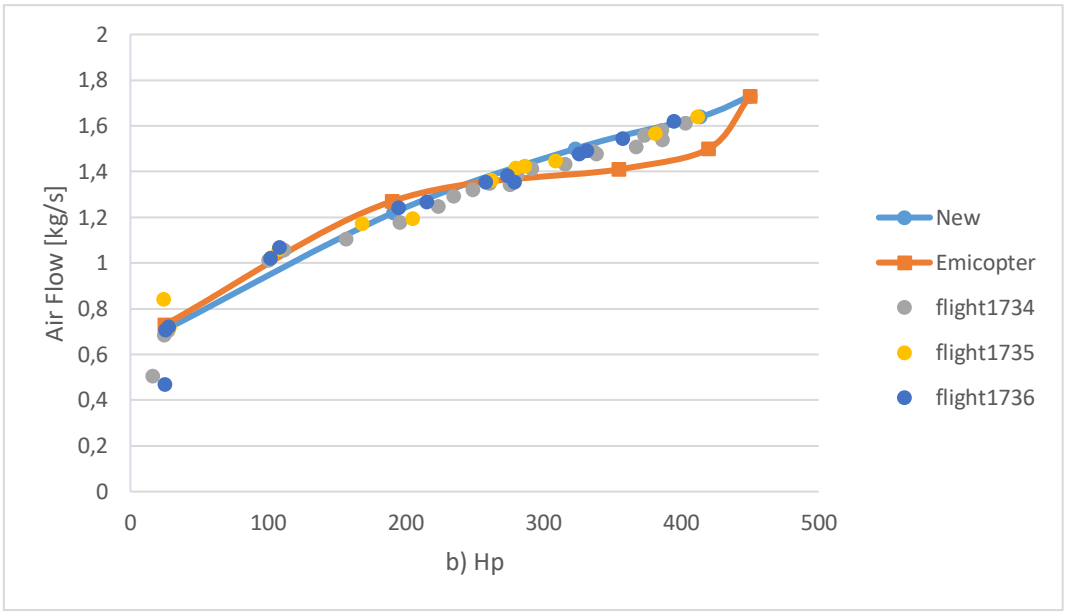
Air Flow [kg/s]
2
1,8
1,6
1,4
1,2
1
0,8
0,6
0,4
0,2
0
0
100
200
300
400
500
b) Hp
New
Emicopter
flight1734
flight1735
flight1736

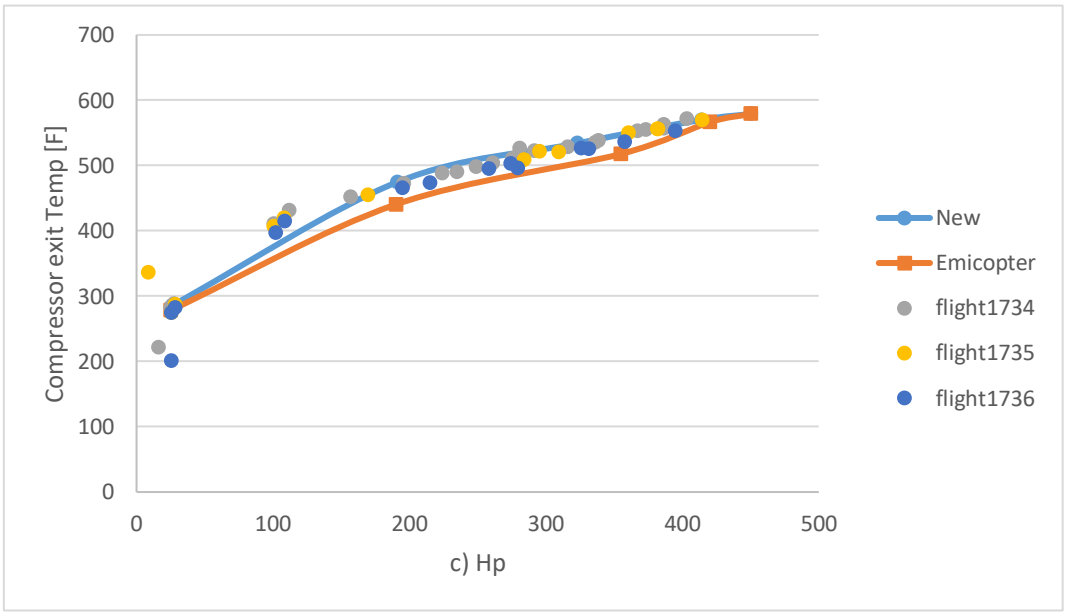
Compressor exit Temp [F]
700
600
500
400
300
200
100
0
0
100
200
300
400
500
c) Hp
New
Emicopter
flight1734
flight1735
flight1736

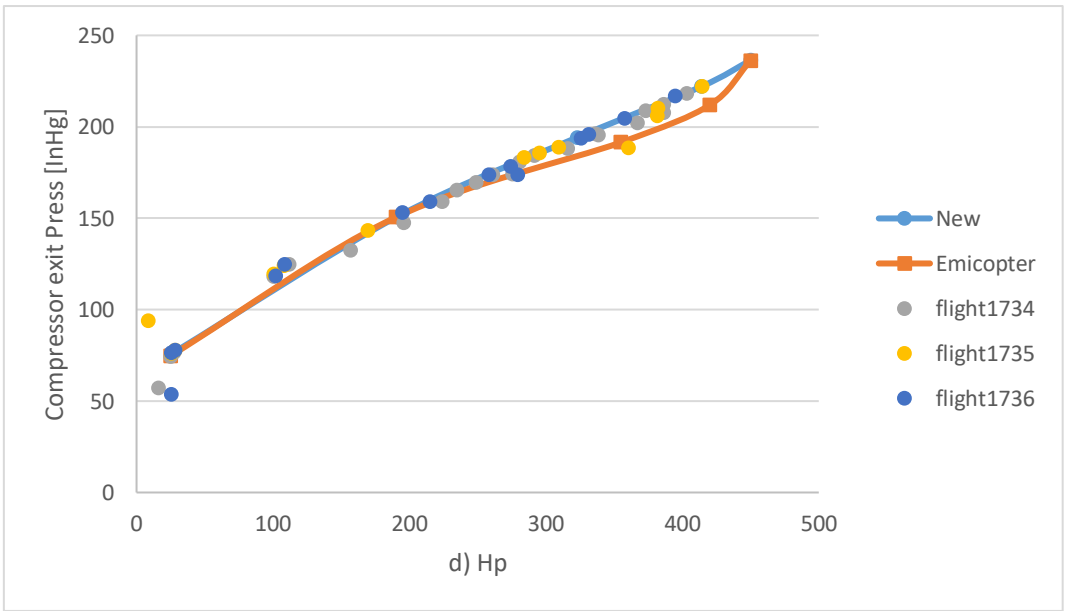
Compressor exit Press [InHg]
250
200
150
100
50
0
0
100
200
300
400
500
d) Hp
New
Emicopter
flight1734
flight1735
flight1736

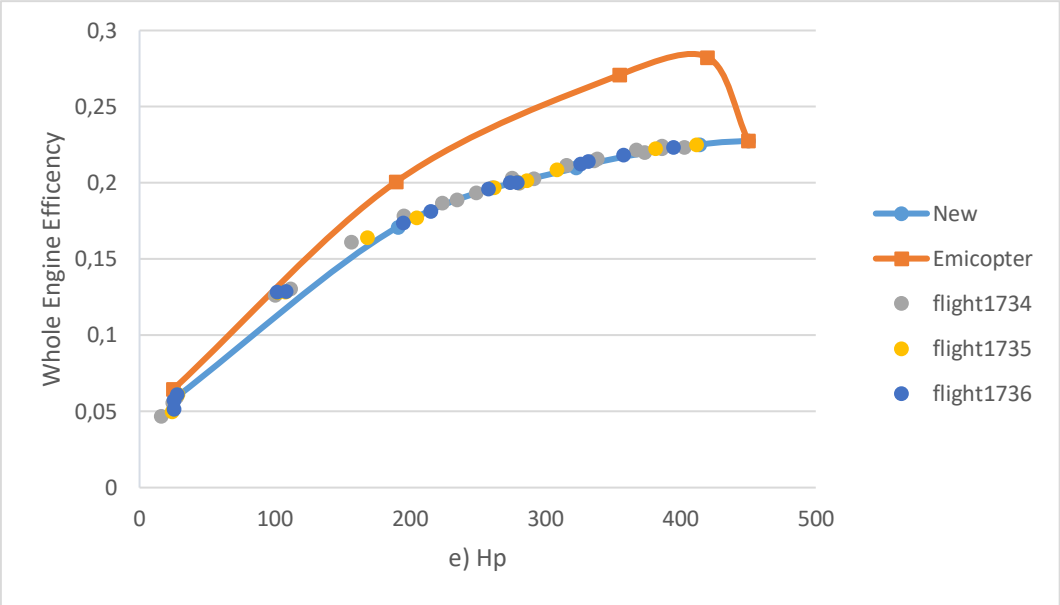

Figure 3.17a-e *Experimental data taken from flights 1734-1735-1736 compared with the Emicopter project [4] boundary conditions and the new ones. a) fuel flow [g/s] b) air flow [kg/s] c) compressor exit temperature [F] d) compressor exit pressure [inHg] e) whole engine efficiency*

We also have added two new cases concerning data collected at 8000 feet (Table 4a-b and Figure 3.18a-b). This choice is because different height means different flight conditions. Our purpose is to generate a model able to predict good value in any case and in any situations.

a) SHP=214 hp	***Imperial***		***Metric***	
Airflow Rate	2,44	lb/s	1,11	kg/s
Fuel Flow rate	0,0418	lb/s	0,0190	kg/s
Air Fuel Ratio (AFR)	58,29	-	58,29	-
Power	214,1	SHP	162	kW
Compressor exit Temperature	936	°R	520	K
Compressor exit Pressure	69,0	Psia	4,70	atm
Combustor exit Temperature	2,44	°R	1,11	K

b) SHP=332 hp	***Imperial***		***Metric***	
Airflow Rate	2,87	lb/s	1,30	kg/s
Fuel Flow rate	0,0570	lb/s	0,0258	kg/s
Air Fuel Ratio (AFR)	50,29	-	50,29	-
Power	332,6	SHP	251	kW
Compressor exit Temperature	1006	°R	559	K
Compressor exit Pressure	85,5	Psia	5,82	atm
Combustor exit Temperature	2,87	°R	1,30	K

Table 4a-b *Operating and boundary conditions of the test cases studied at 8000 feet*

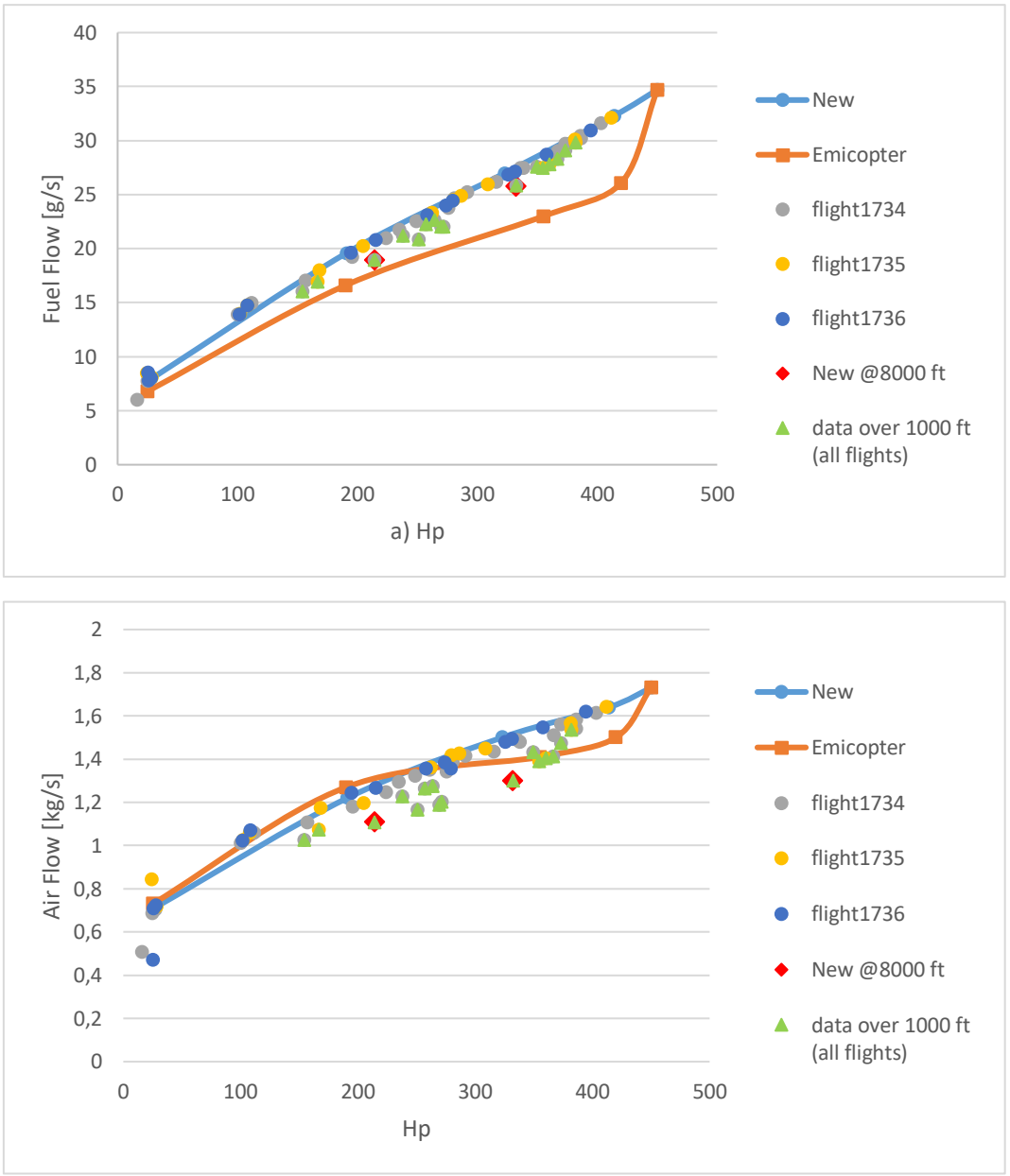

Figure 3.18a-b *Experimental data taken from flights 1734-1735-1736 compared with the Emicopter project [4] boundary conditions and the new ones at 8000 ft. a) fuel flow [g/s] b) air flow [kg/s]*

We have chosen, as reference, data at 8000 feet just because our intention is to analyze the model in the worst conditions.

What we can notice is a lower consumption of fuel and a lower air flow. This consideration may open new analysis scenarios, for example evaluations whether it is better to fly at low altitude or climb and fly at high altitude.

Concerning spray combustion modeling, it is required to specify the operating conditions for the continuous phase (gaseous phase) and the discrete phase (liquid droplets). The air flow distribution inside the liner is also a fundamental parameter that will be discussed in the following section 3.4.3.

3.4.1 Spray injection

A Discrete Phase Model (DPM) with 3D injection has been employed for the fuel injection.

Actually, liquid fuel is pumped from the tank to the combustion chamber, where through a nozzle it is atomized, thus creating a spray of particles, whose size and shape are statistically distributed. In our simulations the atomization stage has been neglected, because of poor information about injector, and has been replaced by direct injection of spherical particles with a uniform diameter of 50 µm, in accordance with Naegeli [47].

Table 5 summarizes features of spray in the moment of injection (fuel flow @450 hp).

Spray angle	45 $[°]$
Injector diameter	1 $[mm]$
Dispersion angle	0 $[°]$
Injection temperature	300 $[K]$
Flow	0.0347$\left[\frac{Kg}{s}\right]$
Velocity	47$\left[\frac{m}{s}\right]$

Table 5 *Initial conditions of fuel spray (@450 hp)*

We must set also the particles number that will be injected and specify the type of particle.

The particle types available depend on the range of physical models that we have defined. For our model, we have chosen the droplet model.

A droplet particle is a liquid droplet in a continuous-phase gas flow that obeys the force and that experiences heating/cooling via Law 1 followed by vaporization and boiling via Laws 2 and 3 (see chapter 2, section 2.4).

About the number of particles injected let's do some estimations to understand the order of magnitude. Considering the fuel mass flow injected (m), the number of incoming particles into the system (@ t=1 ms) is:

$$Nparticles(t) = \frac{m\,t}{\rho\,\frac{\pi\,d^3}{6}} \approx 700000 \tag{3.1}$$

Obviously, this number is prohibitive for the simulation. To obtain a good agreement between results and calculation time we set 20 the Number of Continuous Phase Iterations, that allows you to control the frequency at which the particles are tracked, and 100 for the number of particles injected.

In Figure 3.19 an example of velocity profile, diameter and residence time of particles inside the combustion chamber is reported.

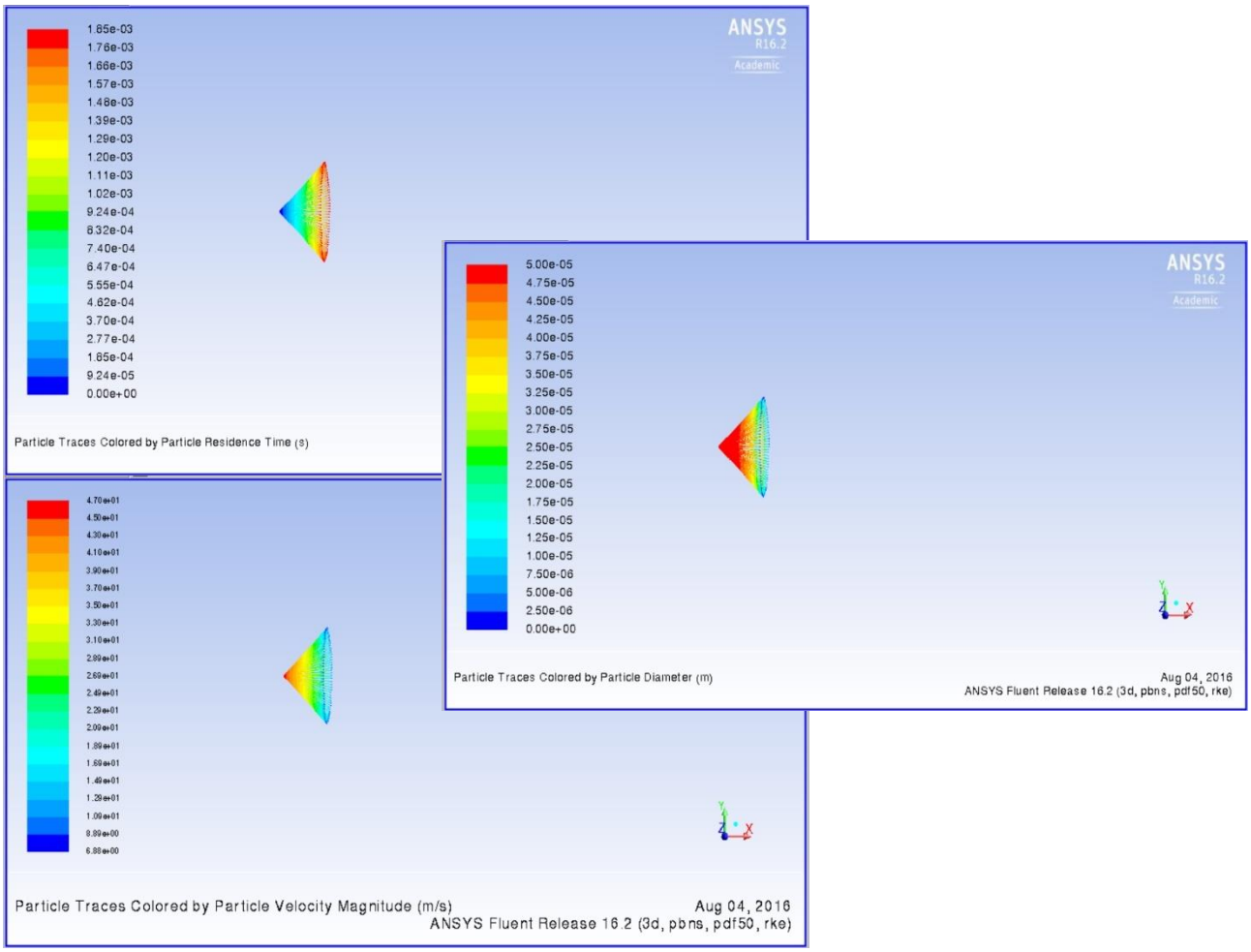

Figure 3.19 *Velocity profile [m/s], residence time [s] and particles diameter [m] of the fuel particles injected into the combustion chamber as evaluated with Fluent*

3.4.2 Fuel properties

Always depending on crude source and the refinery process, kerosene is a complex mixture in the C9–C15 fraction with a distillation range 140–300 °C.

Kerosene-type jet fuels are relatively nonvolatile, and the major components are linear and branched alkanes (35%–50%), cycloalkanes (30%–35%), and one and two-ring aromatics (20% to 25%). Jet fuels are blends of kerosene streams, sometimes supplemented with naphtha and low concentrations of additives to improve stability and performance. All jet fuels must be free of water and must be pumpable at very low temperatures and stable at higher temperatures [48].

Common aviation fuels, used both for commercial and military aircraft, include Jet A, Jet A-1, and JP-8.

Table 6 reports the average physical properties of liquid fuel (Kerosene) taken from Fluent material database (@298 K and 1 atm).

$\boldsymbol{\rho_d}$	780 $\left[\frac{kg}{m^3}\right]$
$\boldsymbol{cp_d}$	2090 $\left[\frac{J}{Kg\ K}\right]$
$\boldsymbol{\lambda_{T,d}}$	0.149 $\left[\frac{w}{m\ K}\right]$
$\boldsymbol{Dh_{ev}}$	226000 $\left[\frac{J}{Kg}\right]$
$\boldsymbol{T_{eb}}$	477 $[K]$
$\boldsymbol{D}$	3.79 e-06 $\left[\frac{m^2}{s}\right]$
$\boldsymbol{P^0}$	1329 $[Pa]$

Table 6 *Average physical properties of kerosene at room temperature and pressure (T=298 K, p=1 atm)*

These properties considerably influence the rate of heating and evaporation of droplets inside the combustion chamber, thus this is the reason why it is necessary to introduce, for the most significant properties, the dependence on temperature and pressure. Those properties are the specific heat, the latent heat of vaporization, the boiling temperature and vapor pressure; the latter two are an index of fuel volatility.

Vapor pressure $P^0(T)$ [mmHg] is evaluated with the following expression:

$$Log\ P^0(T) = A + \frac{B}{T} + CLog(T) + DT + eT^2 \tag{3.2}$$

where:

$$A = -50{,}5512 \quad B = -2705{,}3 \quad C = 28{,}273 \quad D = -0{,}045702 \quad E = 0{,}000020443$$

The function is plotted in Figure 3.20.

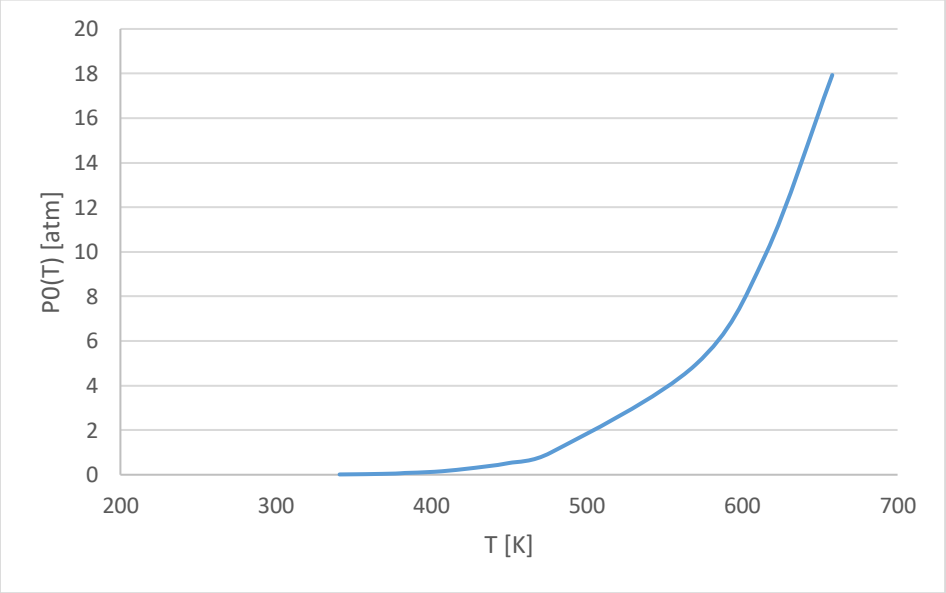

Figure 3.20 *Vapor pressure trend of the fuel (kerosene) with the temperature*

Through a regression, values of the constants to insert in Fluent polynomial expression have been obtained. That expression is defined as:

$$P^0(T) = A + BT + CT^2 + DT^3 + ET^4 \tag{3.3}$$

where:

$$A = 2553029 \quad B = 29258 \quad C = 126{,}046 \quad D = -0.2423636 \quad E = 0.00017582$$

Similar considerations have been made for the specific heat of the liquid phase. The dependency of specific heat on temperature is reported in the following:

$$cp_d(T) = 2983.54 - 8.03520\ T + 0.0182079\ T^2 \quad (3.4)$$

In Figure 3.21 the trend of the specific heat is reported.

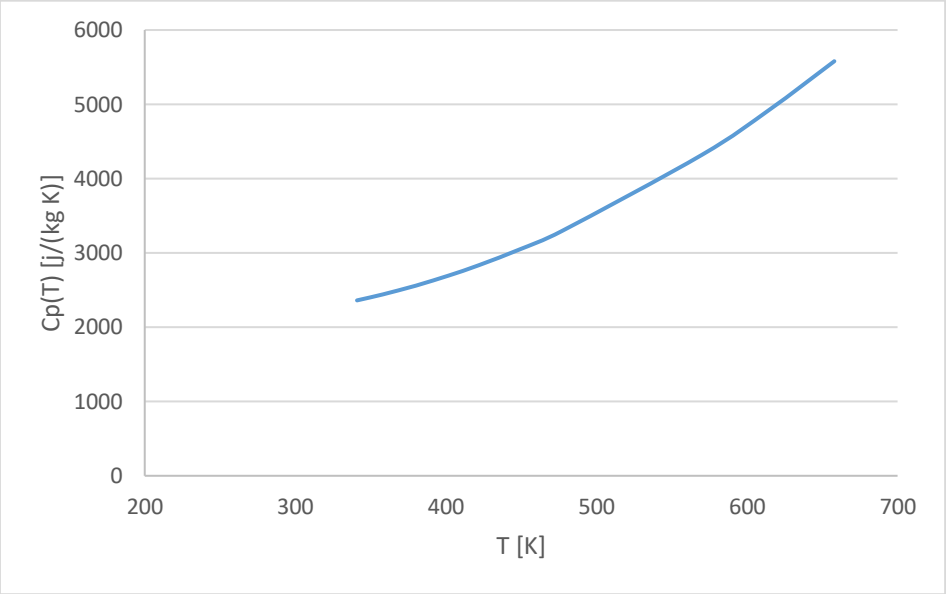

Figure 3.21 *Trend of the specific heat of liquid fuel (kerosene) with temperature*

As regards the latent heat of vaporization Dh_{ev}, Fluent allows to insert only a constant value. It varies from 226000 [J/Kg] at the temperature of 300 K and 175000 [J/Kg] at the temperature of 596 K. For the simulations, a constant average value of 200000 [J/Kg] has been then adopted.

In this thesis work we have used the flamelet model so, in addition to defining the physical properties of the fuel, we have had to define also chemical composition of kerosene. To do that we use a surrogate mixture to mimic the properties of aviation fuel.

We have adopted the surrogate proposed by Humer (surrogate C) [49], which composition is report in the Figure 3.22.

	Surrogate Components	Humer [%]
Normal alkanes	*n*-Octane *n*-Decane *n*-Dodecane *n*-Tetradecane *n*-Hexadecane	46.0
Branched-alkanes	Isooctane Isocetane	
Cycloalkanes	Methylcyclohexane Decalin	27.7
Aromatics	Toluene Xylene 1,2,4-TMB *n*-Propylbenzene Butyl-benzene 1-Methyl-naphthalene tetralin	26.3
Average molecular weight		133.2
H/C ratio		1.93

Figure 3.22 *Kerosene composition supposed by Humer [49]*

Before getting this surrogate C, we have compared it with others (Aachen and Princeton [50]) to understand if this choice could affect our results.

We can notice that, for a reference power of 191 hp, all the surrogate taken in account are able to predict quite similar values of CO_2, O_2 and H_2O [ppm]. The results that are reported below (Figure 3.23) will be better understood in the following Chapter 4.

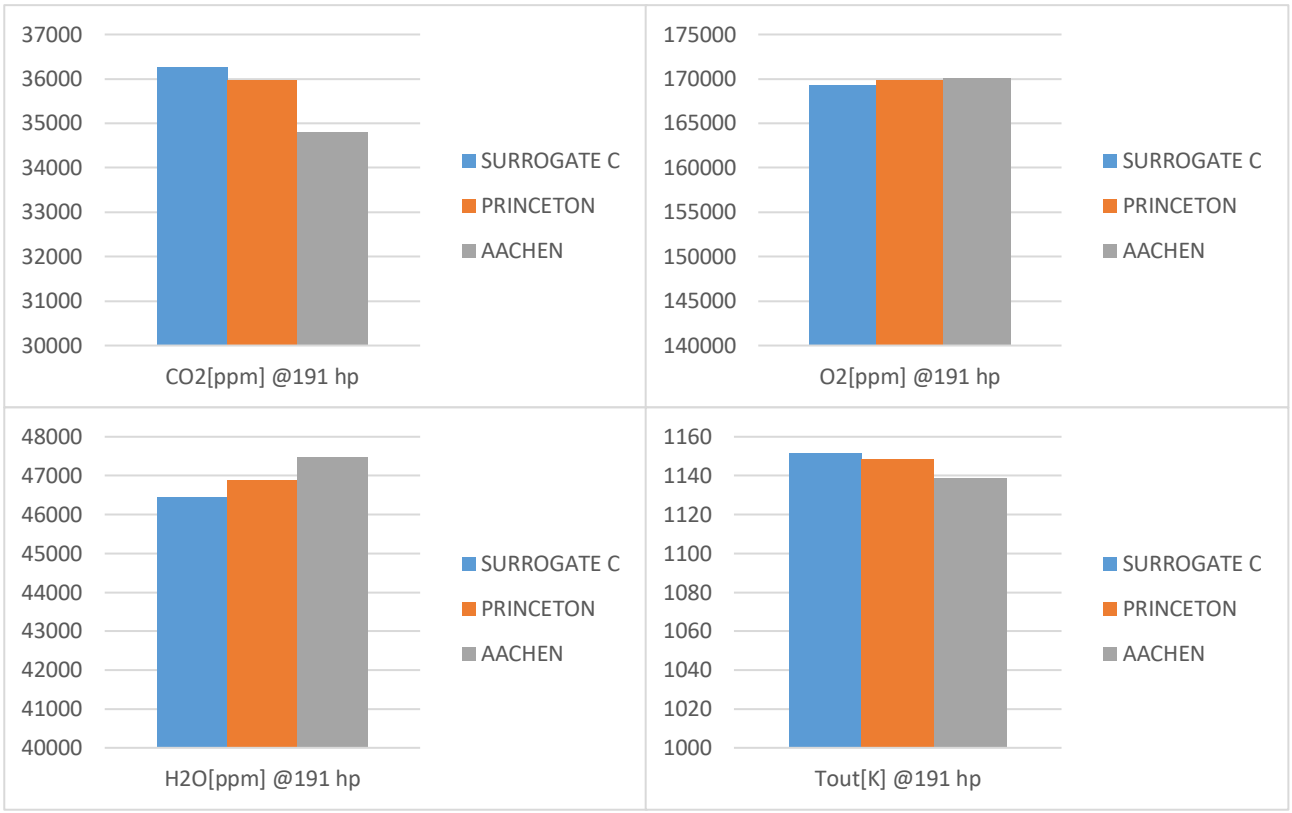

Figure 3.23 *Effect of surrogate composition*

3.4.3 Air flow distribution

Estimations of the air flow distribution of the combustion zone assumes that the pressure is uniformly distributed around the combustor liner with the compressor discharged stagnation pressure. This assumption is obtained from the design criteria for a compressor diffuser where ‘’the discharged air pressure is fully recovered and the pressure is uniformly distributed around the combustor liner’’ as discussed in Lefebvre [51].

The flow slit around the combustion zone has been estimated using Eddy Dissipation combustion model. The predicted mass flow distribution is further justified in comparison to conventional design parameters from literature (Mellor [52]).

For a total engine mass flow, the Eddy Dissipation model has predicted 87% of the airflow through the combustor [46].

Airflow distribution around the combustor liner is predicted based on the engine performance parameters, and the results of the simulations have been applied as boundary conditions for the CFD simulation.

For a total air flow of 1,73 [kg/s] (ref. @450 hp), the airflow distribution is reported in the Table 7 below:

AIR INLET	FLOWS $\left[\frac{Kg}{s}\right]$
Swirler plan 1 and 5	0.0359
Swirler plan 2 and 4	0.0854
Swirler plan 3	0.0098
Primary zone cooling slot	0.1867
Primary injection holes 1	0.2030
Primary injection holes 2	0.1575
Dilution zone cooling slot	0.2556
Dilution injection holes 1	0.3773
Dilution injection holes 2	0.1999
	TOT: 1.511

Table 7 *Distribution of air flows entering the combustor @450 hp*

To check this air distribution, a simple sensitive analysis has been performed. The basic idea is to control if there are differences between the air distribution based on Eddy Dissipation model and the one based on holes' area fraction (calculated using as reference a total holes' area equal to 1). Results are reported in the Table 8, where the first case is marked blue and the second yellow.

	Area [Fract]	air flow [kg/s]	air flow [kg/s]
Plane 1 and 5	0,0366	0,0554	0,0359
Plane 2 and 4	0,0709	0,1072	0,0854
Plane 3	0,0104	0,0157	0,0098
Primary injection 1	0,1386	0,2094	0,203
Primary injection 2	0,0945	0,1429	0,1575
Dilution injection 1	0,2501	0,3780	0,3773
Dilution injection 2	0,1274	0,1925	0,1999
Primary cooling slot	0,1346	0,2034	0,1867
Dilution cooling slot	0,1367	0,2065	0,2556
SUM	1	1,511	1,511

Table 8 *Air distribution based on Eddy Dissipation model (blue) vs air distribution based on holes' area fraction (yellow) @450 hp*

It's possible to observe that the air distribution calculated assuming the complete geometry of the plenum by [46] is quite similar to the flow distribution which can be calculated simply on the basis of the relative areas of the holes. The results are therefore not significantly sensitive to the air flow distribution assumed as boundary conditions. Anyway, the suggestion of [46] was adopted in all the simulations.

Air flow streamlines have been also simulated using Fluent CFD-Post to better understand the characteristic path of the flow and the variation of the velocity profile along the liner combustor (Figure 3.24a-b). In figure 3.25 we can also see how the airflow comes in the swirler plan.

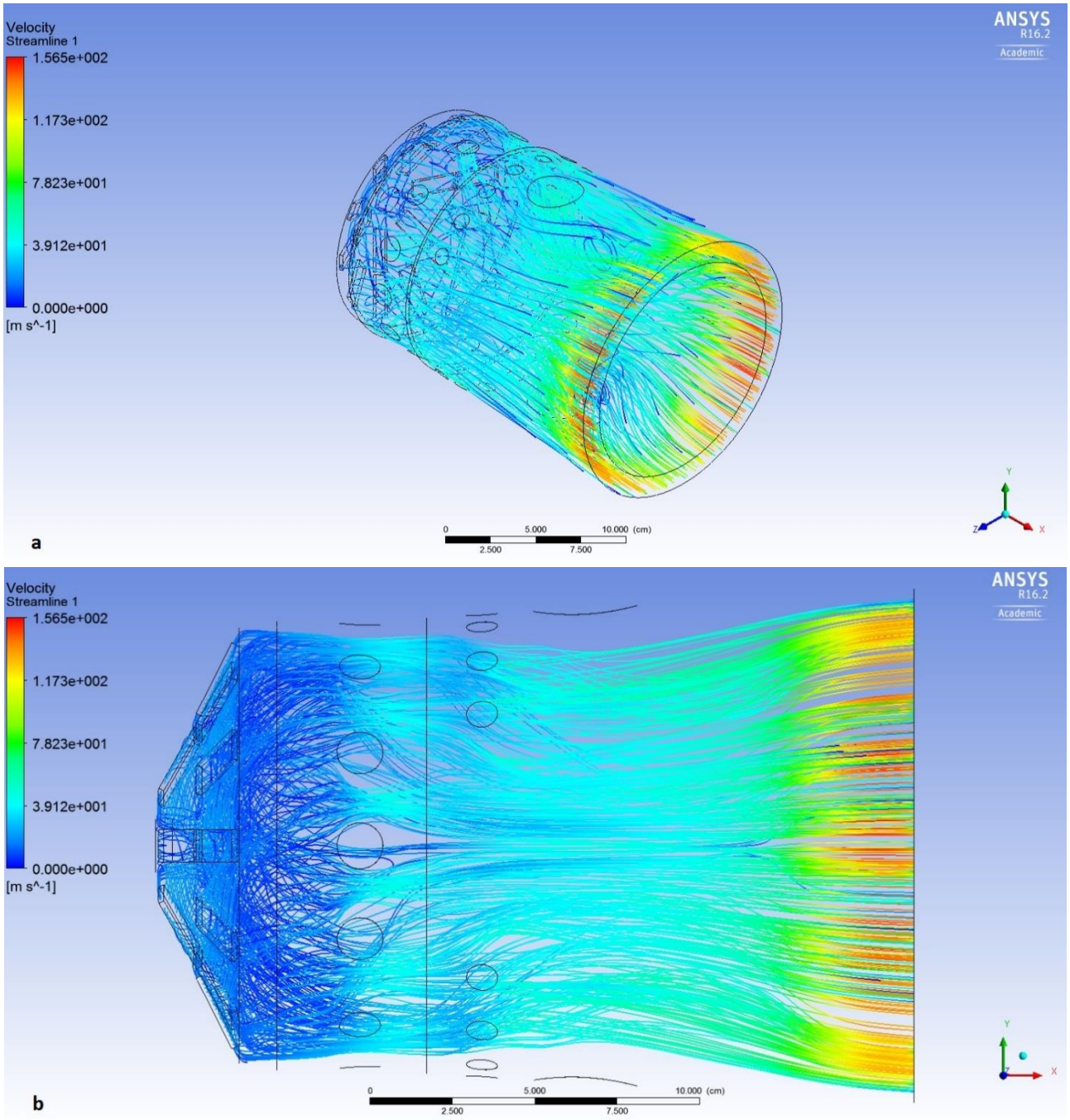

Figure 3.24a-b *Characteristic path of the flow and the variation of the velocity profile [m/s] along the liner combustor*

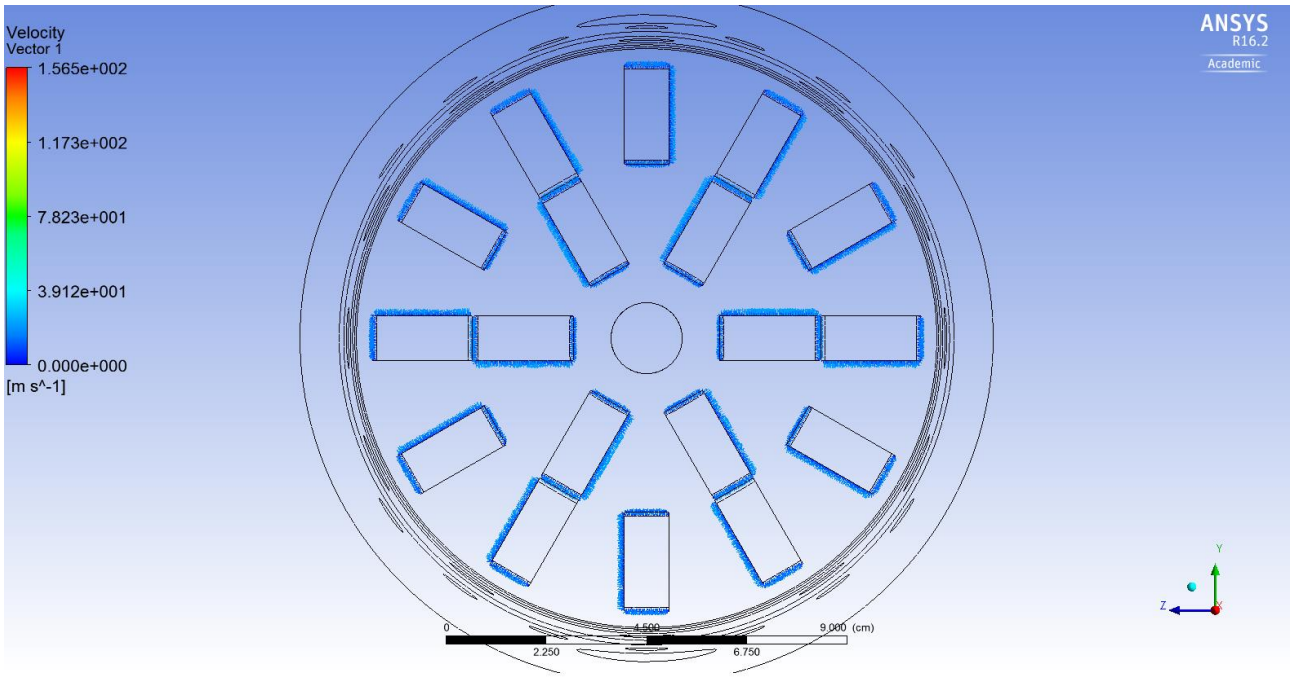

Figure 3.25 *How the airflow comes in the swirler plan*

3.4.4 Turbulence properties

In accordance with what we have said in Chapter 2, section 2.1.1, the turbulence model adopted in this thesis work is the realizable k-ε. The differences with the standard k-ε in terms of turbulence Eddy Dissipation and temperature profiles are reported below for the 191 hp reference case (Figures 3.26 and 3.27). We can notice that there are quite significant differences between the two models.

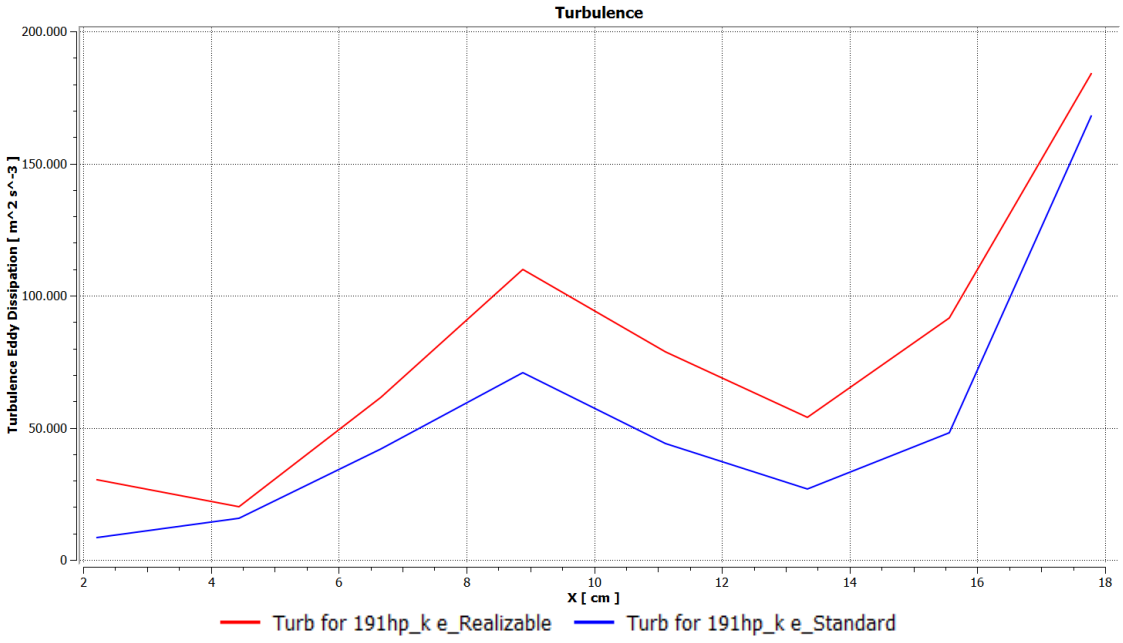

Figure 3.26 *Turbulence Eddy Dissipation profiles along the center line for realizable and standard k-ε model @191 hp*

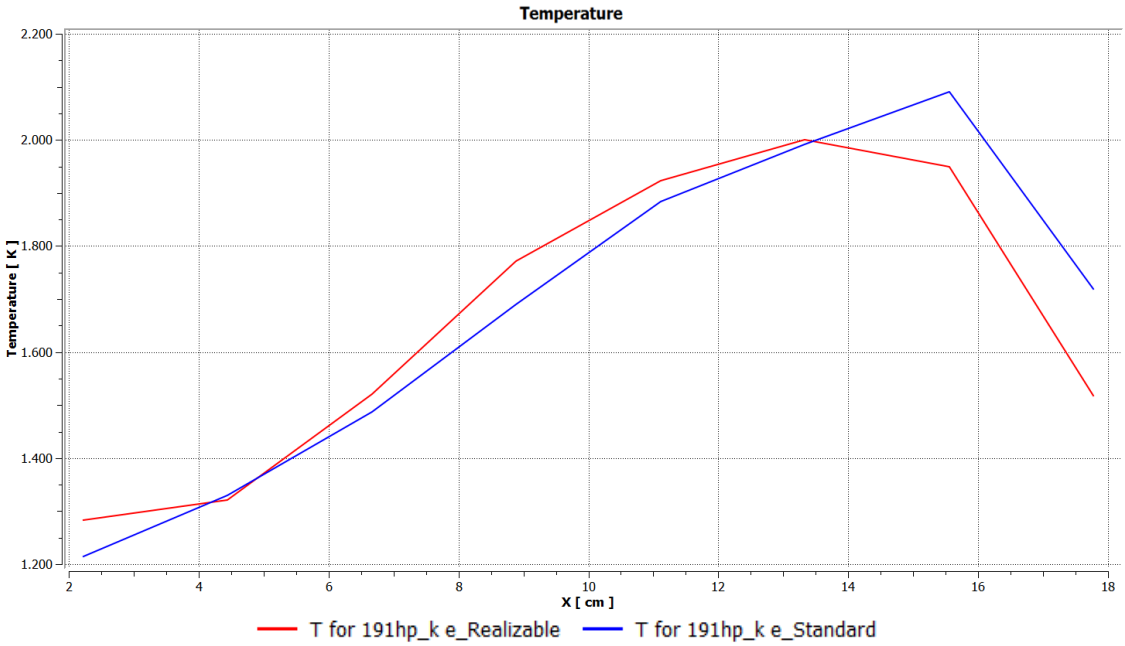

Figure 3.27 *Temperature profiles along the center line for realizable and standard k-ε model @191 hp*

As boundary conditions inherent to the turbulence model adopted (realizable k-ε), we have used specifications relating to the intensity of turbulence and to the hydraulic diameter.

The turbulence intensity is defined as:

$$I = \frac{u''}{\tilde{u}} \tag{3.5}$$

The value of the turbulence intensity equal to 10% is suitable to describe the turbulent flow within the combustor, as shown in [46]. It now remains to define the hydraulic diameter. The hydraulic diameter is a fluid quantity defined as the ratio of the wetted perimeter of the fluid (P_b), and the passage area (S) of the same:

$$D_h = \frac{4S}{P_b} \tag{3.6}$$

It corresponds, by definition, exactly to the diameter of a hole only if it has a circular shape. The hydraulic diameter for each air inlet is evaluated on the basis of the combustor geometry shown in section 3.2.

Chapter 4 – Results

In this Chapter, all the results obtained using Fluent are shown. Planes (XY, ZX) and center lines, used as reference for result reports, have been showed in Figure 3.12 (Chapter 3, section 3.2).

A summary table of the models and Fluent options used in this thesis work to produce the results is reported below (Table 9).

ENERGY:	ON
TURBULENCE MODEL: - k-ξ	 REALIZABLE
RADIATION:	P1
COMBUSTION: - NON-PREMIXED COMBUSTION	 STEADY FLAMELET
SPRAY: - BREAK UP - COLLISION - DRAG - EVAPORATION	 TAB O'ROUKE DYNAMIC 3 LAWS
POLLUTANT SPECIES: - NO - N_2O - CO	 PROMP + THERMAL TRASPORTED SIMPLE UNSTEADY FLAMELET
SOLUTION METHODS: - PRESSURE-VELOCITY COUPLING - SPATIAL DISCRETIZATION	 SIMPLE FIRST ORDER UPWIND

Table 9 *A summary table of the models and Fluent options used in this thesis work*

4.1 Global view

In this section, we report the results obtained for the continuous phase in terms of temperature, velocity, pressure and mass fraction fields.

In Figures 4.1 and 4.2 the growth of temperature profiles along the two symmetry planes (ZX, XY) are shown. For all the cases involved (from 26 hp to 450 hp), the same reference scale is set to better understand changes. A good tool able to make easier the comparison is the CFD-Post implemented in Ansys Workbench even if for some cases we have simply used Fluent graphical features.

As we can see, there is a noticeable change among profiles during the transition from low to high power. In the low-power case (26 hp) we notice colder temperatures and a profile less developed

while, on the other hand, increasing the power we notice that temperatures growth and profiles sharpness become more defined.

This will certainly influence the production of pollutants (especially thermal NO_x) and more generally all the temperature dependent parameters.

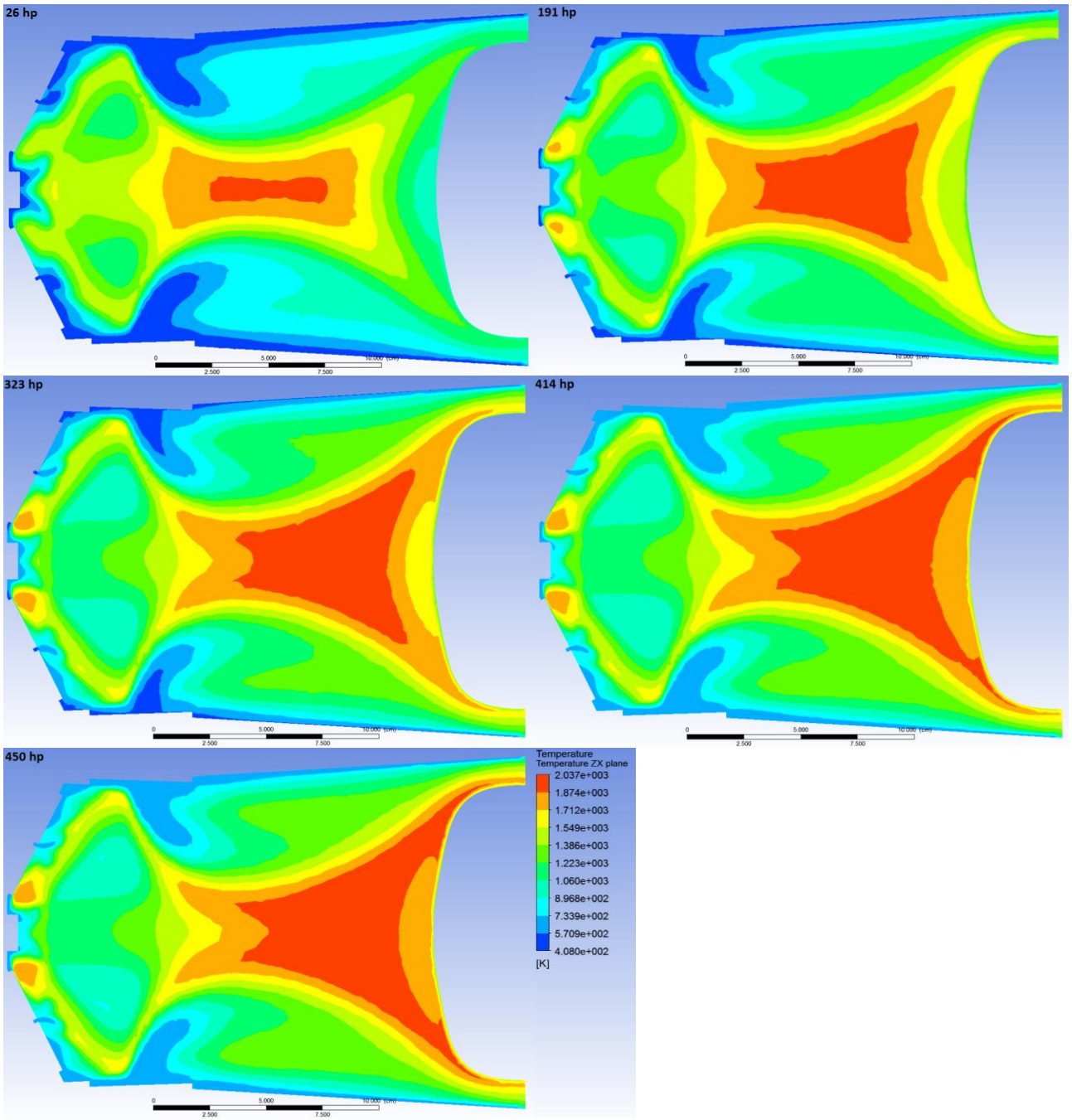

Figure 4.1 *Temperature profiles along the ZX plane*

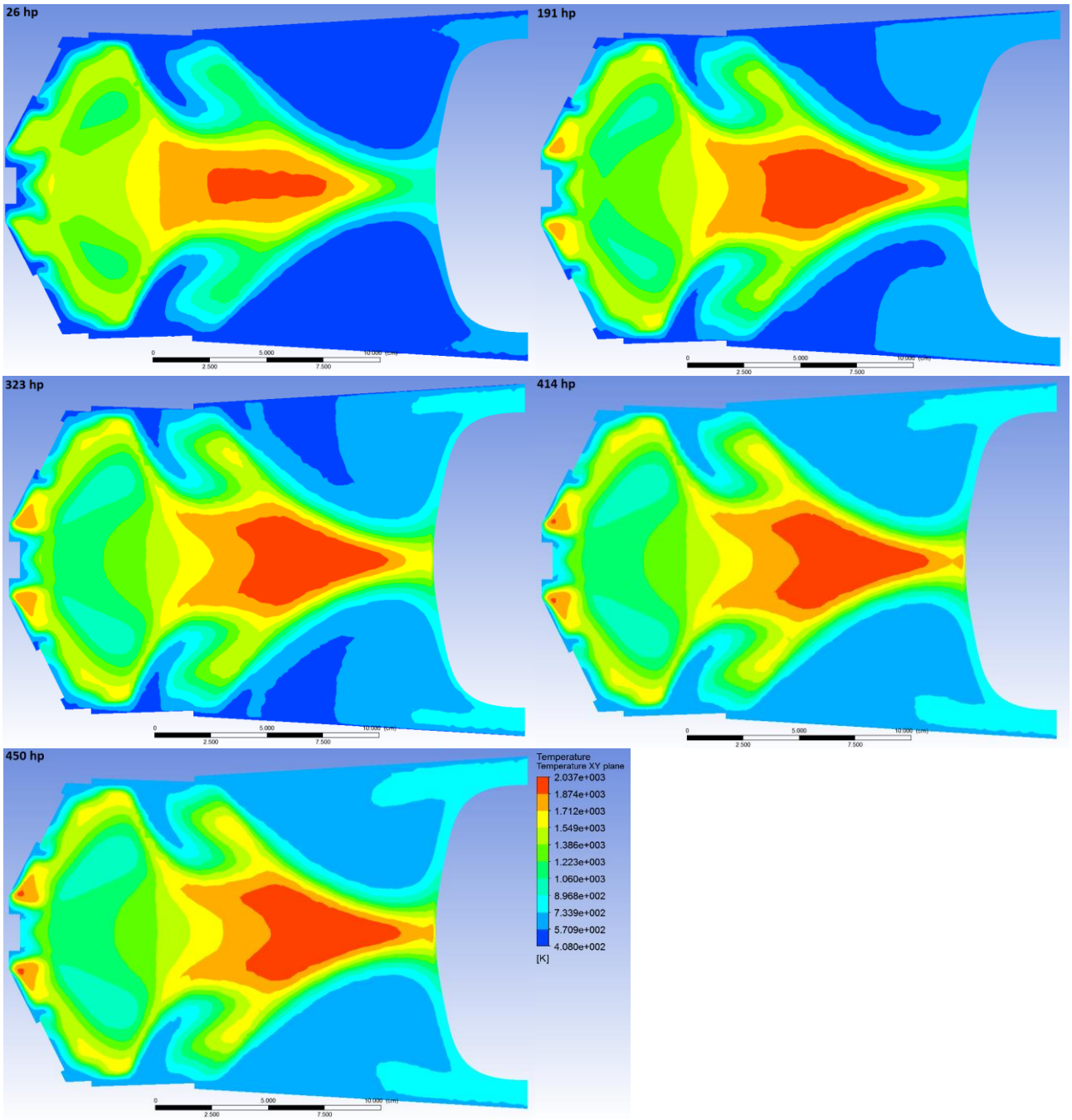

Figure 4.2 *Temperature profiles along the XY plane*

Increasing power, we see lower temperature peaks in the primary zone and higher ones in the secondary. Sharper profiles are noticeable too.

We analyzed also temperature profiles along the center line for different powers. The related chart, made on the comparison lines, is showed in the following (Figure 4.3).

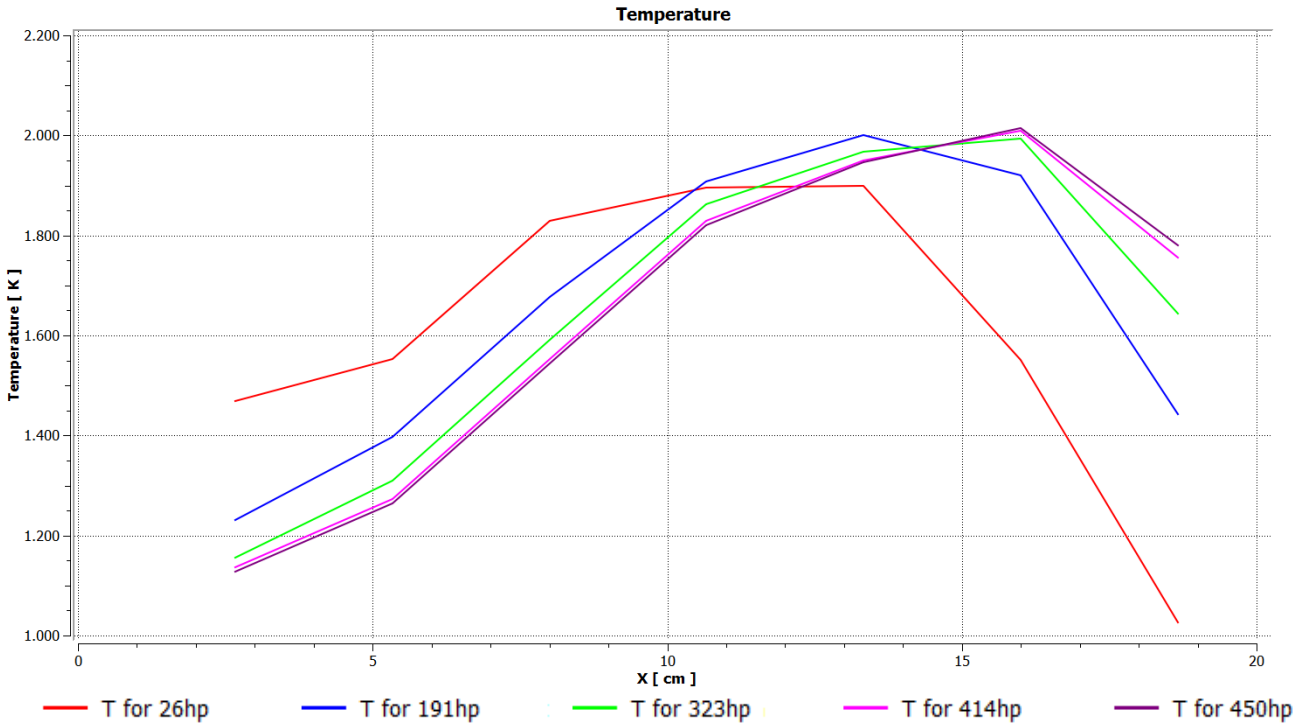

Figure 4.3 *Temperature profiles along the center line*

We can notice, as seen before in the Figures 4.1 and 4.2, that the temperature peak increases and moves away from the fuel inlet increasing power. Lower powers show higher temperatures at the beginning of the combustor liner while lower ones at the end.

The reason of this observation in this engine can be easily understood simply by considering that less power is associated with a higher air/fuel ratio. This state brings to a more diluted air system and, obviously, to lower temperatures. Moreover, just if we have less fuel inside the combustor chamber we will have, globally, lower temperatures due to a larger effect of heat losses.

To get a complete view of the temperature inside the liner, a 3D temperature volume rendering for the 450 hp case has been made and is reported below (Figure 4.4).

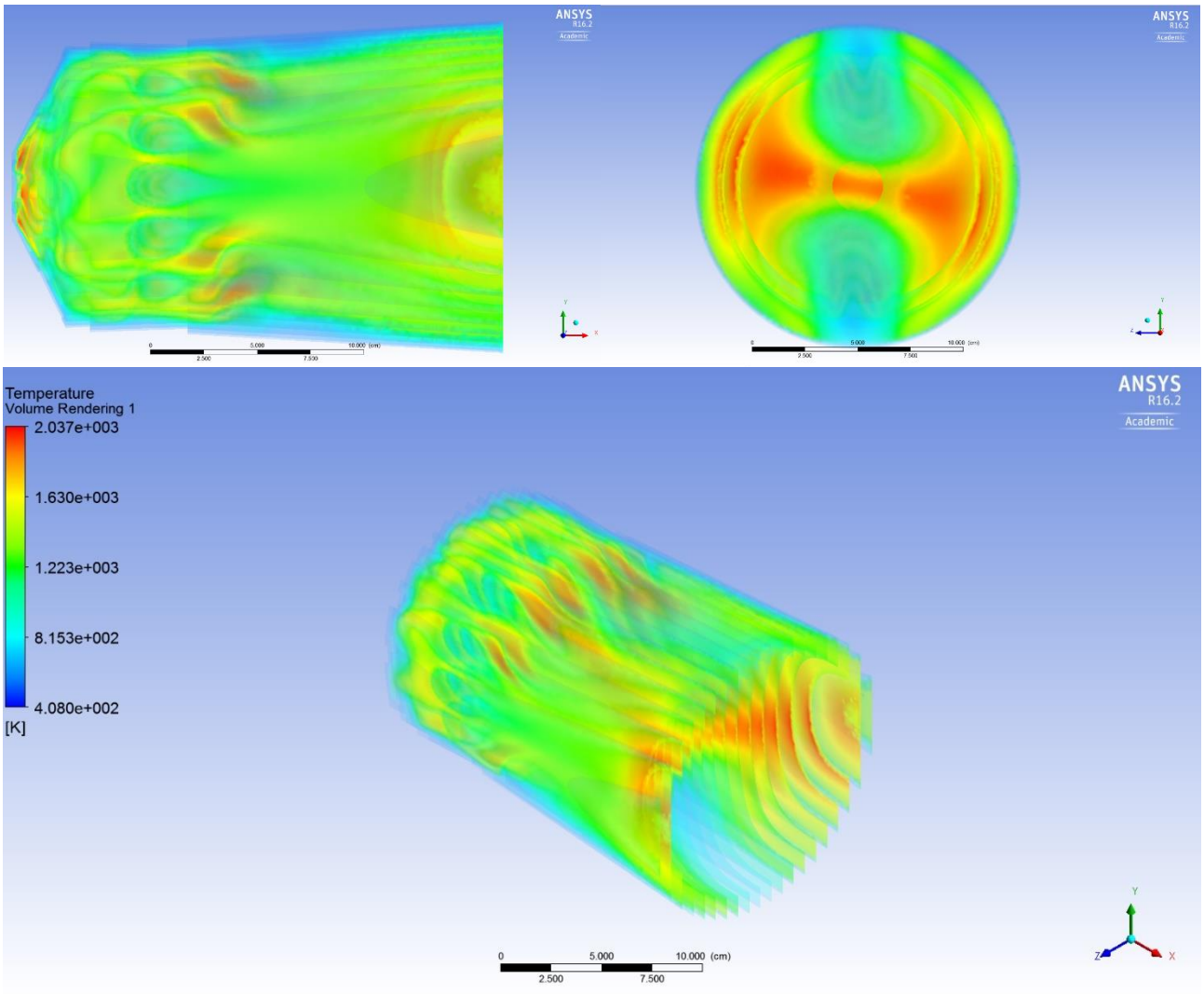

Figure 4.4 *3D temperature volume rendering for the 450 hp case*

Similarly to what seen before, Figures 4.5 and 4.6 reports the growth of velocity profiles and mixture fraction profiles along the ZX plane for all the powers.

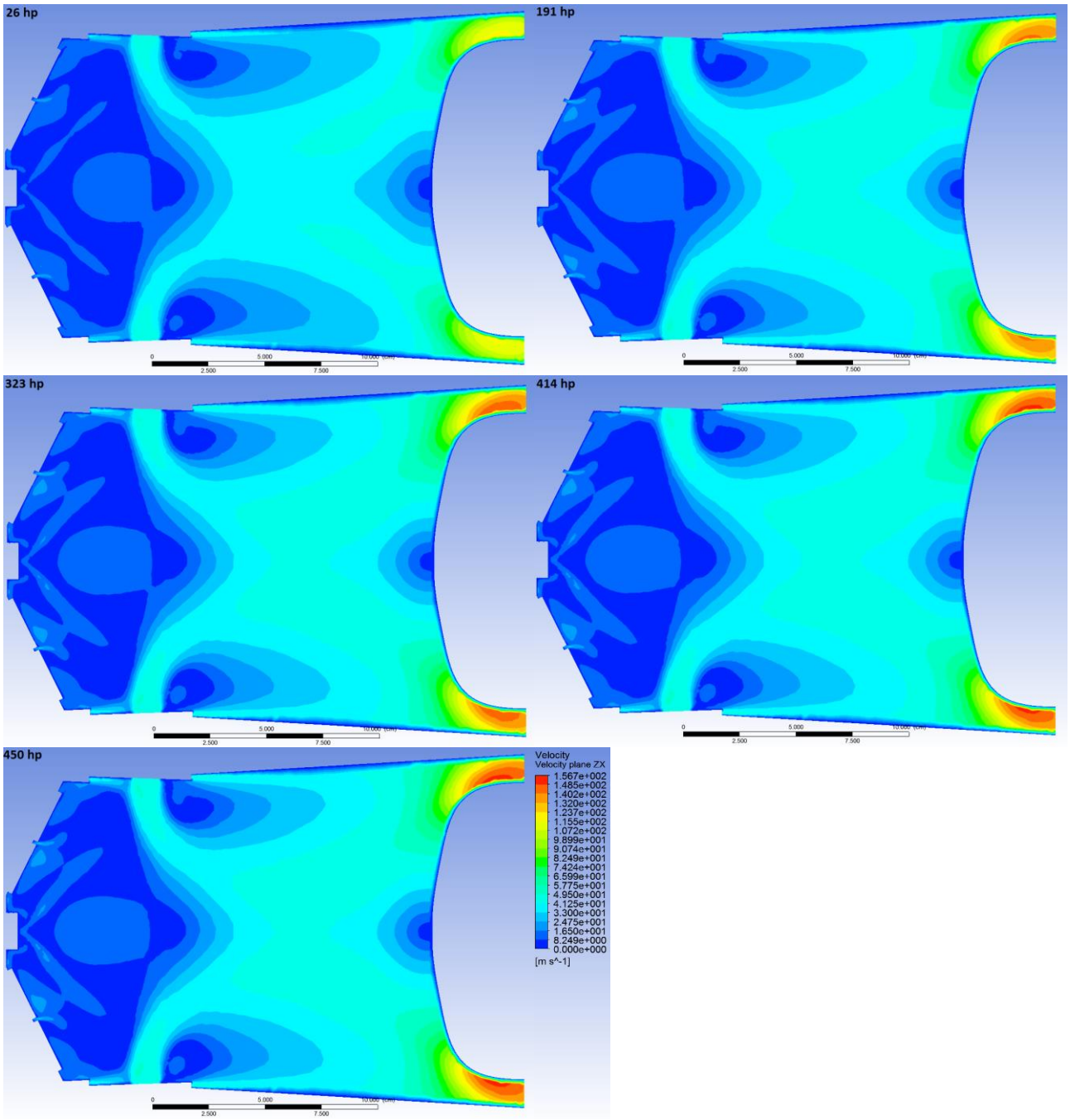

Figure 4.5 *Velocity profiles along the ZX plane*

We can notice an increase of the velocity with power growth. The maximum velocity is reached at the outlet, in the narrowing of the passage section caused by the presence of the turbine shield.

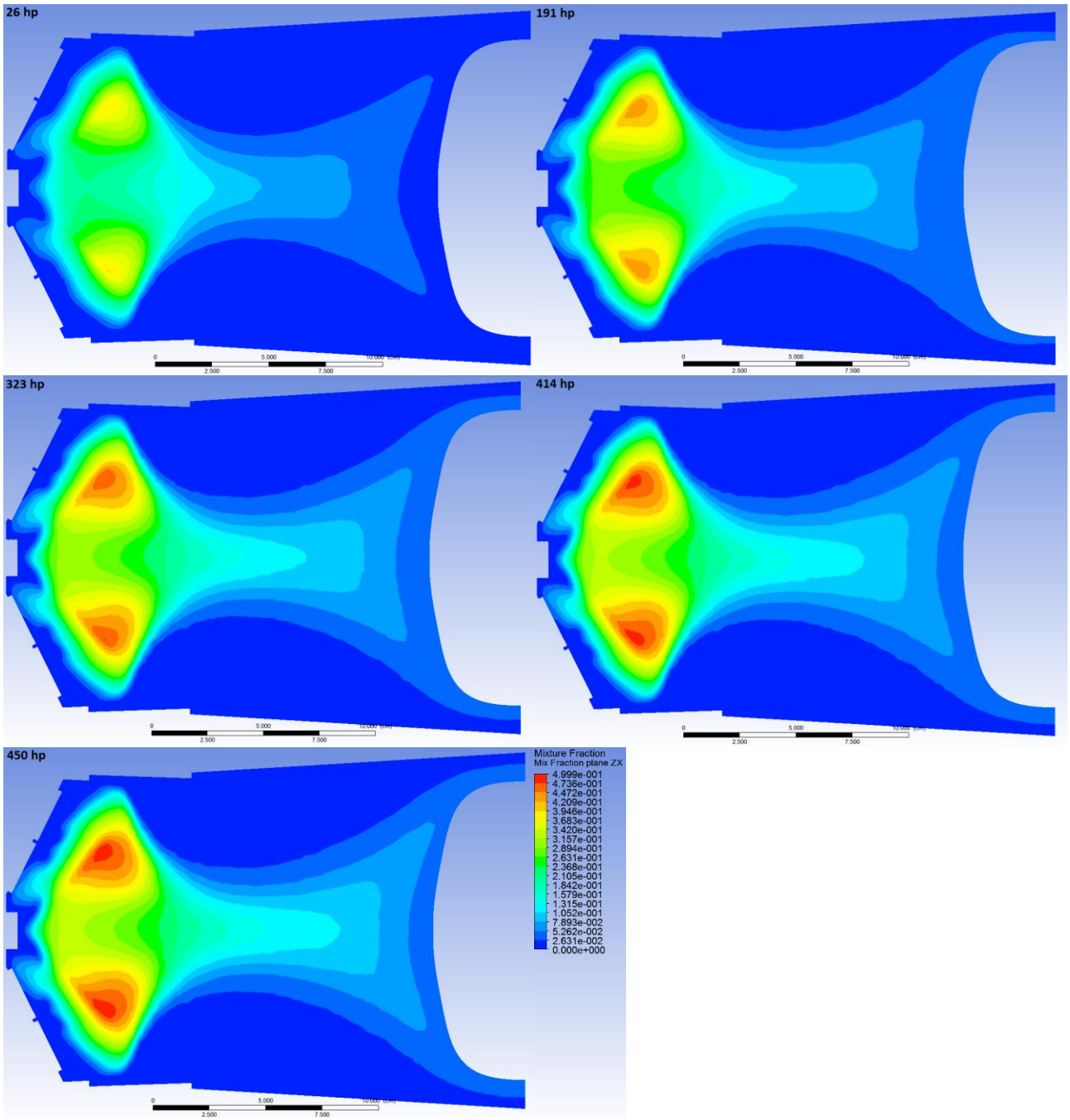

Figure 4.6 *Mixture fraction profiles along the ZX plane*

In the region close to injection there is a higher degree of mixing; lower concentration gradients may be caused by a lower evaporation fuel rate. These considerations bring to a reduction of temperature peaks, especially in the primary region (as noticed previously in Figures 4.1 and 4.2).

The related charts for velocity and mixture fraction, made on the comparison lines, are showed in the following Figures 4.7 and 4.8

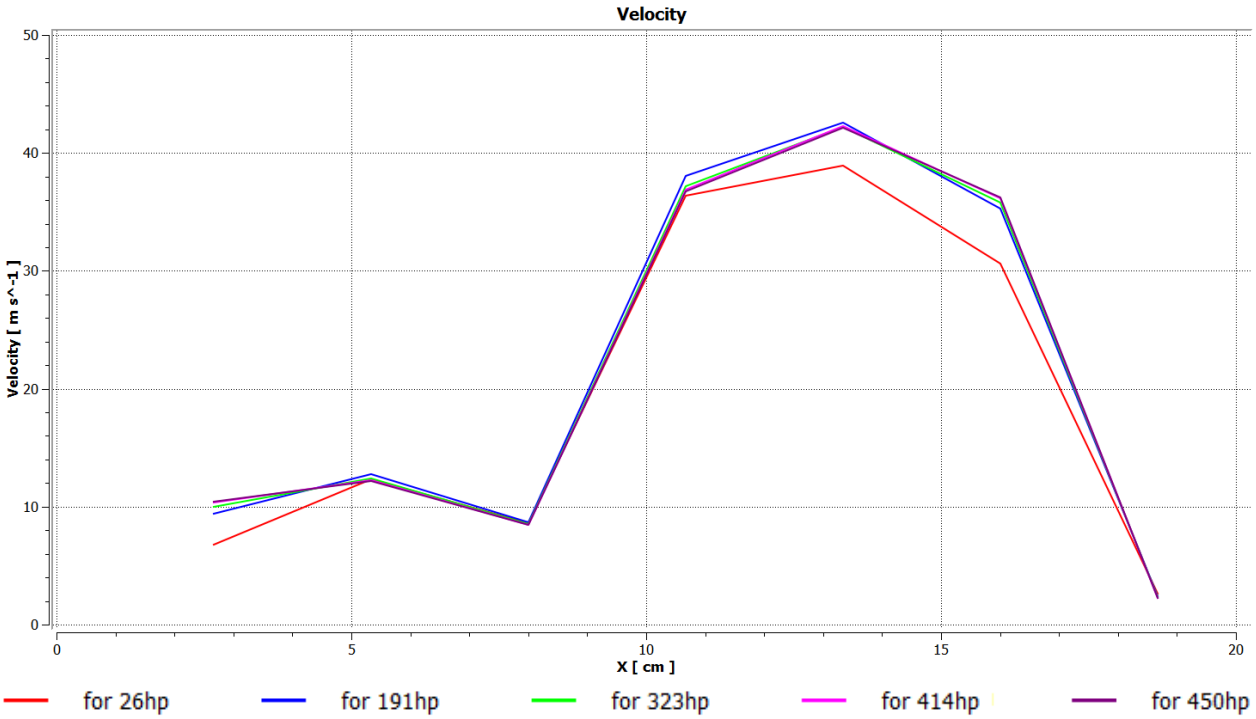

Figure 4.7 *Velocity profiles along the center line*

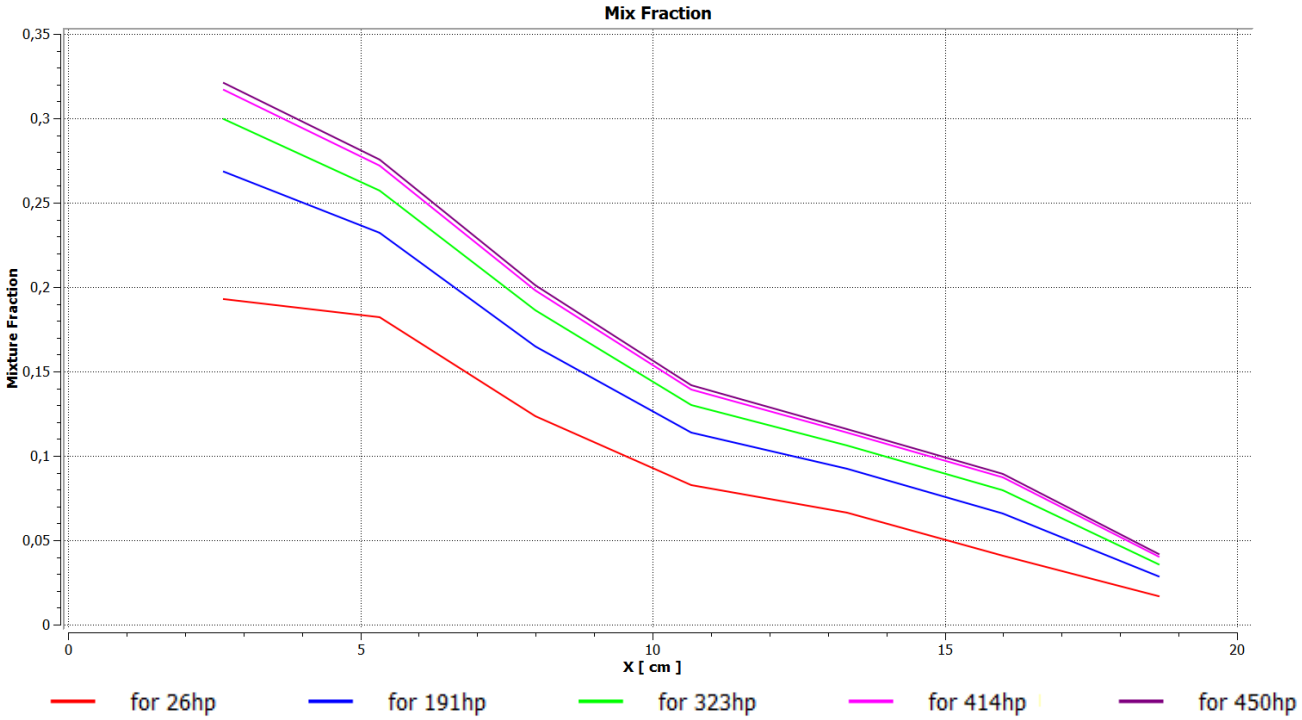

Figure 4.8 *Mixture fraction profiles along the center line*

In Figure 4.9 pressure profiles [Pascal] inside the combustion chamber are reported along the plane ZX. In this case the reference scale is different because we have specific working pressure for each power (see Table 3a-e in Chapter 3, section 3.4). For this results we have used Fluent graphical features.

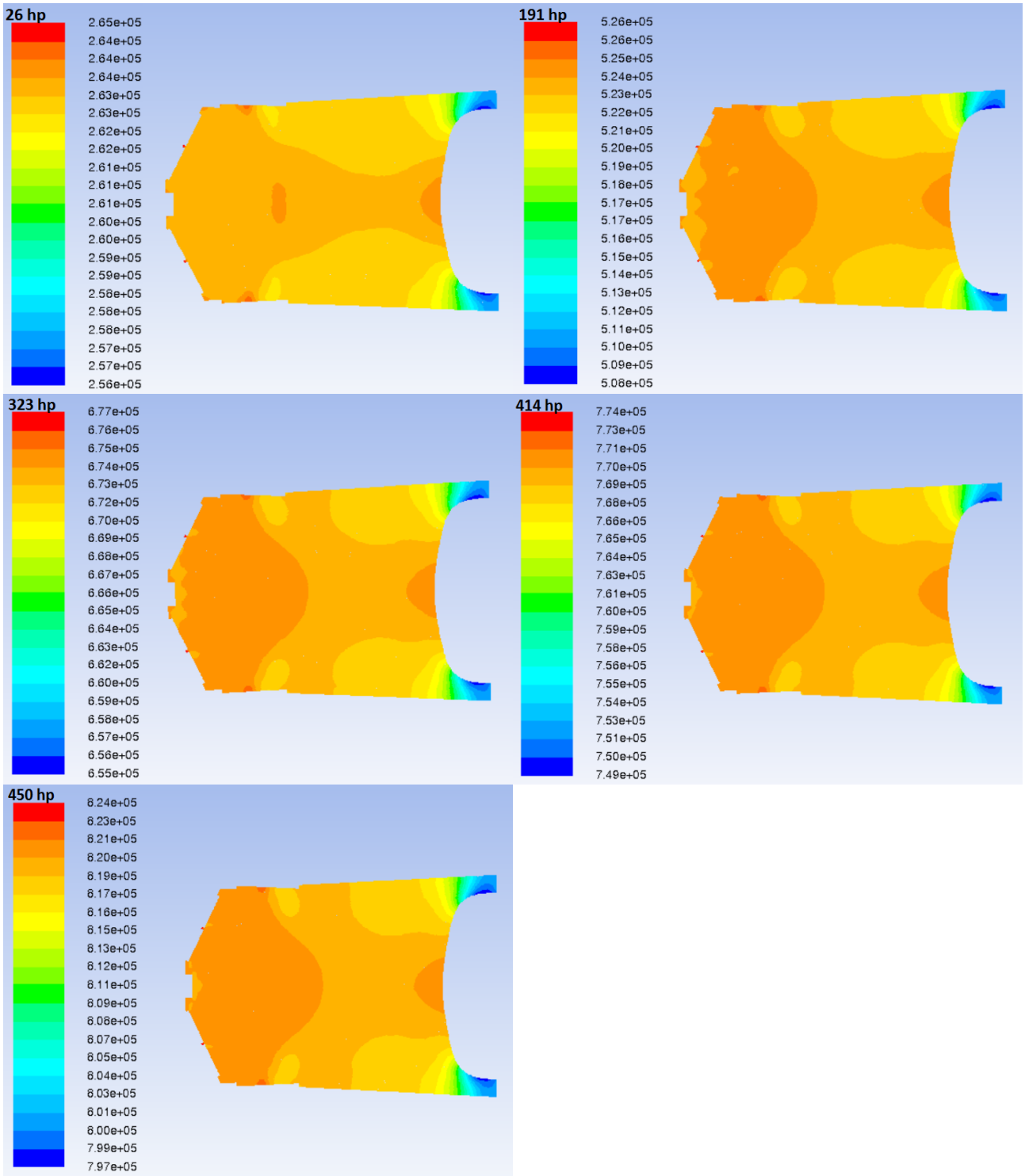

Figure 4.9 *Pressure profile along the plane ZX*

It can be noticed that in the region of spray evaporation the pressure is slightly higher than in the rest of the combustor.

4.2 Basic results

As explained in the Chapter 2, we have based our simulations on the flamelet model. So first, we have had to generate a set of flamelet and a pdf table for each cases. The kinetic mechanism used to create flamelet is the reduced scheme for kerosene surrogates developed by the CreckModelling group [51] at the Politecnico of Milan.

The reduced mechanism includes 123 species but, during the pdf table generation, just the 50 more present species have been tabulated.

In the Figures 4.10 and 4.11 we can see some examples of flamelet 2D graphs and a 3D representation of the pdf.

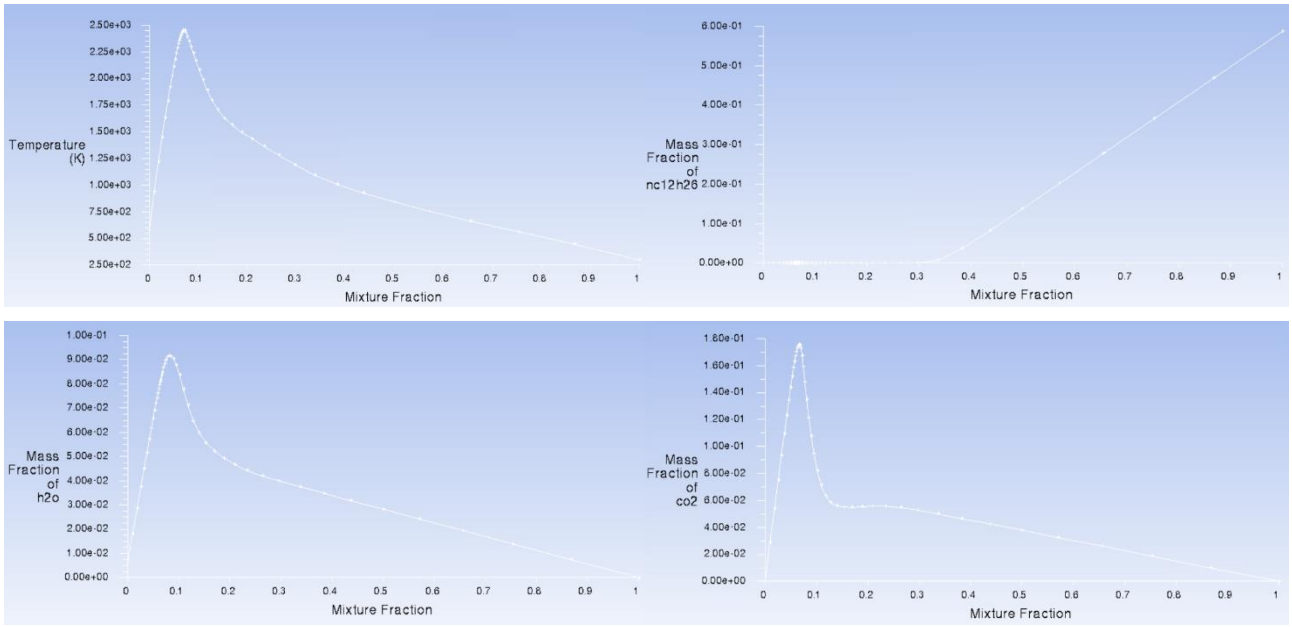

Figure 4.10 *Flamelet graphs*

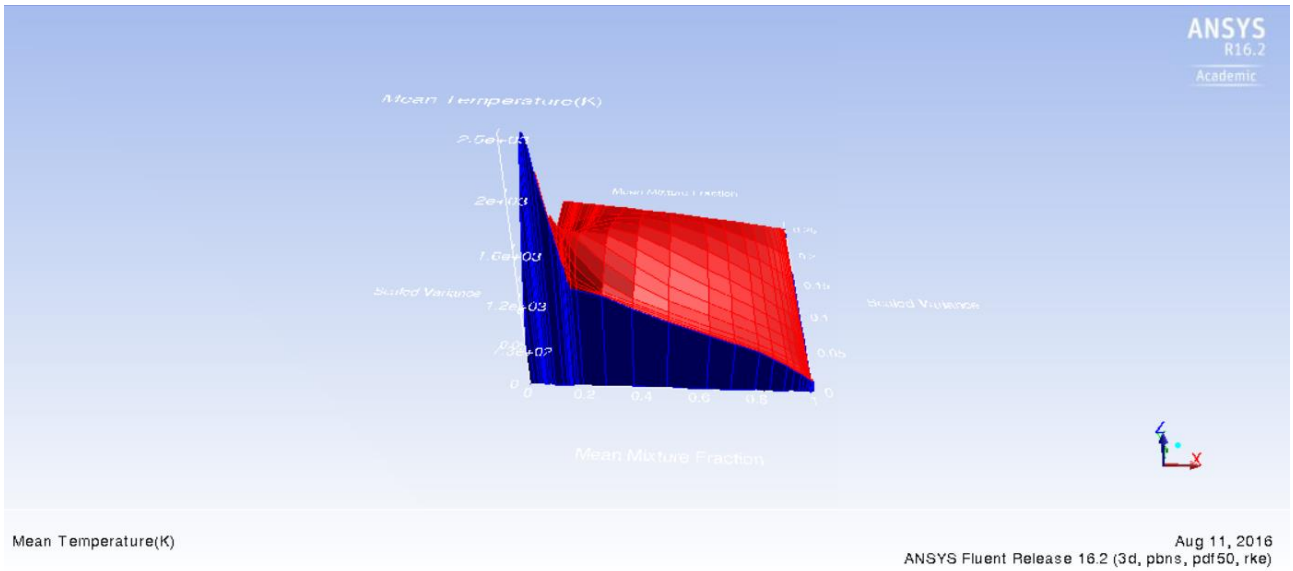

Figure 4.11 3D PDF

4.2.1 Dry air

During first simulations, the air composition didn't take in account the presence of water and hence this have brought to an underestimation of the water content measured at the outlet. In the Figure 4.12 below we can see a graph that shows the water values [mol%] predicted in the Emicopter project [4] (even in that case those values were underestimated), our new values (New) and the experimental data refers to flights 1734-1735-1736 (see Chapter 3).

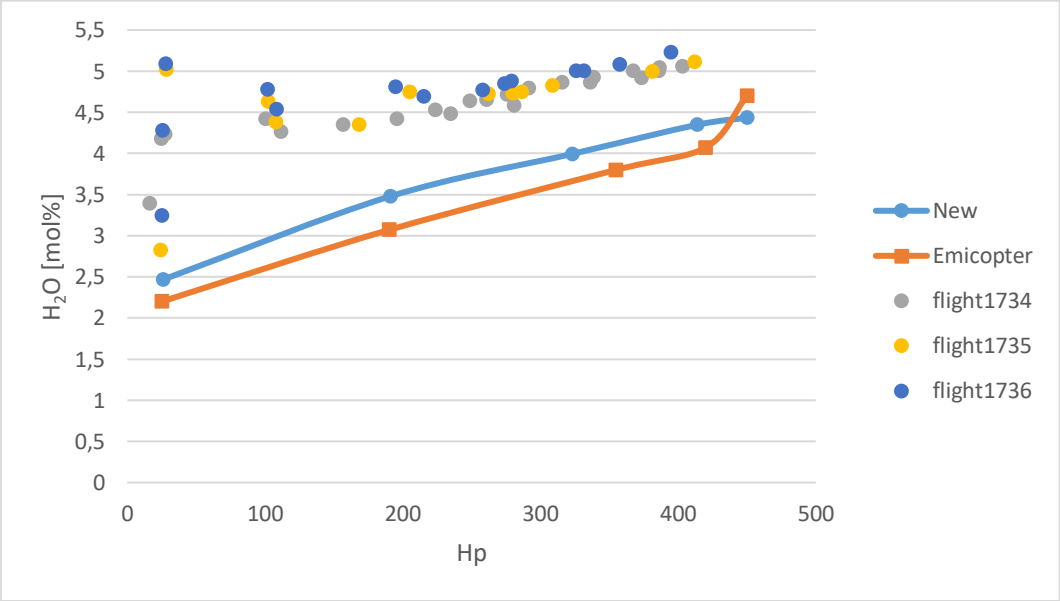

Figure 4.12 H_2O production: predictions vs experimental data

It's easy to notice that that there is an absolute difference of about 1% mol between our predictions and the experimental data. We have supposed that this constant difference might be caused by the fact that we have used dry air. So, we decided to analyze the experimental data to compute the relative humidity of the air. Conclusions and results are summarized in the following section 4.2.2.

4.2.2 Wet air

From the material balance it's possible to calculate the expected water in the air. Subtracting it from measured values we found the excess of water while from the Antoine equation we calculated the water present in the saturated air. The ratio between this two last quantity is the relative humidity of the air.

The value predicted was two; the first one for flights performed under 1000 feet and the second one for flights over 1000 feet. This distinction is due to the fact that in altitude the air humidity is lower. The two values and the calculation done are reported in the Table 10 and 11 with the composition in molar fraction percentage.

		[%] tot	tot molar fract	molar fract	[%] mol
molar composition wet air under 1000 feet	N_2	78,08	0,7808	0,77337	77,34
	O_2	20,95	0,2095	0,20751	20,75
	Ar	0,934	0,00934	0,00925	0,925
	H_20	0,997	0,00997	0,00987	0,985
		…			
	sum	100,96	1,0096	1	
	average humidity [%]	0,997			

Table 10 *Molar composition [mol%] wet air under 1000 feet*

		[%] tot	tot molar fract	molar fract	[%] mol
molar composition wet air over 1000 feet	N_2	78,08	0,7808	0,77587	77,59
	O_2	20,95	0,2095	0,20818	20,82
	Ar	0,934	0,00934	0,00928	0,928
	H_20	0,672	0,00672	0,00667	0,662
		…			
	sum	100,64	1,0064	1	
	average humidity [%]	0,672			

Table 11 *Molar composition [mol%] wet air over 1000 feet*

New simulations have been performed and the results (under 1000 feet) are reported in the charts below (Figure 4.13a-d).

In this specific section, as seen in Chapter 3 section 3.4, the experimental data (flights 1734-1735-1736) collected over 1000 feet are omitted. The data over will be considered in the following section 4.2.3 where we model two specific cases that refer to a height of 8000 feet.

As seen before (section 4.2.1), a comparison with the Emicopter project [4] has been planned to better understand improvements of this New model.

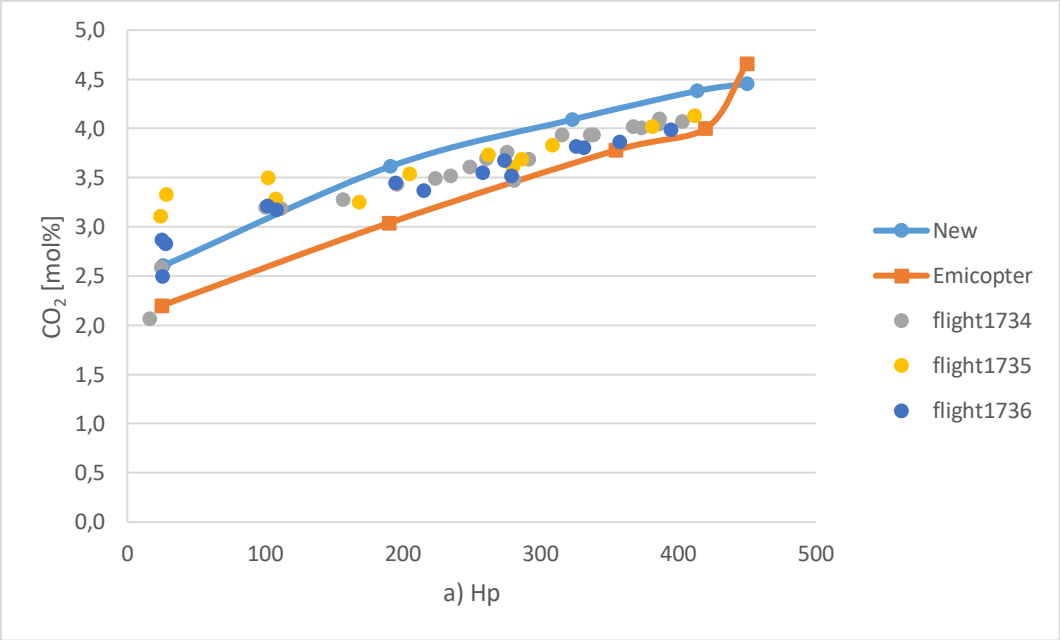

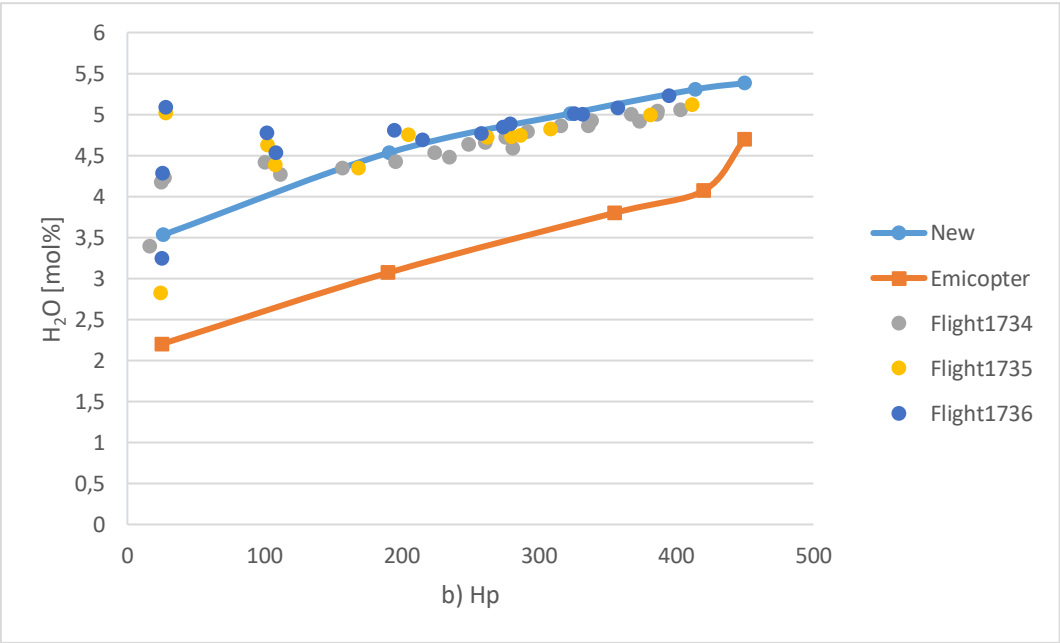

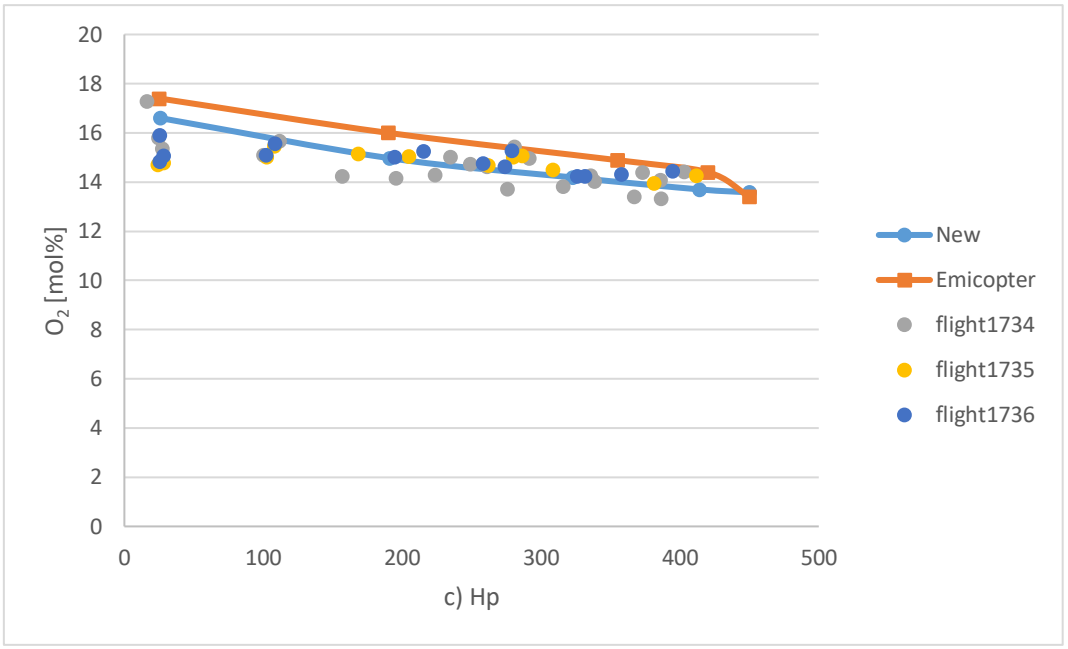

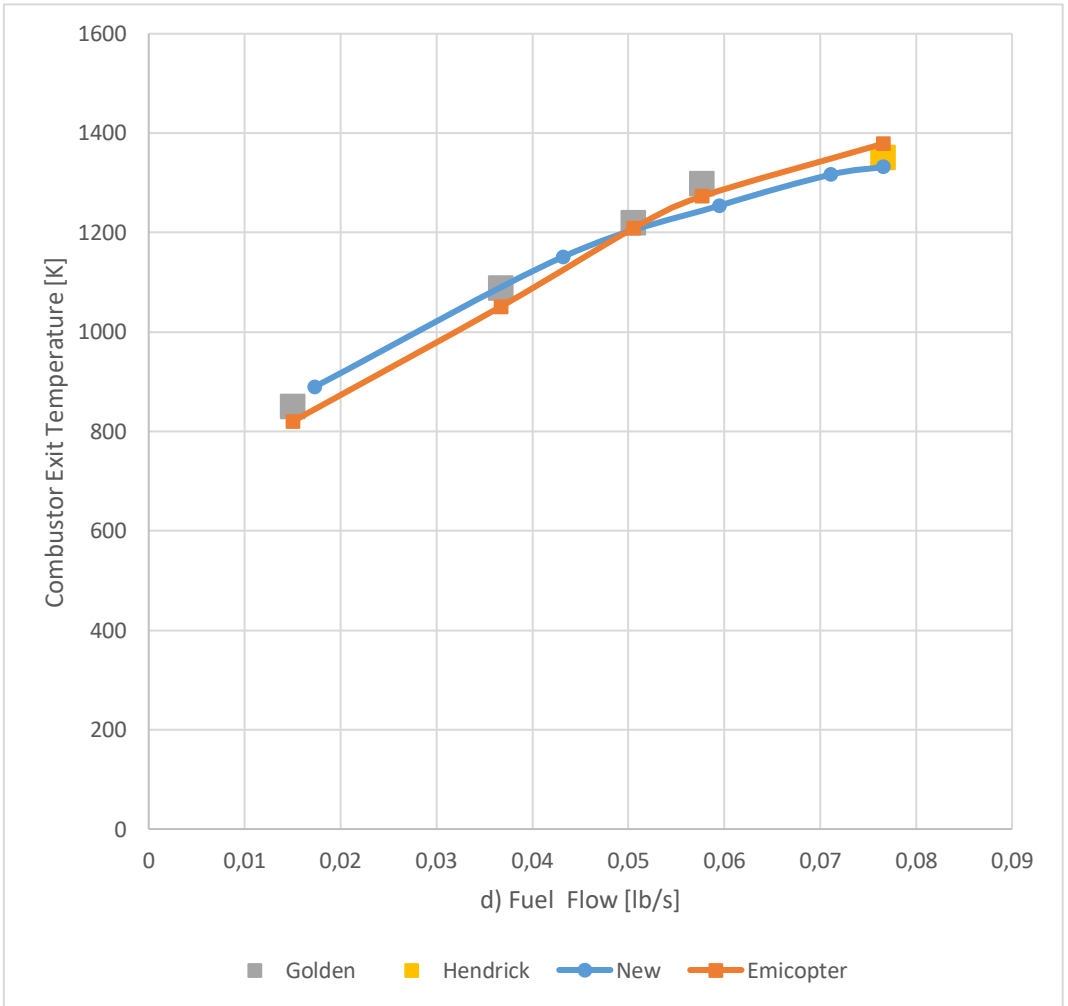

Figure 4.13a-d *Experimental data compared with the Emicopter project [4] results and the new ones. a) CO_2 [mol%] b) H_2O [mol%] c) O_2 [mol%] d) combustor exit temperature [K] (in this last case we have not experimental data but just the ones taken from literature [13] [14])*

The results are in a quite good agreement with the experimental data. The bigger difference can be observed at low power conditions where our model underestimates the CO_2 and H_2O molar composition and, in a less significant way, overestimates the O_2. The molar fraction of CO_2 seems to be globally slightly overestimated even if the right trend in maintained. The temperature profile is also a little bit different, especially for high powers, but in this case the experimental data comes from the literature and, except for the 450 hp case, are based on a different type of engine (C20B).

The improvement of the New model is mainly associated to a better characterization of the boundary conditions, which have been only estimated using different literature sources in the case of the Emicopter project [4]. We can support this affirmation just observing the different values predicted at 450 hp, which is the only case related to the two projects using the same engine (C20R).

Figure 4.14 shows that, except for the water content, there is no much different from the simulations done with dry air or wet air, as you can notice in the resuming Figure 4.14 below.

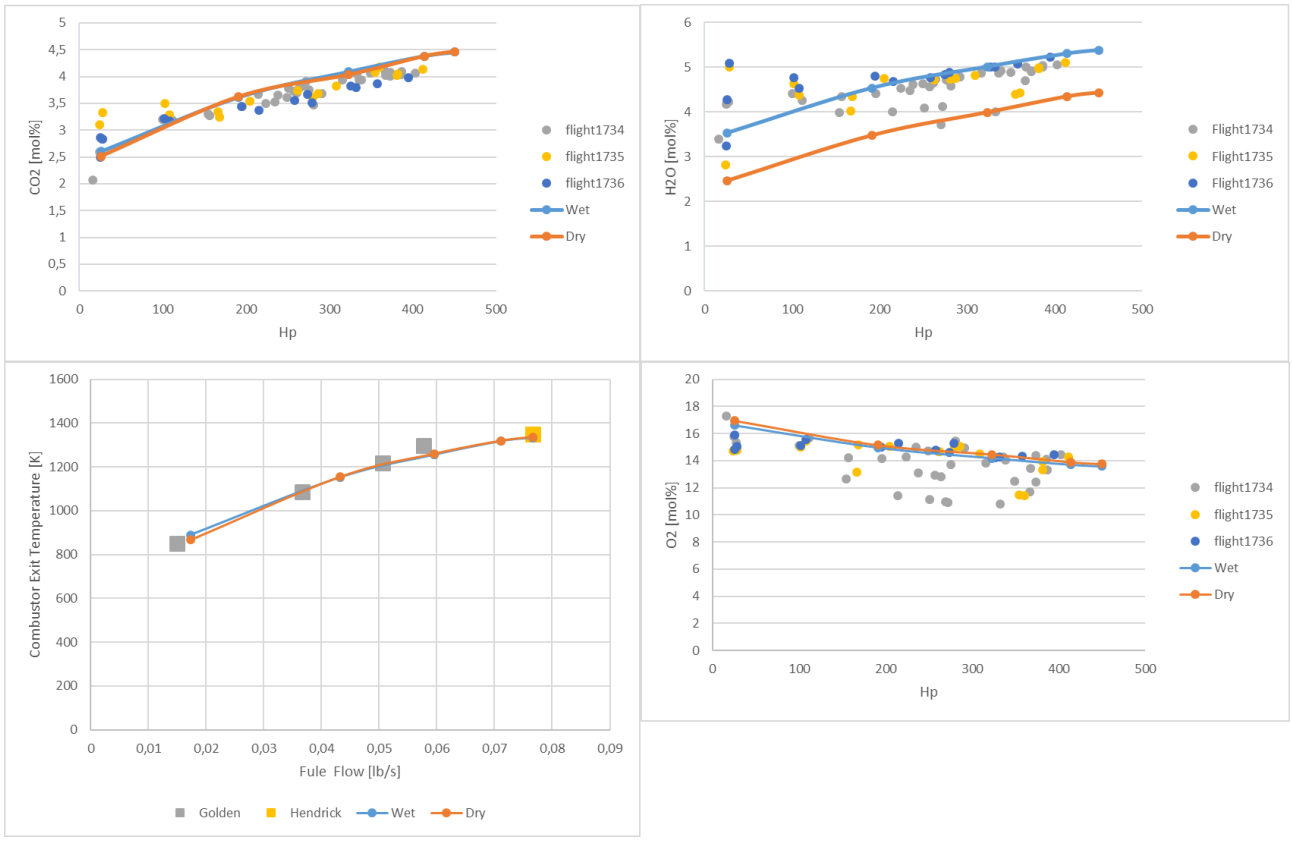

Figure 4.14 *Dry air Vs. Wet air*

A view of mass fractions profiles of CO_2, H_2O and O_2 along the ZX plane for all the powers (from 26 hp to 450 hp) is also reported below (Figures 4.15, 4.16 and 4.17).

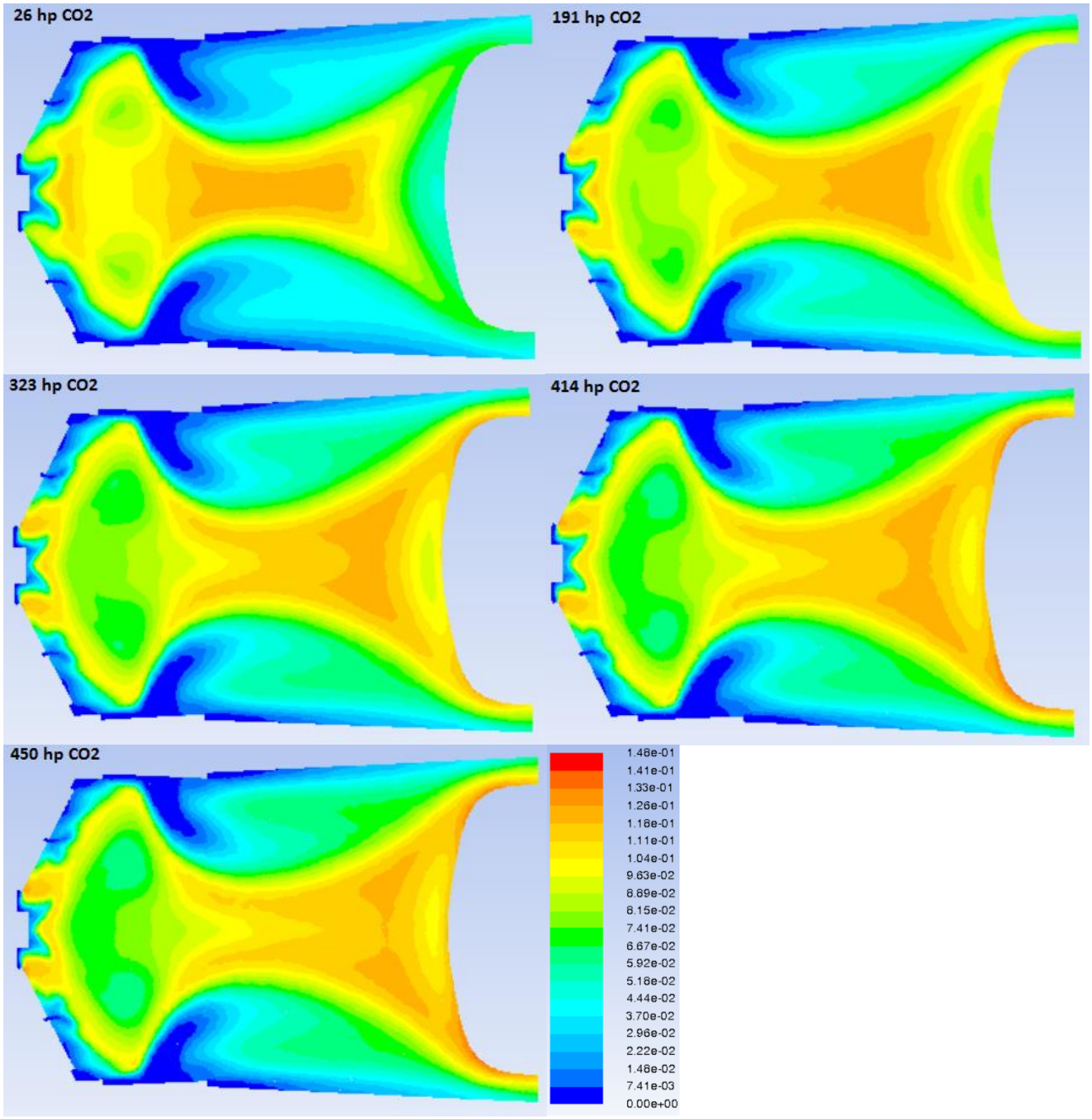

Figure 4.15 *Mass fraction profile of CO_2 along the ZX plane*

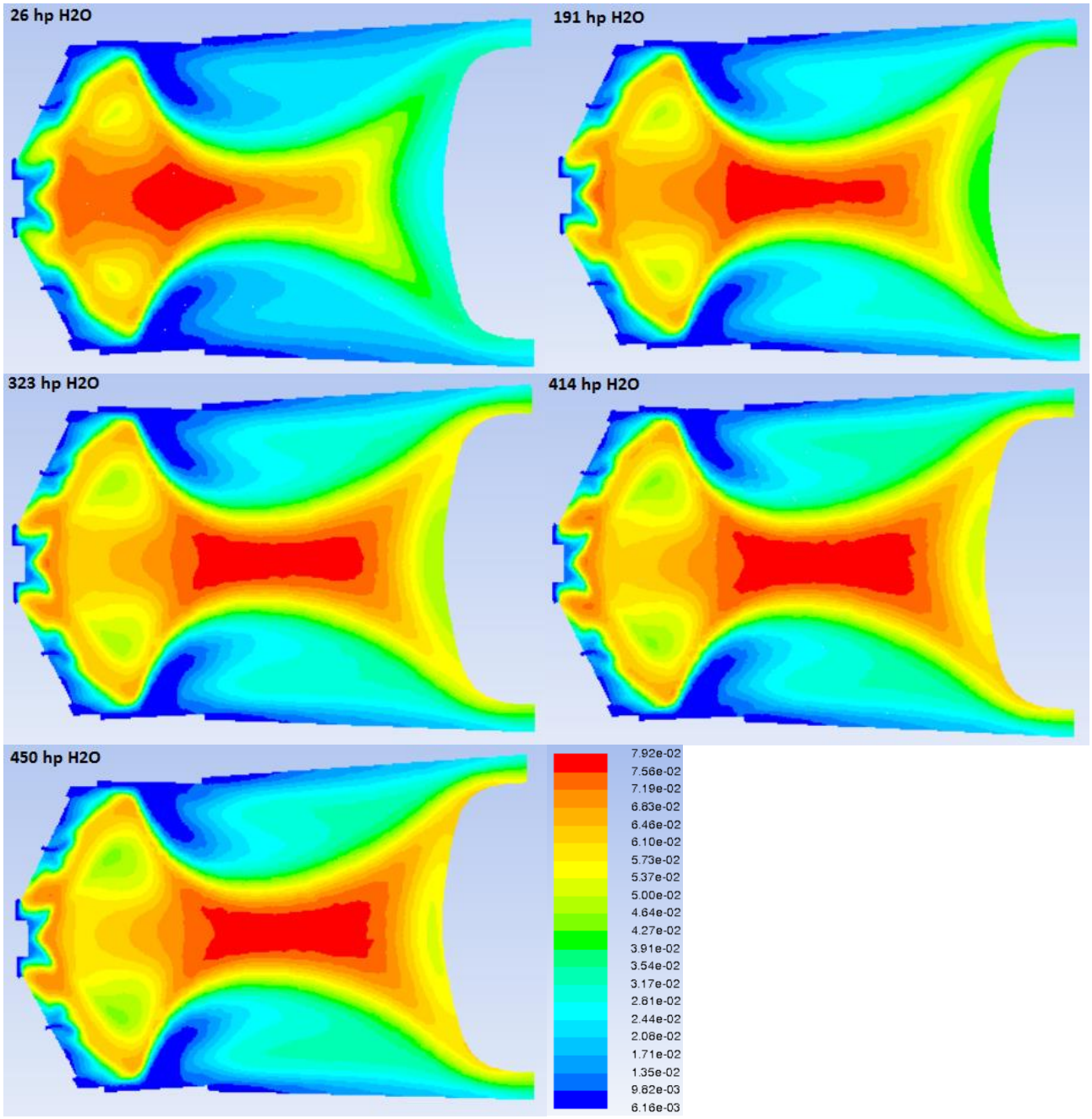

Figure 4.16 *Mass fraction profile of H_2O along the ZX plane*

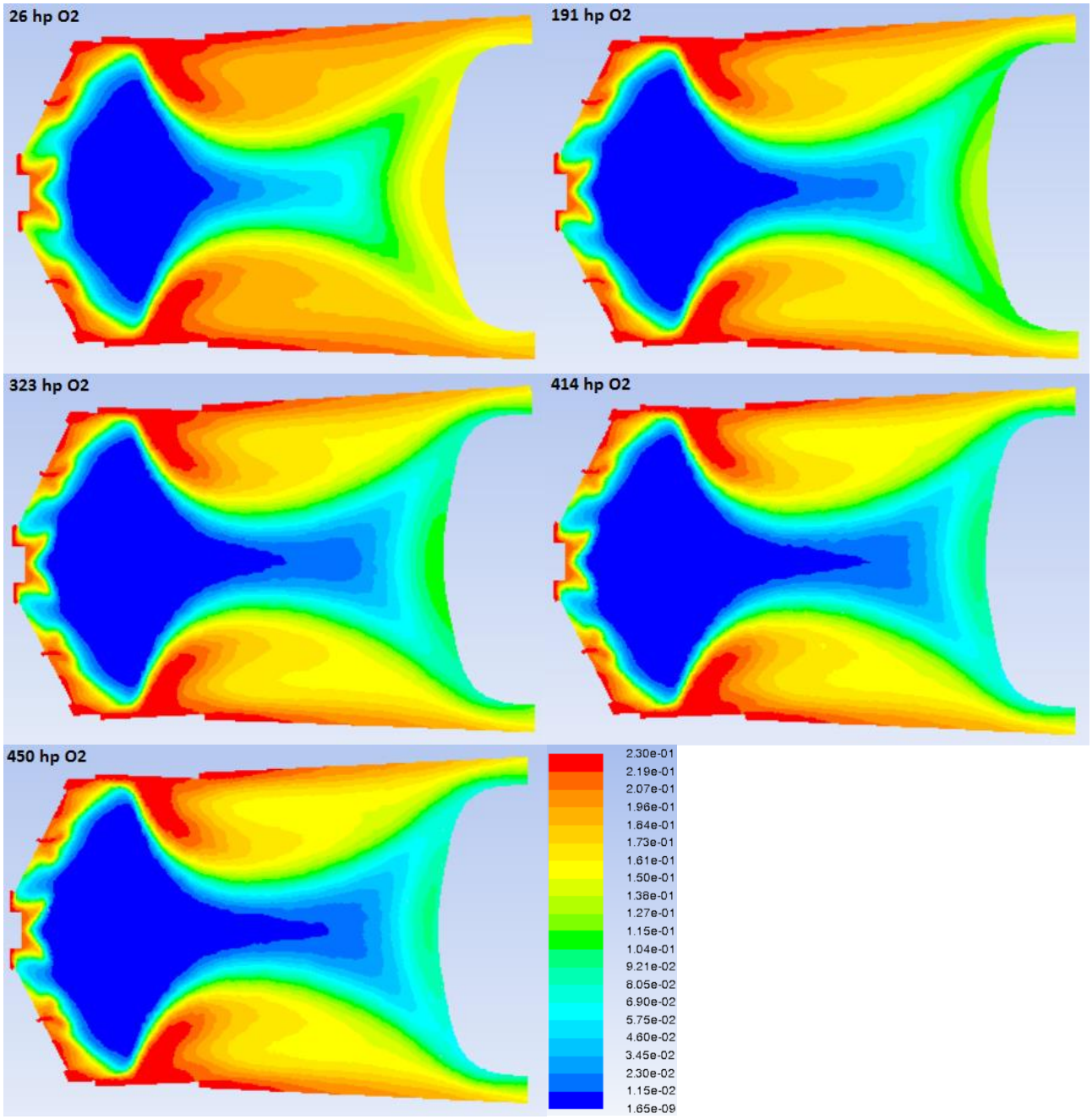

Figure 4.17 *Mass fraction profile of O_2 along the ZX plane*

Combustion of hydrocarbons at high temperature occurs via hydrogen abstraction followed by rapid decomposition to smaller fuel fragments which undergo oxidation reactions. There are a great variety of these processes that produce fuel radicals and oxidizing radicals. For a reference power (450 hp), we want to show the mass fraction profiles along the ZX plane of some radicals and important species involved in the combustion inside this engine (Figure 4.18a-f).

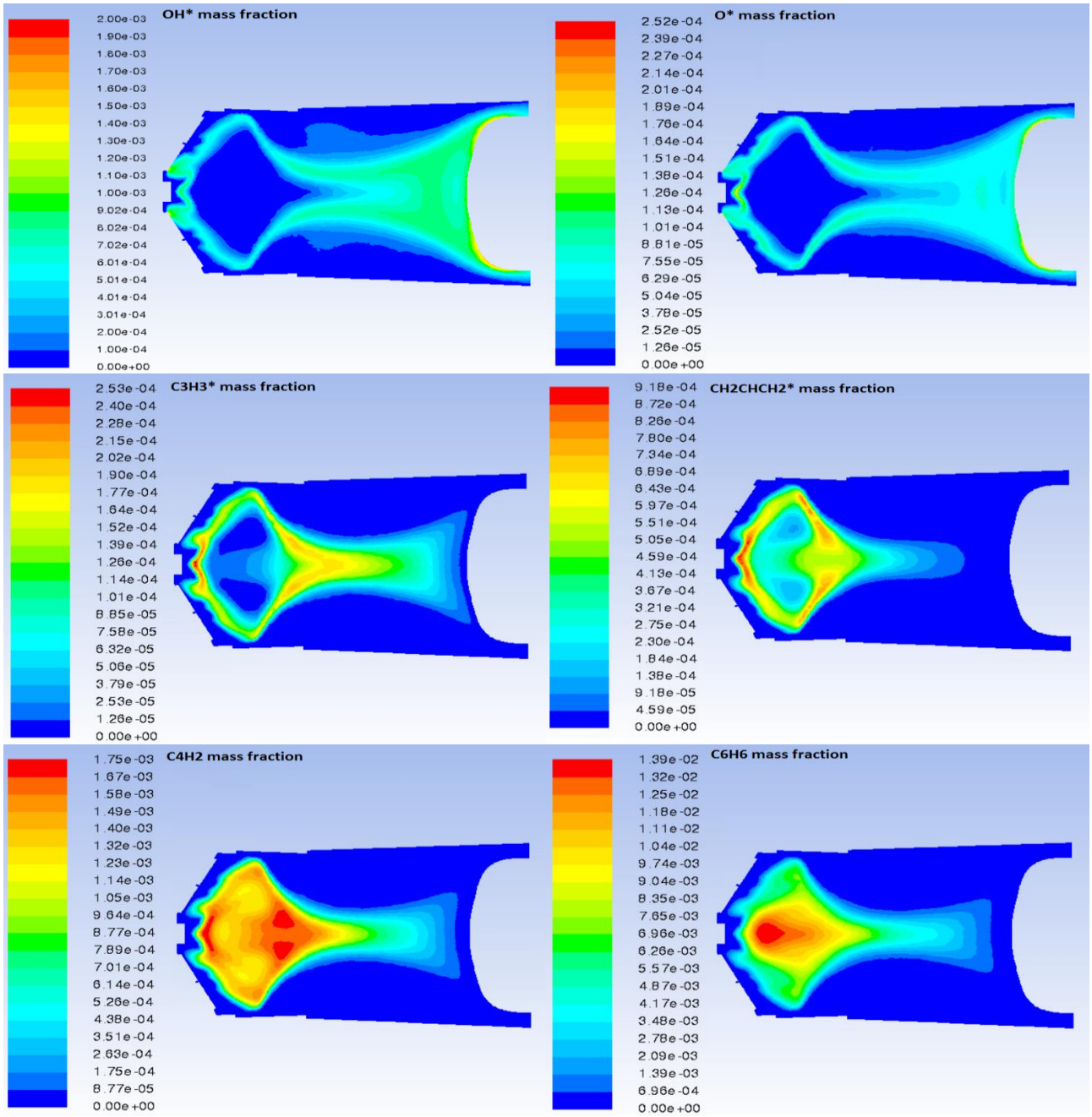

Figure 4.18a-f *Mass fraction profiles along the ZX plane of some radicals and important species involved in our combustion a) OH* b) O* c) CH_3CH_3* d) CH_2CHCH_2* e) C_4H_2 f) C_6H_6*

We can notice how some species like OH* and O* are mainly present near the flame front (this characteristic is common for all the radicals in general) while others, like C_6H_6 and C_4H_2, are largely present in the rich zones.

4.2.3 Over 1000 feet flights

As we said in the previous chapter, we analyzed also two "special" cases. What differentiates them from the others is that the experimental data have been collected during flights over 1000 feet. In the Figures they are marked as red points.

To better underline the difference between these cases and the others, we adopted boundary conditions of flights done at 8000 feet.

We can notice that they have boundary conditions (Chapter 3, section 3.4) and, obviously, results (see the following Figures) quite different from the base cases. In the charts below, the experimental data were cleaned from the ones taken under 1000 feet to have better view on the results.

In Figure 4.19a-c we have compared our model with the data collected. We have no data for power lower than 100 hp simply because under this threshold the helicopter cannot fly. The mission 1736 doesn't provide flight altitudes above 1000 feet.

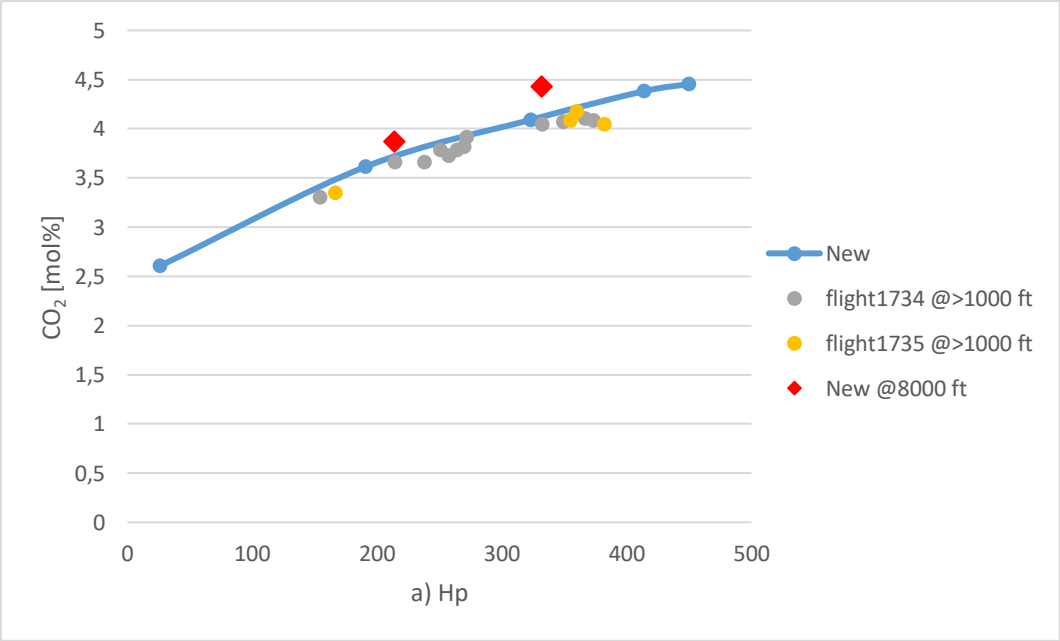

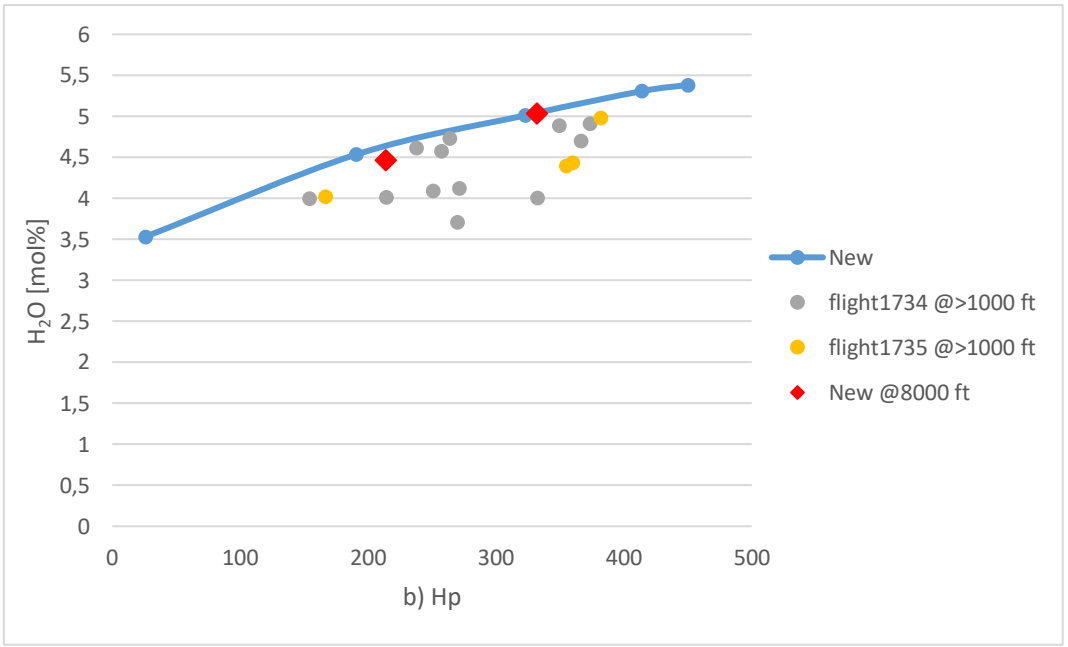

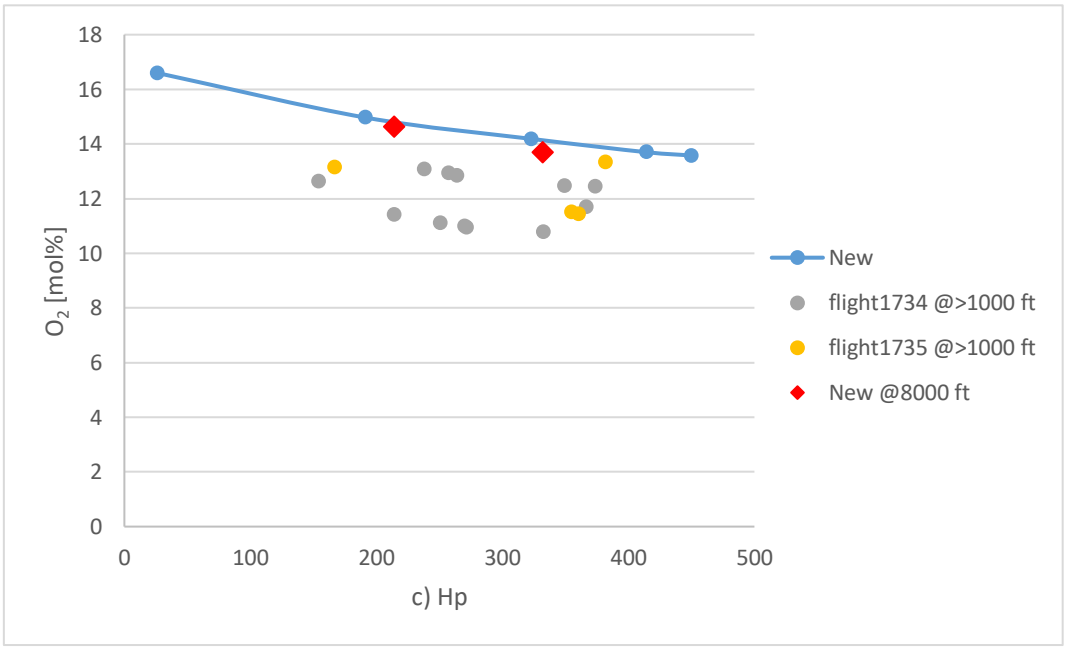

Figure 4.19a-c *Experimental data compared with the model results above 1000 feet. a) CO_2 [mol%] b) H_2O [mol%] c) O_2 [mol%]*

The results are in good agreement with the data even though, as seen in standard cases, they are a little overestimated. Obviously, we don't need to underline that results obtained from computer simulation, even in the case of complete combustion products like CO_2 and H_2O, cannot perfectly reproduce the experimental data due to uncertainties in measurement and/or in the boundary conditions.

There are a lot of parameters that influence the data collection during the experimental campaign; for example, simply the weather condition can interfere significantly.

4.3 Pollutant prediction

When satisfied that the model can represent in a good way real engine emissions (CO_2, H_2O and O_2), we start using the Post-Processor and tools (as the Unsteady flamelet) implemented in Fluent to estimate some of the pollutants produced.

4.3.1 NO

First, we calculated the NO emission. We considered both thermal and prompt mechanism with the N_2O formation and reburn method. For the turbulent interaction mode, we chose the mixture fraction option.

As we can see in the Figure 4.20 below, the results modeled almost perfectly the experimental data except for low powers for which the data are likely to not be suitable. An improvement is also clear respect the Emicopter project [4] due to the new boundary conditions and the geometry refinement.

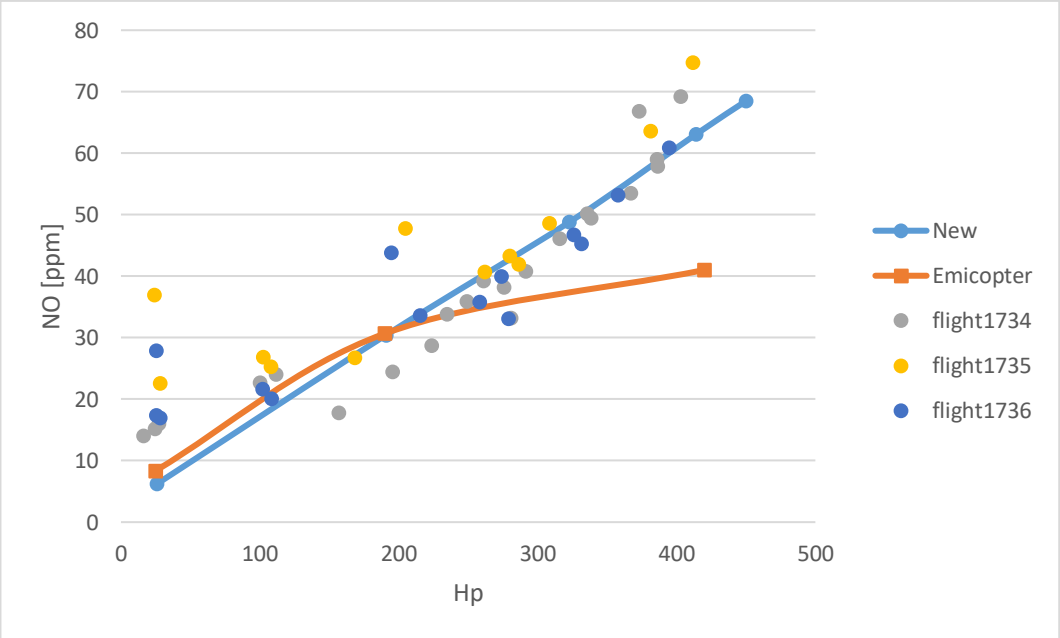

Figure 4.20 *NO production [ppm]: predictions vs experimental data*

According to Tsutomu Shimizu [54], other species present at the same concentration as NO therefore do not affect the reading. Species present in much larger concentrations may, however, interfere with the NO readings. At low power, we have a great production of CO and unburned hydrocarbons that can easily lead to wrong NO measures.

In Figure 4.21 we compared also data and results got over 1000 feet. The results still remain in good agreement with the experimental data.

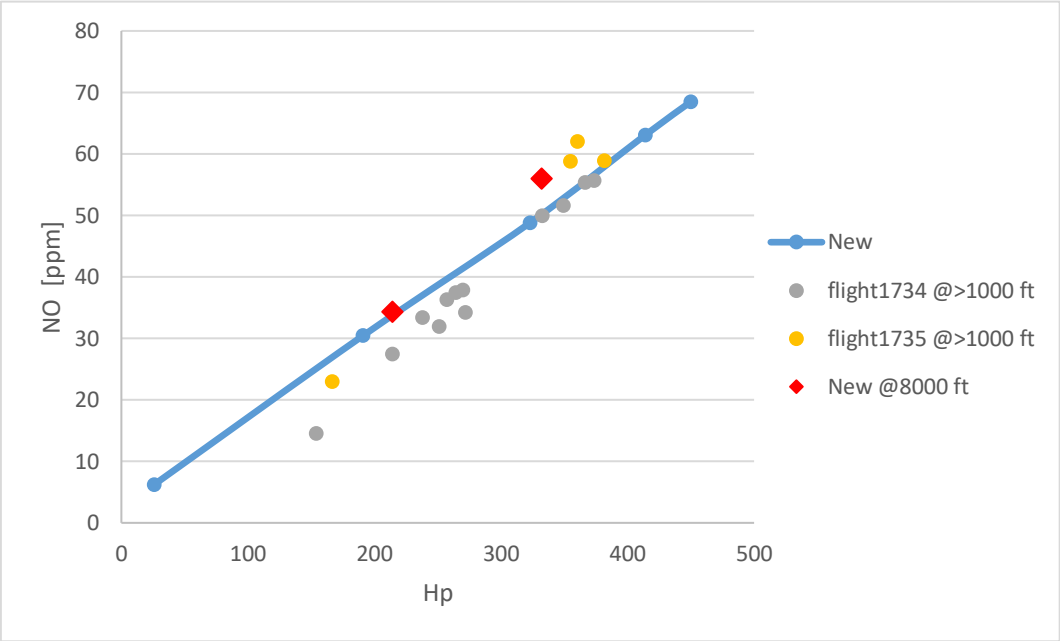

Figure 4.21 *NO production [ppm] above 1000 feet: predictions vs experimental data*

4.3.2 N_2O

It's very important to quantify the N_2O production because is a greenhouse gas 300 times worse than CO_2 as well as an ozone destroyer.

Unfortunately, as we can see in Figure 4.22 the model isn't so accurate for N_2O emission. The mission 1734 doesn't provide any information about the N_2O ppm production.

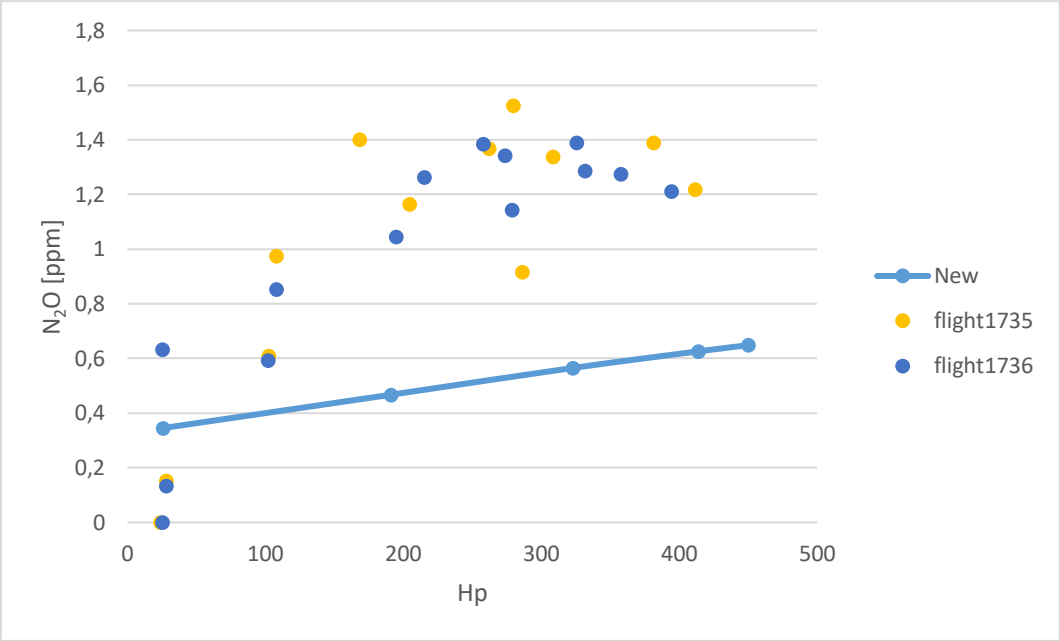

Figure 4.22 *N_2O production [ppm]: predictions vs experimental data*

Nevertheless, the trend of the model isn't completely wrong and further improvement of model calculation parameters could improve the accuracy.

4.3.3 CO

We wanted to compute the CO emission and we have tried different methods to do that; unfortunately, none of these have worked properly.

First, we have analyzed the CO emission predicted by Steady diffusion flamelet but with this method the results cannot be right due to the inability to predict compounds characterized by slow chemistry, as previously explained in Chapter 2, section 2.6.1.

So, we have tried a second method, the Unsteady diffusion flamelet, that can be used to predict slow-forming intermediate and product species that are not in chemical equilibrium. Nevertheless, even in this case, the results are not satisfactory.

We have tried a third method as well, reactor network model available in Ansys Fluent; this model agglomerates cells from the CFD solution into a user-specified small number of reactors and computes detailed chemistry on this reactor network. Unfortunately, the computational time has been enormous and we have not even managed to get the results.

In the following Figures 4.23 and 4.24 we report the produced results. We are not able to correctly estimate nor the numerical values nor the trend, both for ppm and g/s measurements. In Chapter 5 we will use a Post-Processor, developed by CreckModelling group [53], trying to better predict the CO formation.

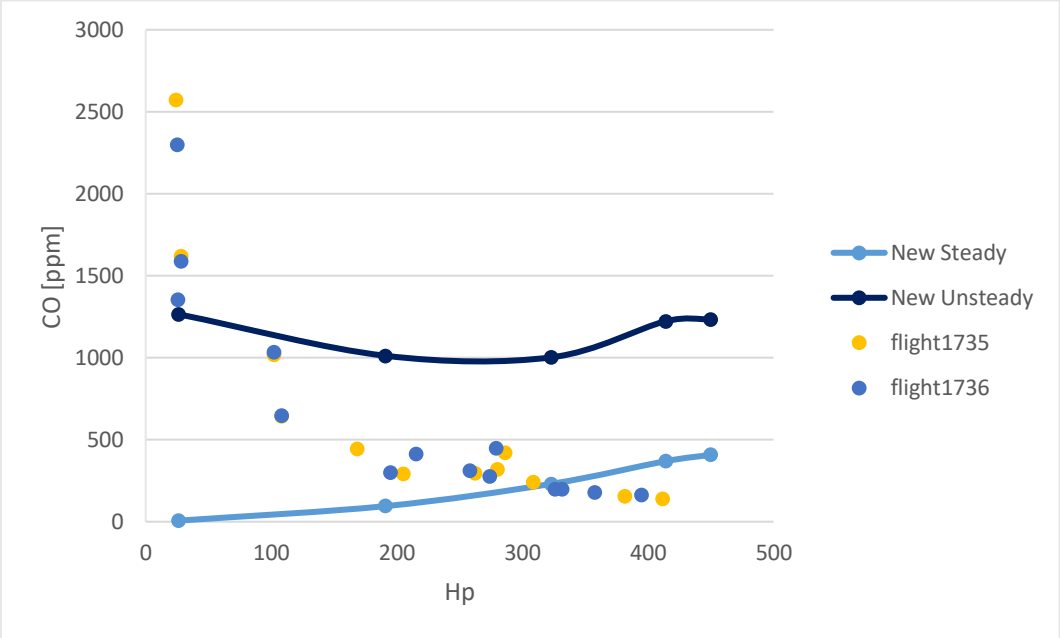

Figure 4.23 *CO production [ppm]: predictions (both steady and unsteady model) vs experimental data*

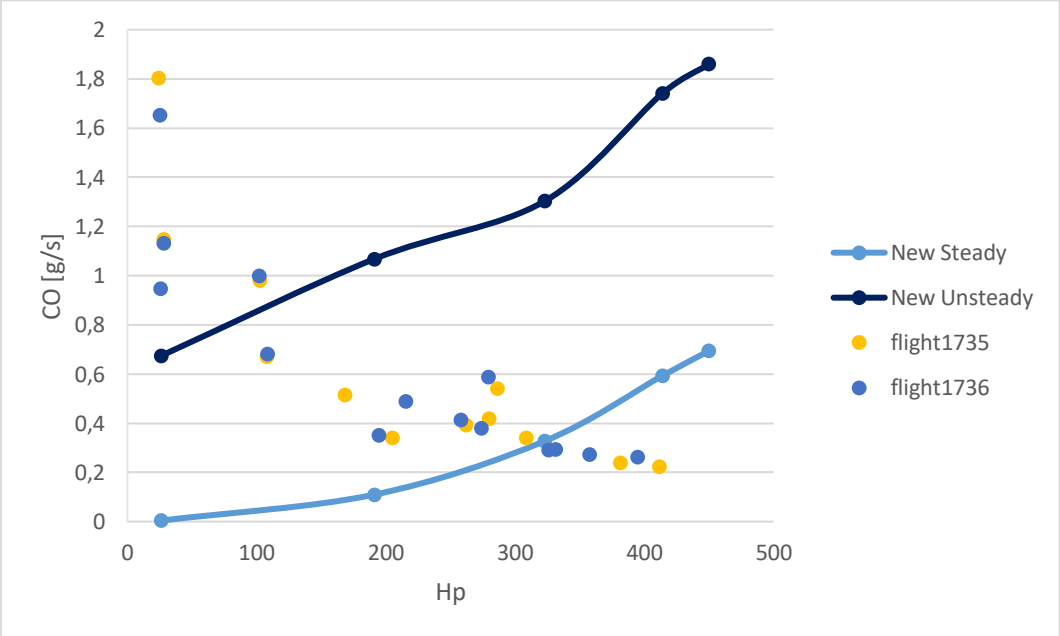

Figure 4.24 *CO production [g/s]: predictions (both steady and unsteady model) vs experimental data*

4.3.4 Unburned hydrocarbons

As the CO prediction seen before, the unburned hydrocarbons are slow chemistry species and so the results obtained are completely wrong. They are shown in the Figures 4.25, 4.26 and 4.27 below. The steady and unsteady cases are virtually overlapped. Both cases are not able to predict value significantly different from a zero value.

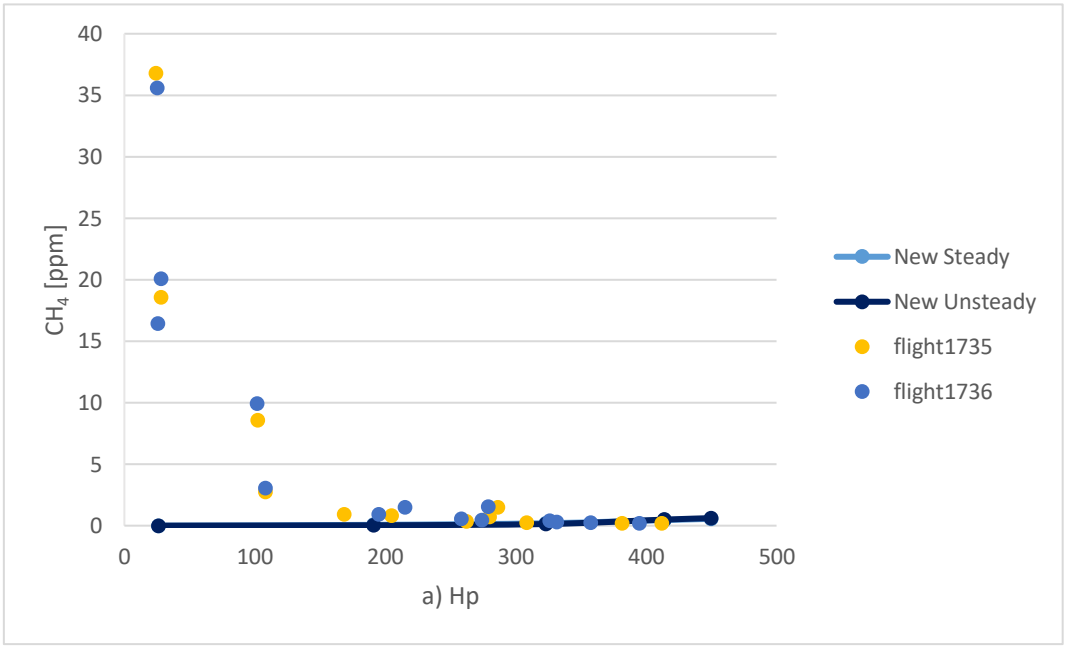

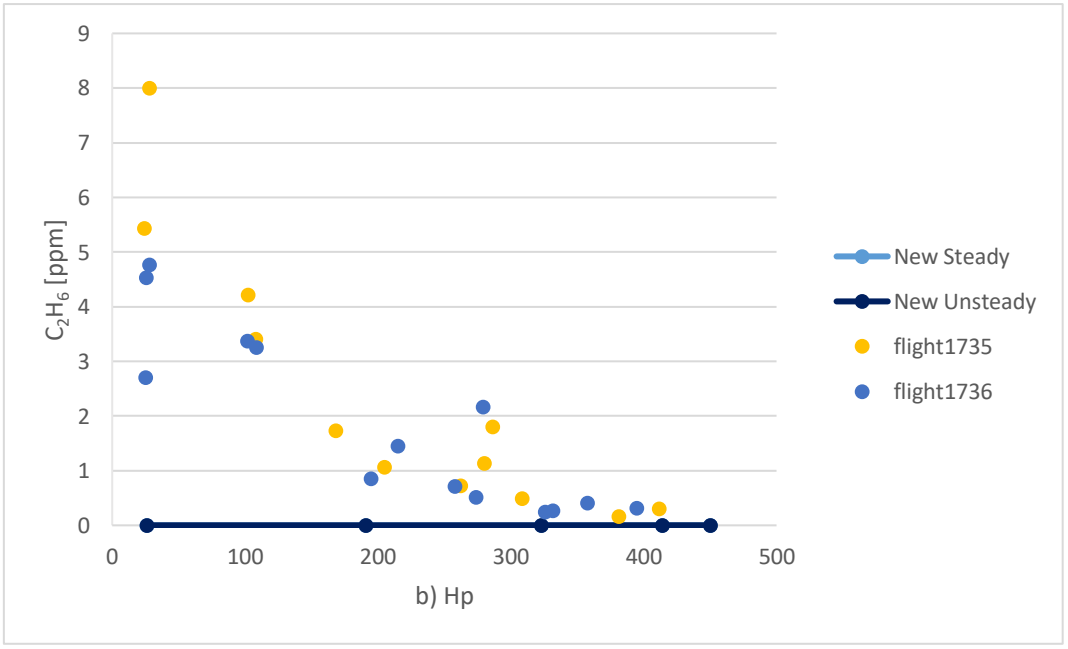

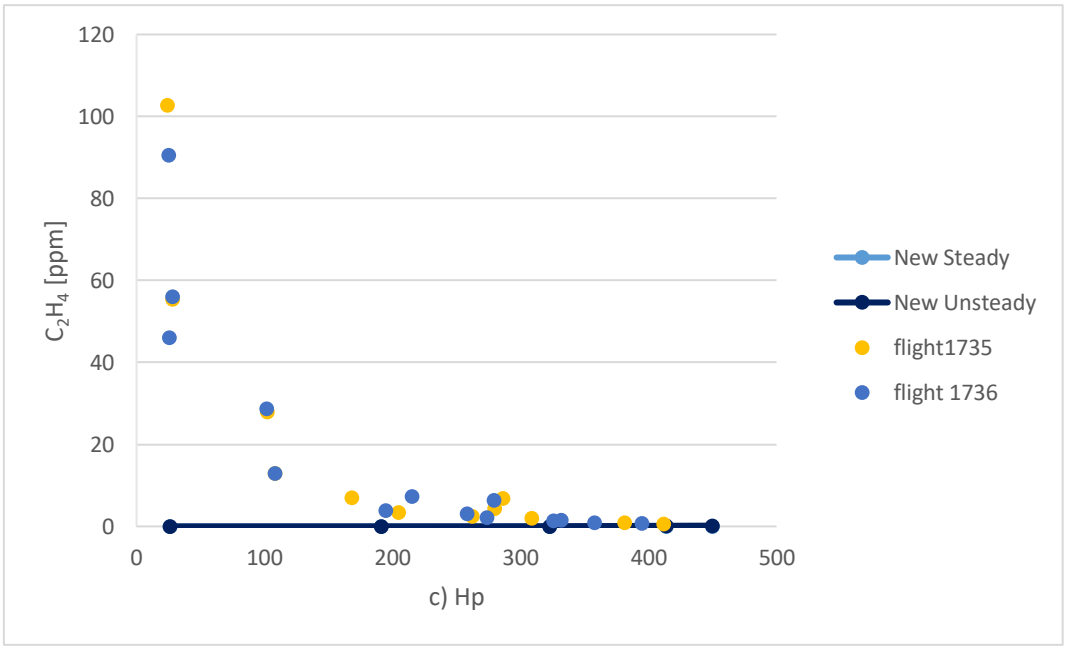

Figure 4.25a-c *Unburned Hydrocarbons production [ppm]: predictions (both steady and unsteady model) vs experimental data a) CH_4 b) C_2H_6 c) C_2H_4*

Chapter 5 – KPP Post-Processor

CFD simulations are not limited to the prediction of fluid flow and thermal field. To further benefit from the prediction, it is useful to adopt post-processing that gives users complete insight into their fluid dynamics simulation results, as seen in Chapter 4, section 4.3. However, the Post-Processor implemented in Fluent haven't reached good values in the field of CO and unburned hydrocarbons predictions. Trying to obtain better results, we have used the Kinetic Post-Processor (KPP) developed at the Politecnico of Milan [53].

5.1 Basic knowledge

The basic idea is to develop a methodology to apply directly detailed kinetic schemes to the study of reactive turbulent systems, restricting the computational effort compared to kinetic and detailed fluid dynamics studies. A complex kinetic scheme can include several chemical species involved in thousands of reactions, which cover a wide spectrum of characteristic time scales, much wider of the characteristic times of turbulence. The temperature and motion fields, calculated using CFD code, is reworked by acquiring the data necessary to build a network of EDC mixing reactors type [55] (with partialization of the reacting volume), interconnected together by exchange of convective and diffusion streams.

At the highest detail level, each cell is then described by a reactor that is at the temperature calculated by the fluid dynamic code (Figure 5.1).

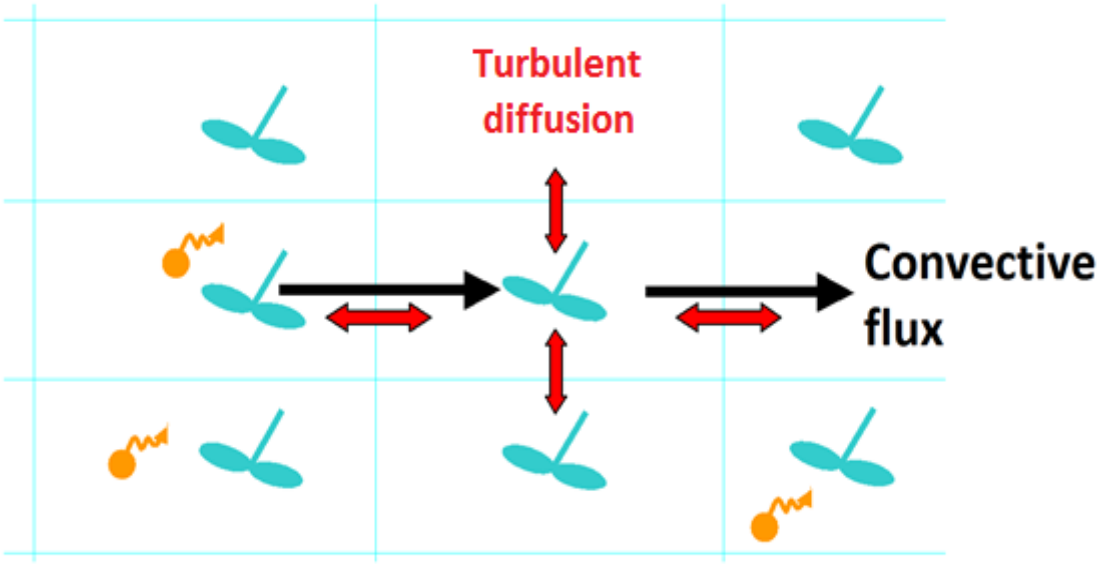

Figure 5.1 *Structure of the kinetic Post-Processor*

The reacting volume is defined as:

$$\frac{V_{rect}}{V_{cell}} = 2.13\left(\frac{\upsilon\varepsilon}{k^2}\right)^{3/4} \tag{5.1}$$

While the governing equation is:

$$\frac{\partial}{\partial t}(\rho Y_i) + \nabla(\rho\vec{v}Y_i) = -\nabla\vec{J_i} + R_i + S_i \tag{5.2}$$

Where $\nabla(\rho v Y_i)$ is the convective flux, $-\nabla J_i$ is the diffusive transport, R_i is the reaction rate and S_i is the liquid evaporation rate.

The convective transport depends on the local value of the motion field provided by the CFD code, while turbulent diffusive transport, which depends not only by the turbulent viscosity but also by the composition gradients, is evaluated for each iteration:

$$\vec{J_i} = -\frac{\mu_t}{Sc_t}\nabla Y_i \tag{5.3}$$

Each reactor is solved by coupling the material exchange and the reactive rate, that is calculated using a detailed kinetic model. The Post-Processor also takes into account the effect of temperature fluctuations on the chemical kinetics (Figure 5.2).

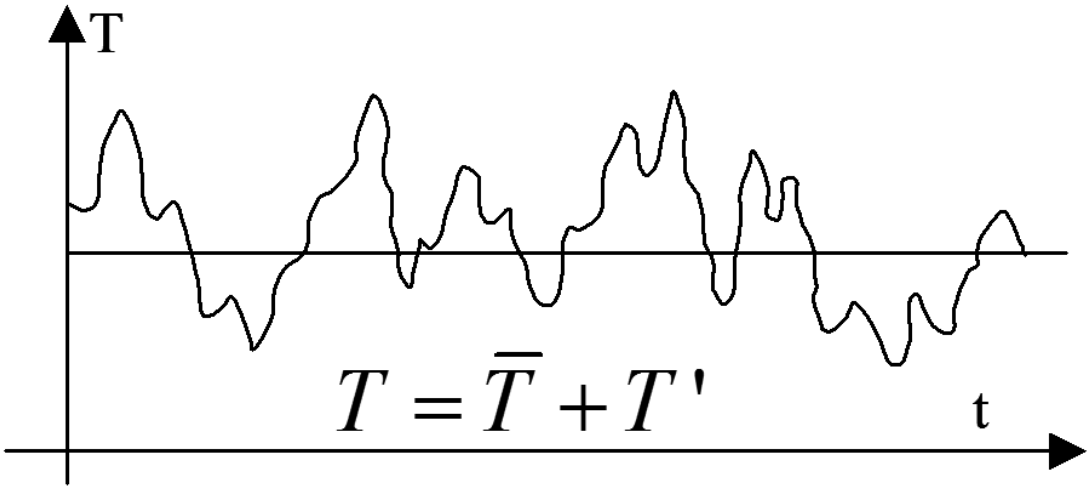

Figure 5.2 *Temperature fluctuations*

The temperature dependence of reaction rate is described by the Arrhenius expression that has a highly non-linear structure:

$$k(T) = AT^{\beta} \exp\left(-\frac{E}{RT}\right) \tag{5.4}$$

Consequently, it is not appropriate calculating the average speed of the reaction simply using the average temperature. Developing the reaction rate as a Taylor series around the average temperature, we obtain:

$$k\left(\overline{\mathrm{T}} + \mathrm{T}'\right) = \mathrm{k}\left(\overline{\mathrm{T}}\right) + \sum \frac{1}{n!}\frac{\partial^n k}{\partial T^n} T'^n + R_n \tag{5.5}$$

Applying the average operator, we get the corrective coefficient to enforce to the reaction rate, calculated using the average temperature. In the case in which the Taylor series is truncated at the second order:

$$\bar{k} = k\left(\overline{\mathrm{T}}\right)\left(1 + \frac{\beta^2 R^2 - \beta R + 2ER\,\overline{\mathrm{T}}^{-1}(\beta - 1) + E^2\,\overline{\mathrm{T}}^{-2}}{2R^2}\overline{\left(\frac{T'}{T}\right)^2} + \cdots\right) \tag{5.6}$$

It can easily be observed (Figure 5.3) that the effect of temperature fluctuations is significant especially for high activation energies. With the use of this correction term, and pushing up to the eighth order of the Taylor series, it is possible to calculate rate of reaction values with a margin of error of less than 10%, even in the case of very large fluctuations.

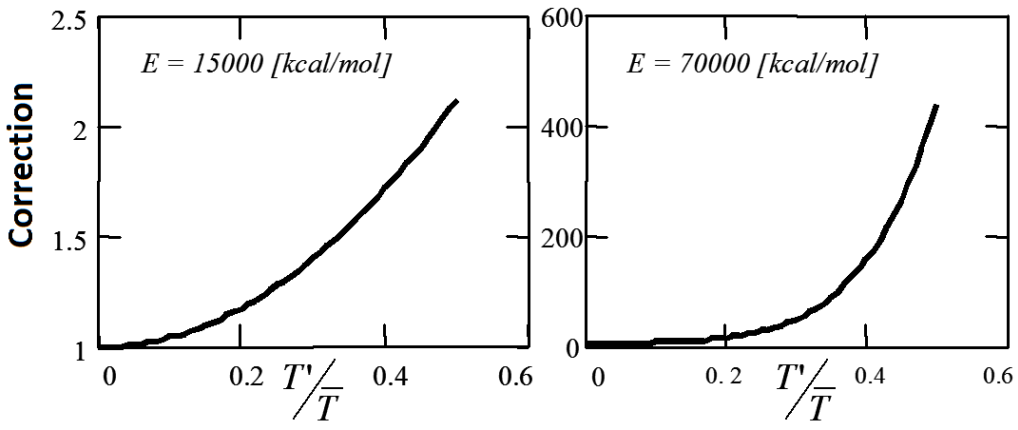

Figure 5.3 *Corrective rate in function of the temperature fluctuations. (T = 1500K, n = 0.3)*

It is necessary, if not directly available from the CFD code, evaluate the intensity of temperature fluctuations. A simple implementation method is based on the assumption of local equilibrium between production and dissipation rates in the equation of temperature variance transport (σ^2), neglecting the convective and diffusive terms [56].

$$\overline{\sigma^2} = \frac{C_1 \mu_t (\nabla \overline{T})^2}{C_2 \bar{\rho} \frac{\bar{\varepsilon}}{\bar{k}}} \tag{5.7}$$

Where:

C_1=2.86 and C_2=2

The use of this simplified expression allows feedback of the temperature fluctuations with a satisfactory agreement with respect to the experimental data, especially when Reynolds numbers are not too high. In addition to the approach that assumes sinusoidal fluctuations, we can use a beta-pdf, a Gaussian or a distribution based on different σ-dirac, all with the same σ.

5.2 KPP parallel version

In the latest years, the recent availability of more computing power due to the large-scale introduction of multiprocessor systems has allowed to manage complex fluid dynamics problems, which would otherwise require an excessive time to reach the desired solution [57].

The introduction of multiprocessor systems has then raised the need of re-thinking problems, in such a way to adapt them to the architecture of the new machines where they were supposed to run. This is why in the past two decades a new communication standard has been created in order to write programs in a parallel way, thus exploiting the possibilities offered by both shared and distributed memory systems. Basically, the creation of such a standard has been driven by three keywords: portability, efficiency and functionality [4].

5.2.1 Performance of a parallel algorithm

The basic purpose of building a parallel program lies in decreasing as much as possible computational times. The achievement of this goal is influenced by several factors, depending on hardware and software used, the degree of parallelizability of the problem and the model adopted to do it. A few concepts are used to quantify the performance of a parallel algorithm.

For example, speedup compares the original algorithm to the one written in a parallel form. It is calculated as:

$$S_p(n) = \frac{t_s(n)}{t_p(n)} \tag{5.8}$$

where, defined p as the number of processors and n as the dimension, $t_s(n)$ is the execution time of the best sequential algorithm, while $t_p(n)$ is the parallel execution time. Theoretically, the maximum attainable speedup is equal to the number of processors used.

The concept of speedup is completed by the analogous of efficiency. It is an index of the efficiency in the use of processors in the parallel algorithm. Mathematically it is expressed as:

$$E_p(n) = \frac{t_s(n)}{p \cdot t_p(n)} = \frac{S_p(n)}{p} \tag{5.9}$$

Of course, if the speedup is linear, efficiency is 100%.

The possibility of decreasing execution times by increasing the number of processors (i.e. the scalability) is first of all influenced by the degree of parallelism of the problem: either small or large, there is anyway a part of the algorithm which must be executed sequentially and will thus be the rate determining step of the algorithm itself.

This is formalized in the so-called Amdahl law [58]: if the fraction of non-parallelizable code is defined as f, the total execution time is given by the sum of the time needed for the sequential part, equal to $f \cdot t_s(n)$, and the time needed for the parallel part, equal to $(1-f)/p \cdot t_s(n)$ (assuming that parallelization efficiency is 100%).

Therefore, the resulting theoretically attainable speedup is:

$$S_p(n) = \frac{1}{f + \frac{1-f}{p}} \tag{5.10}$$

which tends to 1/f whether the number of processors tends to infinite. This trend is graphically expressed below:

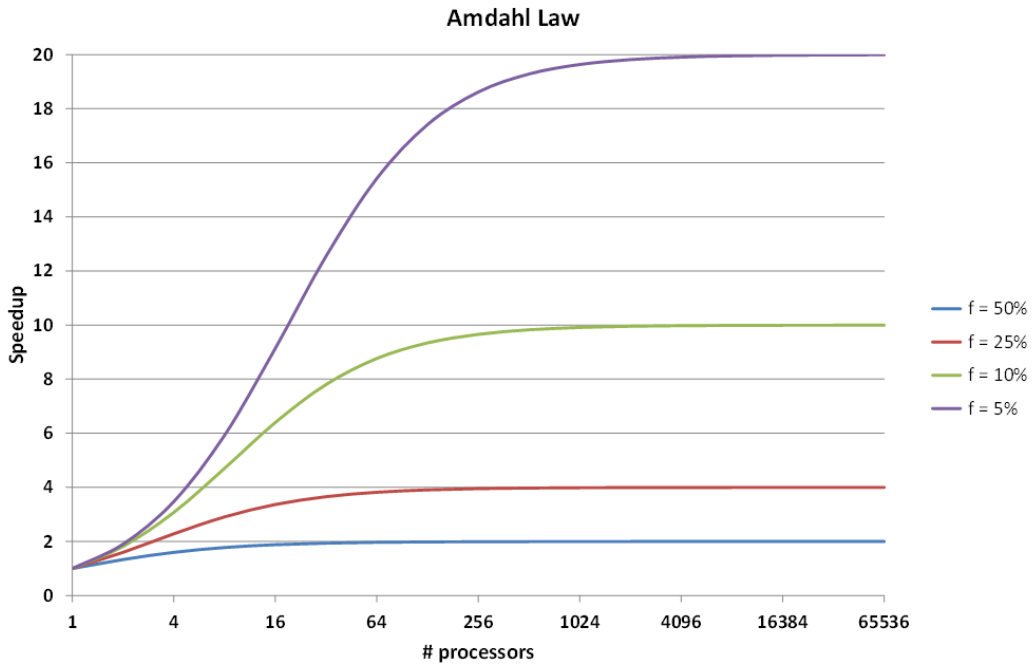

Figure 5.4 *Speedup as predicted by Amdahl law, varying the fraction of non-parallelizable code [4]*

The non-parallelizable part is therefore a key factor, which may strongly influence the performance.

5.2.2 The original KPP: potential and limitations

Basically, the problem faced in the Kinetic Post-Processor is the resolution of a huge non-linear system of "(Number of Species)·(Number of Reactors)" equations in as many unknowns. Its resolution logic, described below in Figure 5.5, is based on an iterative alternation of local and global methods by which the solution is progressively approached [59].

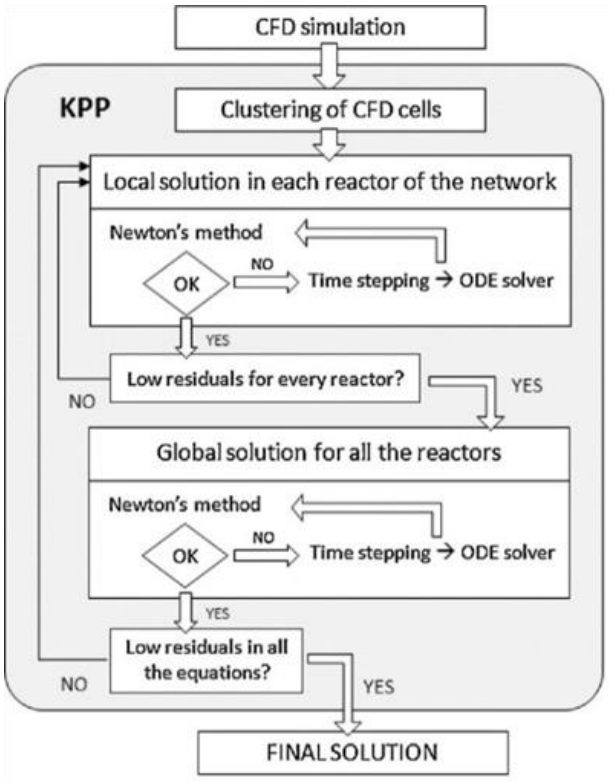

Figure 5.5 *Logic of resolution of the mathematic problem in KPP [51]*

Both methods (local and global) are necessary to find the desired solution: on the one hand, local approaches are essential when residuals are quite high throughout the grid, and therefore global (i.e. Newton) methods would probably fail (as they work well in a sufficiently small neighborhood of the solution); on the other, global methods have the fastest speed of convergence if they converge (Newton's is quadratic).

The limitation in large CFD systems is twofold: on the one hand, the memory required to store a large (though sparse) matrix for the resolution of an ODE or nonlinear system does not allow to solve grids larger than 30000 – 40000 cells with global methods. On the other, matrix factorization requires a computational cost proportional to the cube of the matrix dimension, therefore direct methods become heavier and heavier when increasing the number of cells and/or species.

5.2.3 Parallel approach to resolution methods

One effective technique to work in parallel mode is the master-slave model: in this structure there is a single process (master) which controls the execution of the program, and a variable number of slaves, as it can be seen in Figure 5.6

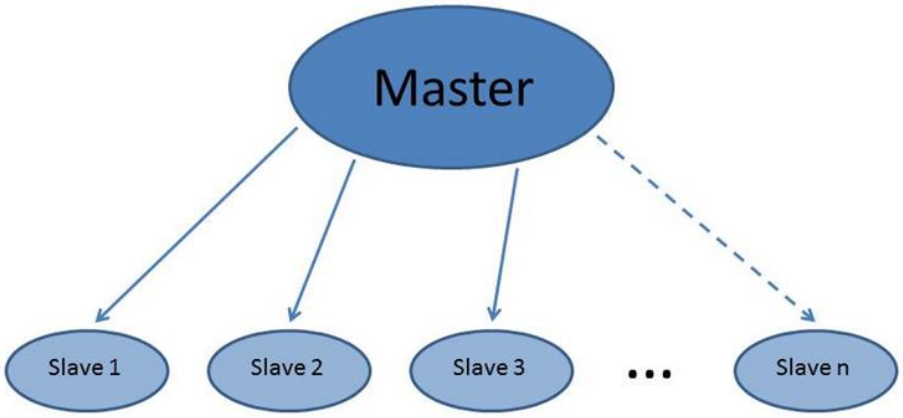

Figure 5.6 *Master-slave model*

In the considered case, the master must split the grid data, and distribute them among the workers. The working principle of this model is quite simple: slaves receive data from master, then they execute the needed computations and finally they send their partial results back to the master.

Basically, Kinetic Post-Processor is a tool able to predict the mass fractions of the different reaction products in a fluid dynamic grid with satisfying accuracy. This is done by applying detailed kinetic schemes to a mesh of reactors, starting from a first guess simulation obtained in CFD codes (i.e. Fluent) by using simplified kinetic schemes; flow and temperature field are imported from the latter and then fixed in post processing. Indeed, many of the produced compounds, not considered in the simplified scheme, are produced in parts per million, so that they do not influence significantly fluid dynamics of the system.

The modeled system is made up of a reactor network: each reactor works like a Perfectly Stirred Reactor (PSR), and then works in the same way, with the same characteristic variables, though in different operating conditions.

Everything is managed by the master process, which sends/receives information to/from slaves.

5.3 KPP set up

Before running the Post-Processor, it is necessary to create the input files using Fluent UDFs (User Defined Functions). Several User Defined Functions need to be compiled to generate a DLL library.

Once the CFD simulation is converged, the “execute on Demand” kinPP function can be executed in Fluent to prepare two input files (CFDNetwork.txt, FirstGuess.txt) processed by the program.

The first file (CFDNetwork.txt) contains information relating to cells of the CFD calculation and to some of variables derived from the CFD solution. These variables are the volume of each cell, its temperature, turbulent diffusivity, temperature fluctuation and exchanger flow rates.

Each cell is identified by a number; it is not required that order is growing.

The structure of this file can be illustrated with a simplified example in which the CFD calculation has been obtained with a simple mesh of 5 cells. The arrows indicate the direction of the mass exchanges obtained hypothetically as CFD solution. There are also input and output flows.

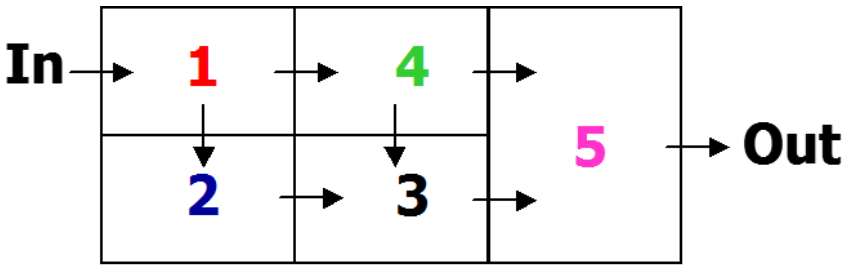

Figure 5.7 Structure of CFDNetwork

You must know which is the order for the chemical species contain within the detailed kinetic scheme that will be used by the Post-Processor. This need to create an appropriate correspondence table.

If a specie, used in the CFD calculation, does not coincide with those of the detailed scheme, for example because it is a pseudo-species used as a surrogate, it will be allocated (respecting the C/H ratio) into two or more species in the scheme.

The second file (FirstGuess.txt) is used to provide to the KPP the initial condition based on CFD solution, that typically resolves the dialing field with a less number of species than those contained in the detailed kinetic scheme.

5.4 KPP results

First, it is necessary to perform a clustering for the cases considered, from 3 million to about 100 thousand cells. The clustering is simply a reduction of the total number of cells, required to use the KPP Post-Processor efficiently and to lower the simulation time. Taking the CO production [ppm] as reference, it is possible to observe that the results are not very sensitive even if the number of cells increase from 2 thousand to 130 thousand (Figure 5.8).

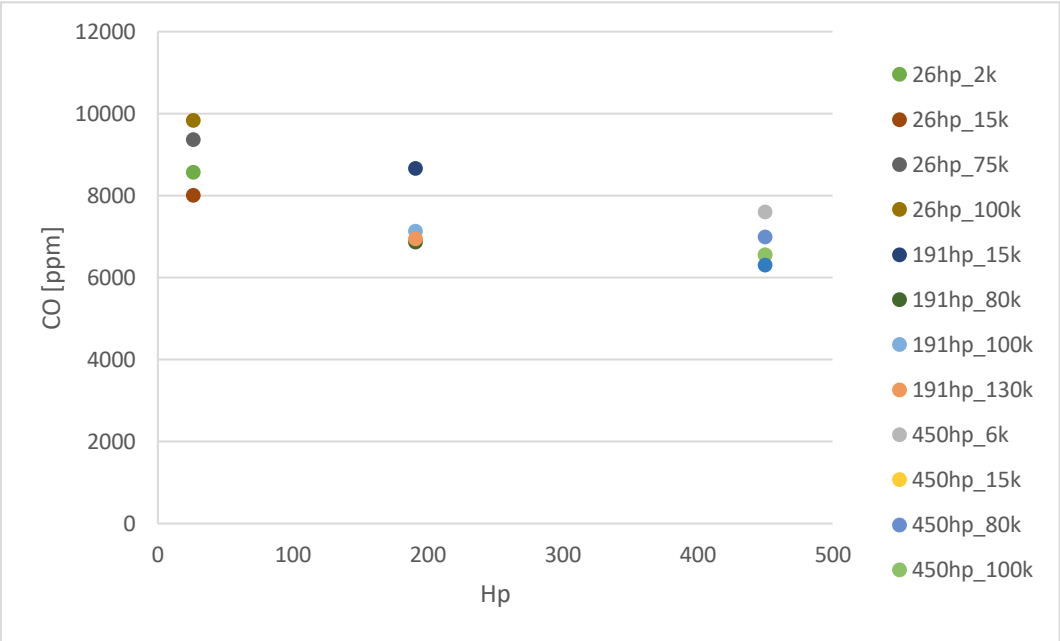

Figure 5.8 *CO [ppm] results obtained with different clustering (from 2 to 130 thousand cells) for 26, 191 and 450 hp*

Considering a constant number of cells (15 thousand) for the 26 hp case, changing the assumption used to evaluate the T-fluctuation, we can notice that, even in this case, the results are not really sensitive (Figure 5.9).

Even if we don't consider any T-fluctuations, due to the low temperature inside the combustion chamber, the results don't change significantly.

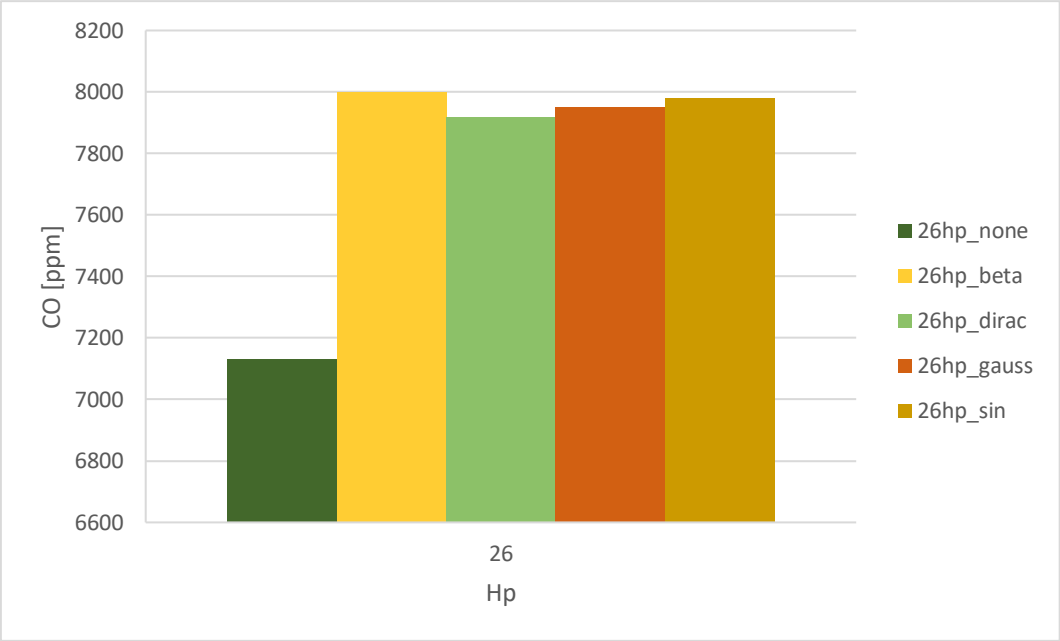

Figure 5.9 *CO [ppm] results obtained with different parameters of correction (none, beta, dirac, gauss and sin) for the 26 hp case clustered at 15 thousand cells*

The results obtained, about CO and unburned hydrocarbons, have been related with the experimental data refers to flights 1735-1736 (see Chapter 3) and reported in the charts below (Figure 5.10a-d).

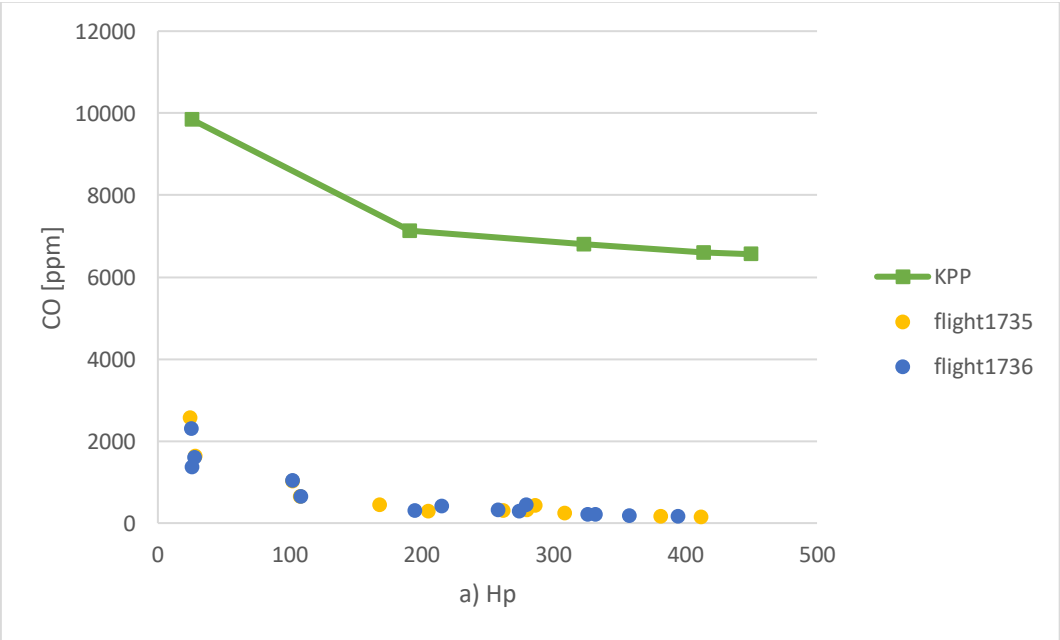

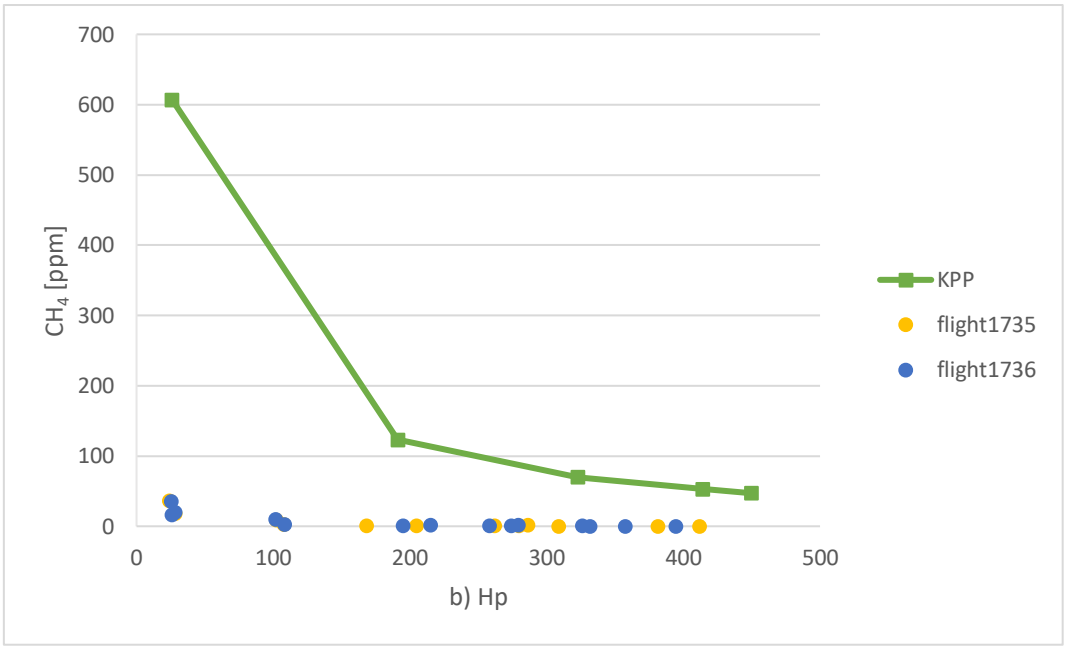
700
600
500
400
300
200
100
0
CH4 [ppm]
0
100
200
300
400
500
b) Hp
KPP
flight1735
flight1736

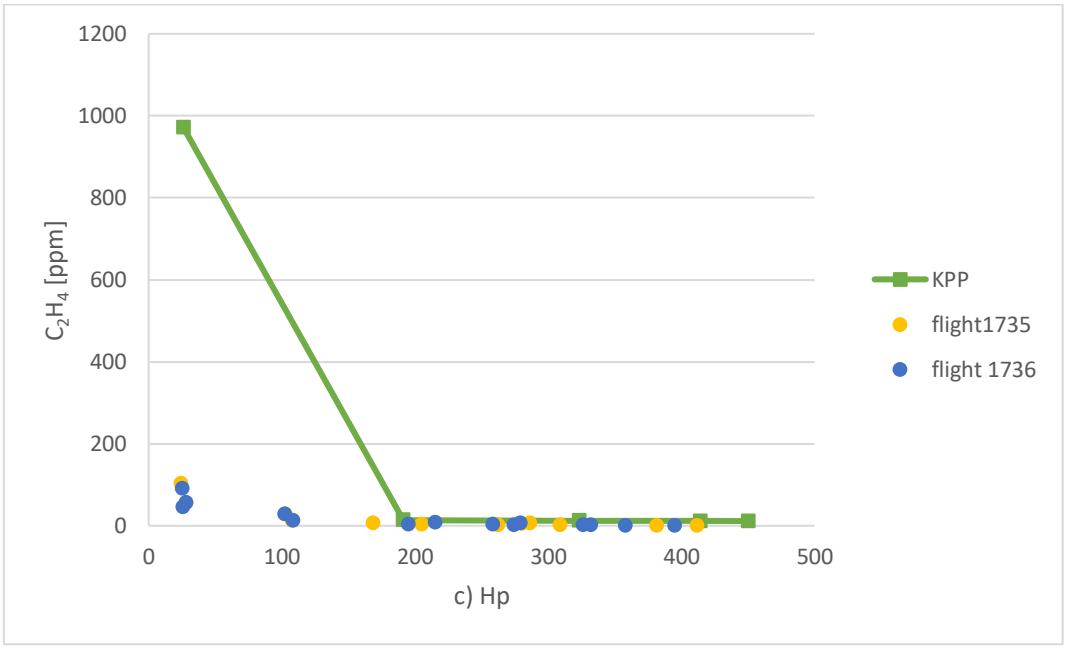
1200
1000
800
600
400
200
0
C2H4 [ppm]
0
100
200
300
400
500
c) Hp
KPP
flight1735
flight 1736

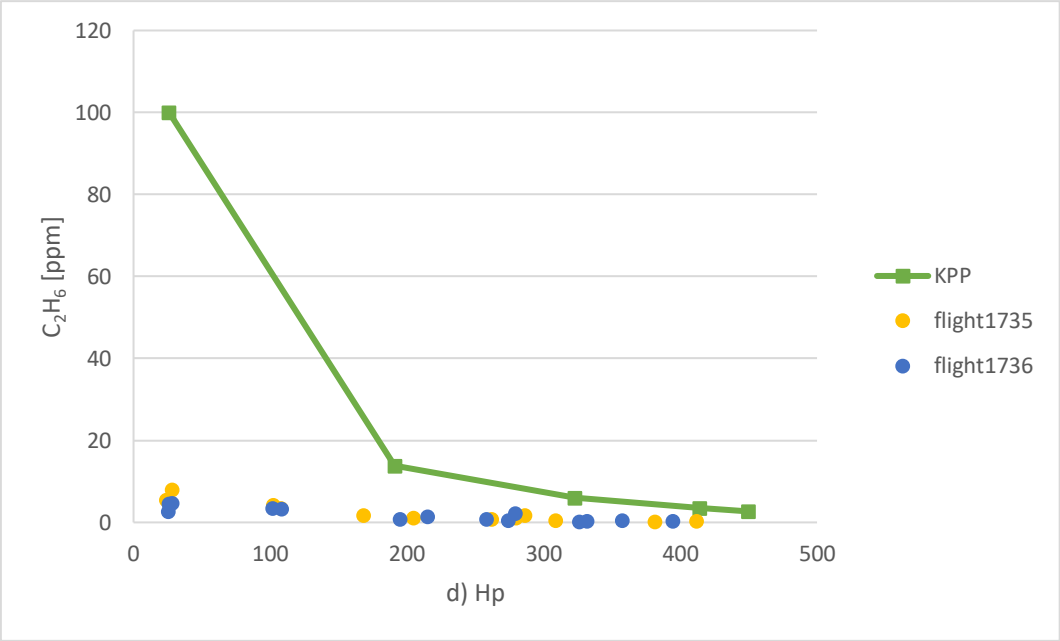

Figure 5.10a-d *Experimental data compared with KPP results. a) CO [ppm] b) CH_4 [ppm] c) C_2H_4 [ppm] d) C_2H_6 [ppm]*

We can notice that, respect to the results obtained using the Fluent Unsteady flamelet (see Chapter 4, paragraphs 4.3.2 and 4.3.3), the shape is good at least. CO and unburned hydrocarbons decrease increasing power with the biggest gap between 20 and 200 hp. Unfortunately, the values obtained are largely overestimated.

A consideration we could do is that at the outlet of the combustor chamber, i.e where the measurements are made, the hypothesis of volume partialization is not more valid due to the relatively low temperatures. The results that we have obtained are shown below (Figure 5.11a-d).

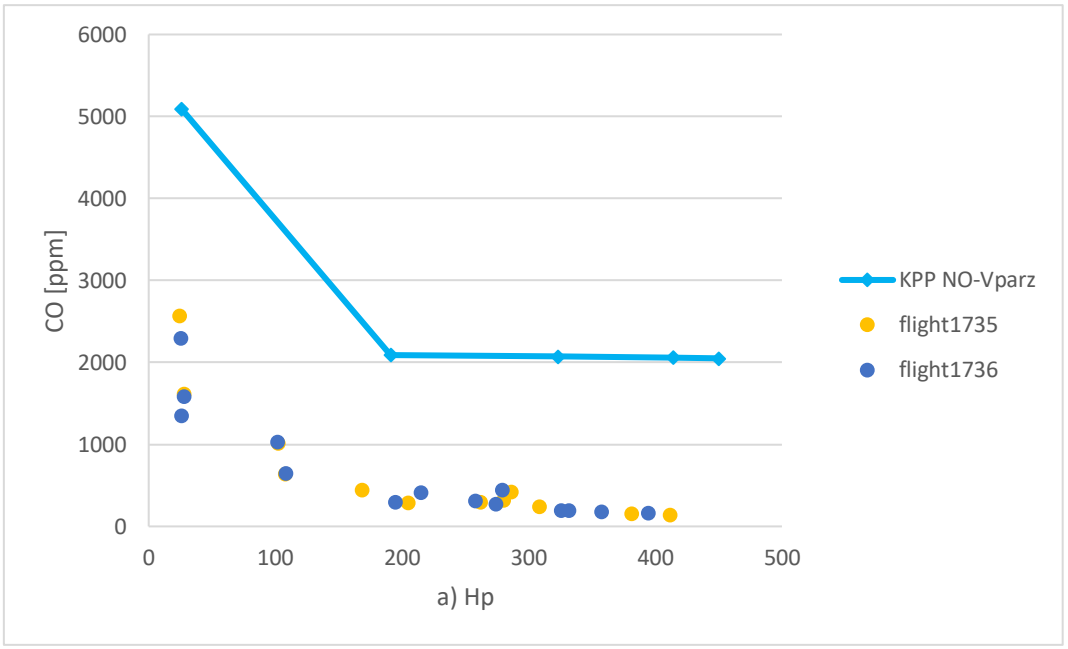
6000
5000
4000
3000
2000
1000
0
CO [ppm]
0
100
200
300
400
500
a) Hp
KPP NO-Vparz
flight1735
flight1736

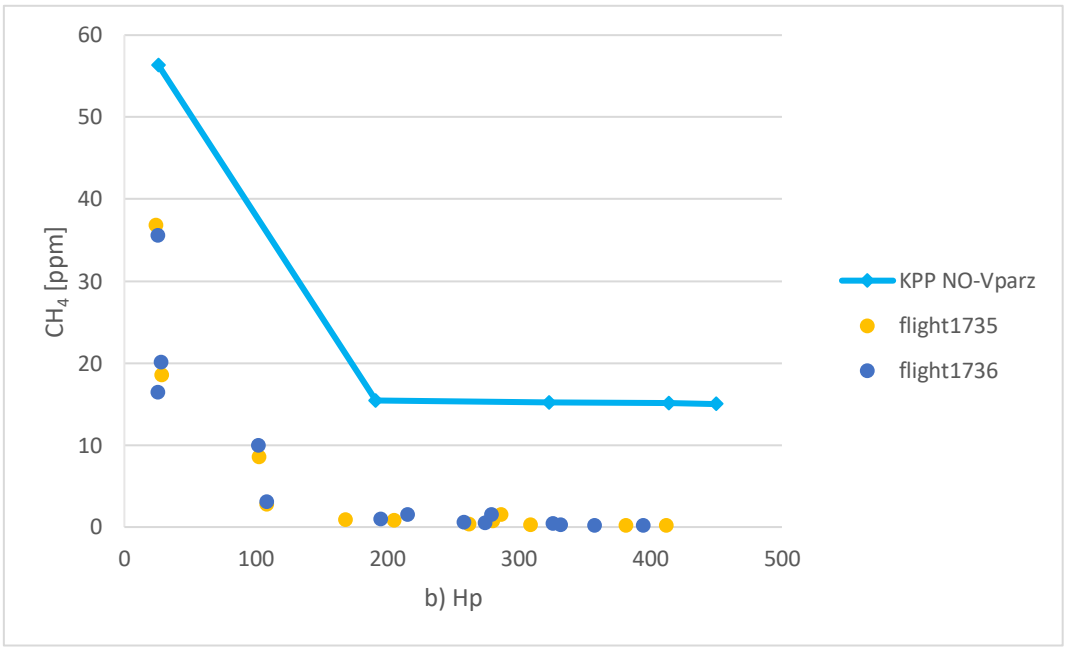
60
50
40
30
20
10
0
CH4 [ppm]
0
100
200
300
400
500
b) Hp
KPP NO-Vparz
flight1735
flight1736

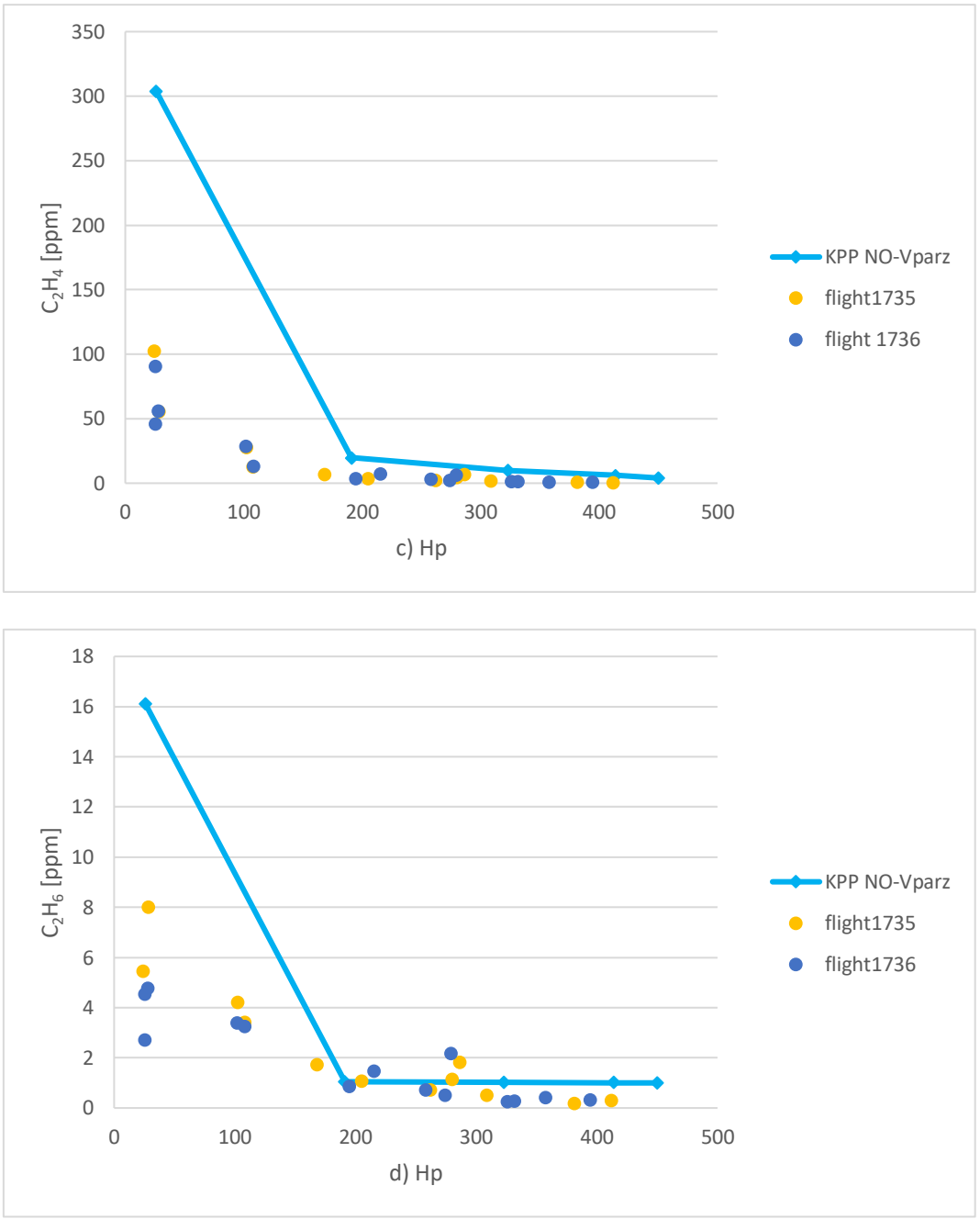

Figure 5.11a-d *Experimental data compared with KPP results (No volume partialization). a) CO [ppm] b) CH_4 [ppm] c) C_2H_4 [ppm] d) C_2H_6 [ppm]*

Improvements are clearly visible, even though especially in the case of CO and CH_4 the results still do not perfectly coincide with the experimental data.

Poor ability to reproduce low-power data (26 hp) can be traced to a certain instability of the flame in these specific conditions because it may be recognized close to extinguishment by the KPP Post-Processor.

About the uncertainty at high powers, it could be caused by a mixture that, given the high temperatures, maintains a certain reactivity. The passage through the turbine could lead to oxidation, especially for CO species, which would decrease the values measured at the exhaust. To better understand the engine framework, see Figure 1.6 in Chapter 1, section 1.2.

A very trivial evaluation has been made by simply creating a batch variable volume and verifying that there is a reduction of the CO, passing from the operating to atmospheric pressure and defining a certain period of time for the occurring expansion. Obviously, this is a simplification of the concept which doesn't take into account of the real presence of the turbine and of the possible cooling done with a fresh air bypass.

The results obtained simply expanding isoentropically the outlet flow for the 450 hp case are reported in Figure 5.12a-c. In this way, the effect of the work done by the gas is not taken into account. For this reason, the temperature remains still quite high. The time necessary to reach the atmospheric pressure has been estimated in 0,07 seconds but, as we can notice in the graph c, it's sufficient 0,01 s to decrease the CO concentration till the experimental data values (about 200 ppm @450 hp).

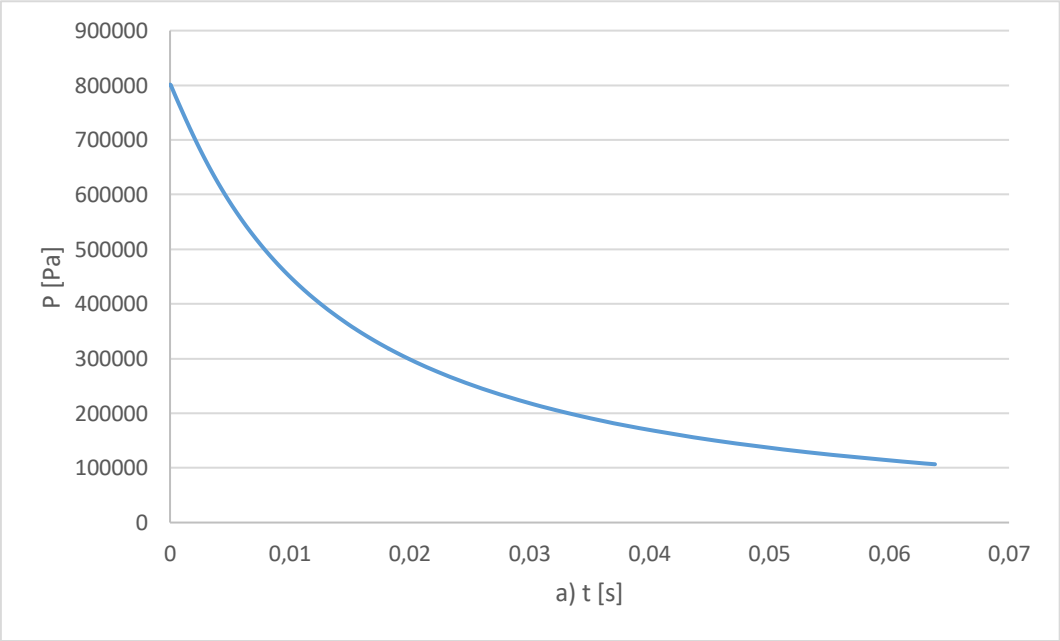

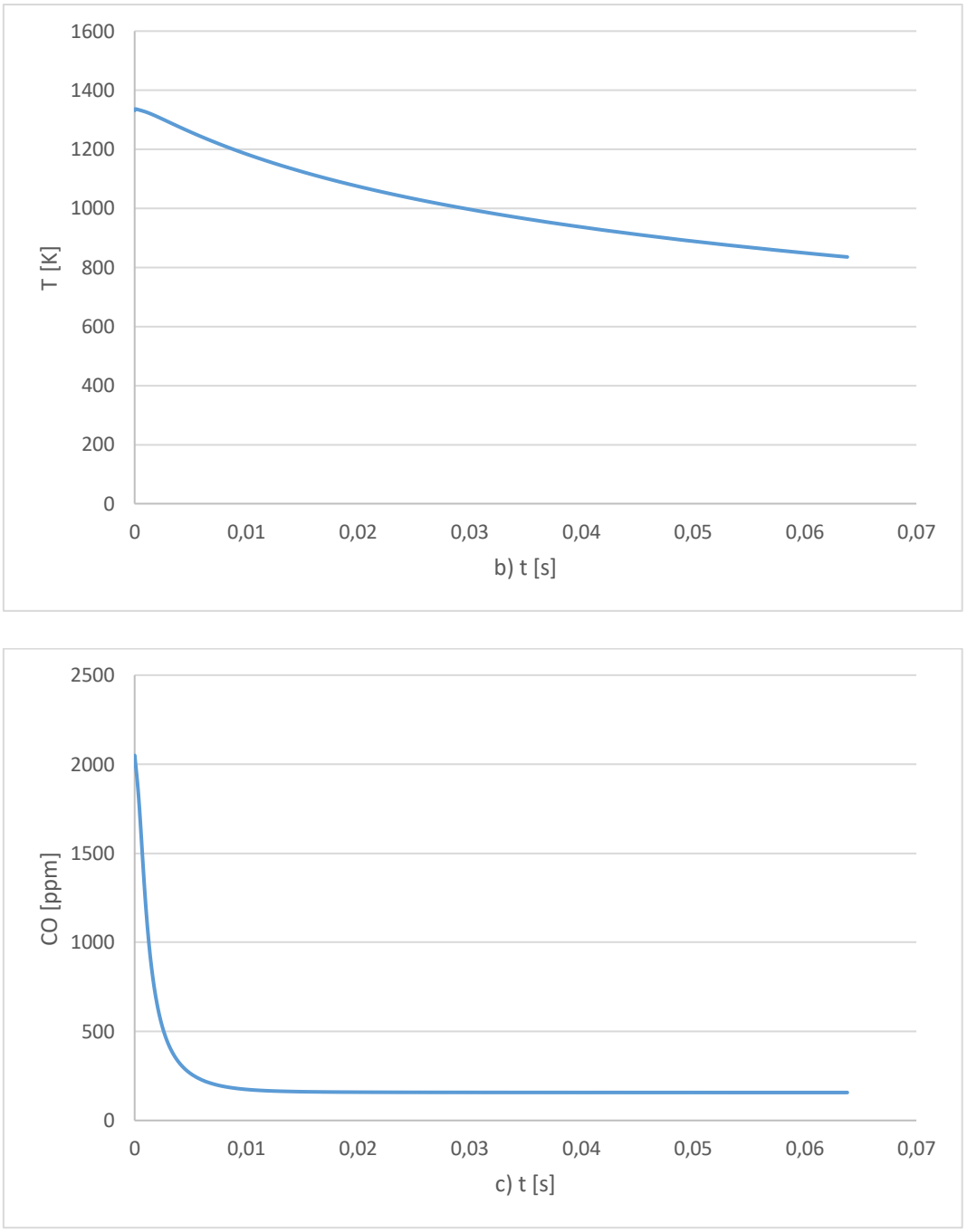

Figure 5.12a-c *Expansion of the outlet flow @450 hp a) pressure decreasing from operating pressure (7.9 atm) to atmospheric pressure b) temperature decreasing c) CO [ppm] variance during expansion*

Keeping constant the time, we can apply this batch simulation to the other powers. The results are reported below (Figure 5.13).

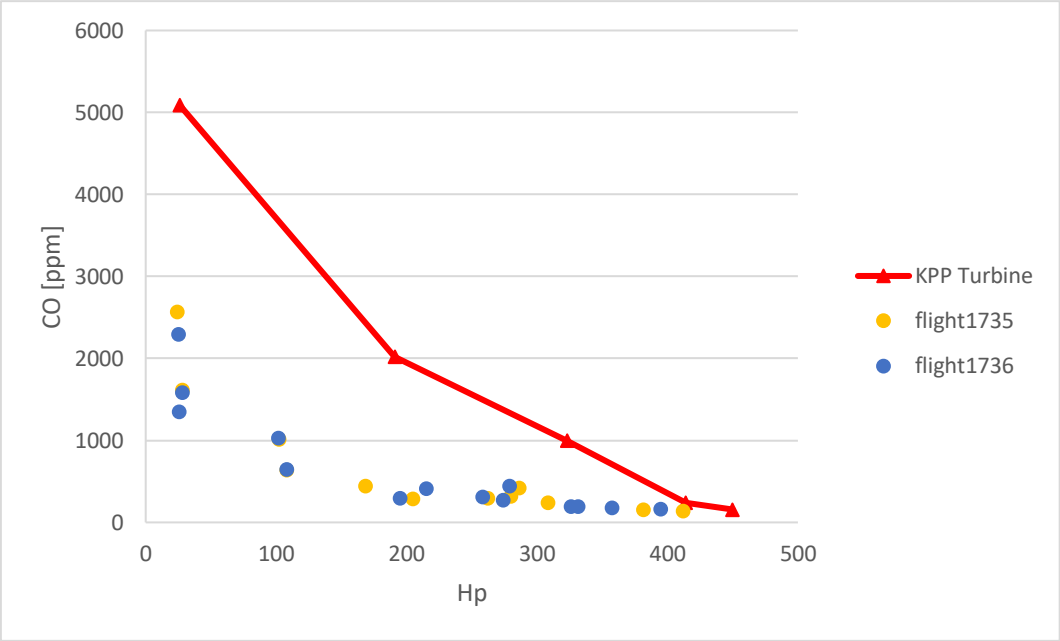

Figure 5.13 *Experimental data compared with batch expansion results for CO [ppm]*

To summarize the work done, we show all the results for CO [ppm] prediction, obtained with different methods, in Figure 5.14 below.

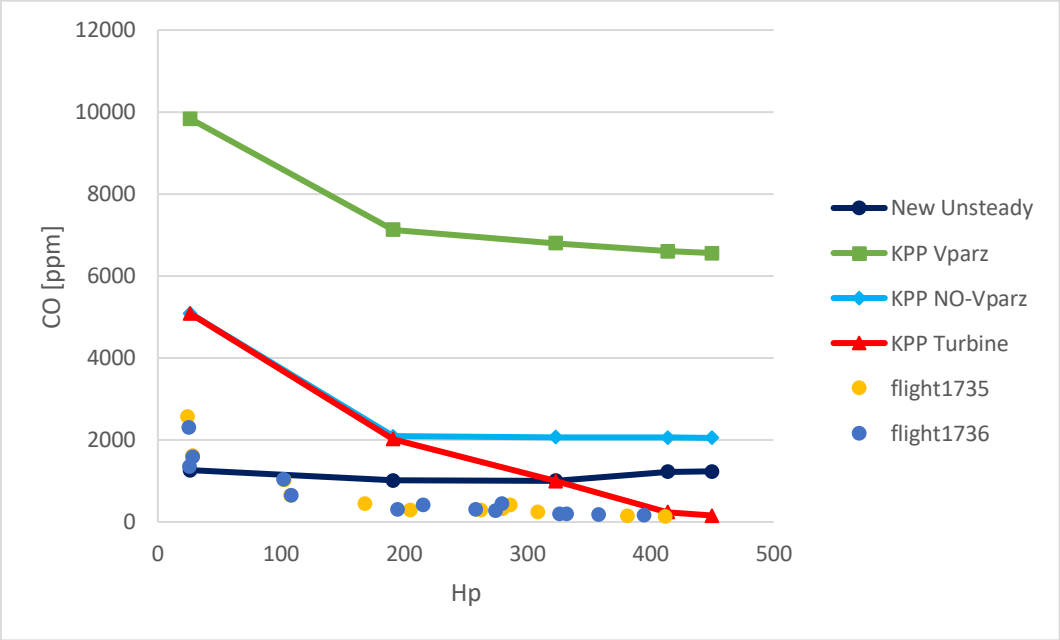

Figure 5.14 *Summary of the results obtained with different methods for CO [ppm] prediction*

Conclusions

The work presented in this thesis has referred to the fluid dynamics simulation of the Allison C20R engine liner.

The work focused on the validation of experimental data using CFD simulation based on Fluent and using a Kinetic Post-Processor (KPP) developed at the Politecnico of Milan [52].

Starting from the CAD construction of the liner, through careful choice of simulation parameters, we have obtained a model able to predict results very close to the experimental data with general improvements compared to the Emicopter project [4].

The use of a new surrogate for the reproduction of the chemical characteristics of jet fuel and the use of new boundary conditions, together with a geometry refining, have been the basis of this thesis work.

The Post-Processor tools included in Fluent has proved excellent capability in the case of NO_x prediction while we have had great difficulties for CO and unburned hydrocarbons. This condition has made necessary the use of an alternative Post-Processor (KPP).

The difficulties observed in the prediction of CO and unburned hydrocarbons are probably attributable to turbulent combustion model. The flamelet (both steady and unsteady) approach used in the CFD simulation failed to predict the correct trend of unburned species with engine power. The KPP post processor allowed to predict the correct trend of emissions with engine power, but don't predict the correct absolute values. The results are very sensitive to the approach adopted in the KPP, which uses the EDC model to describe the turbulence-chemistry interactions.

Further improvements could be achieved by advancing new Fluent settings or analyzing more specifically the real impact of the engine turbine. Moreover, a Post-Processor upgrade is under development. The idea is passing from a EDC to a PaSR based KPP, where the chemical time is considered.

The large number of options that Fluent provides, finer mesh and a better refinement of predictive capabilities of the Post-Processor will soon allow users to get results closer to reality, reveling even more the importance of CFD computation.

Symbols

A: area

C_D: drag coefficient

$C_{u,p,v}$: heat capacity

d: particle diameter

D, Dij: mass diffusion coefficient

Da: Damkohler number

D_H: hydraulic diameter

Ea: activation energy

f: mixture fraction

Fd: drag force

h: heat transfer coefficient

H: total enthalpy

I: stress invariants

I: probability marker

j: diffusion flux

k: reaction rate constant

k: thermal conductivity

k, k_c: mass transfer coefficient

L: characteristic linear dimension

m: mass

M_w: molecular weight

Nu: Nusselt number

P: pressure

P_{sat}: saturation pressure

Pr: Prandtl number

q: heat flux

r: particle radius

R: gas law constant

R: reaction rate

Re: Reynolds number

S_{ij}: mean rate of strain tensor

S: convection source

Sc: Schmidt number

Sh: Sherwood number

T: temperature

t: time

u'': root-mean-square of the turbulent velocity fluctuations

ũ: mean velocity

U: free stream velocity

u, v: velocity magnitude

<v>: maximum velocity of the object relative to the fluid

V: volume

x: space dimension

X: mole fraction

y: dimensionless deviation

Y: mass fraction

α: thermal diffusivity

γ: ratio of specific heats

Δ: change in variable, final-initial

ε: turbulent dissipation rate

η, η': rate exponents for reactants/products

θ: radiation temperature

μ: dynamic viscosity

ν: kinematic viscosity

ν, ν': stoichiometric coefficient for reactants/products

ρ: density

σ: surface tension

σ_s: scattering coefficient

σ_t: dinamic turbulent Schmidt number

τ: stress tensor

$\tau_{mix,c}$: time scale

ϕ: equivalence ratio

ϕ: density-weighted species mass fraction

χ: scalar dissipation rate

ω: specific dissipation rate

ω: angular velocity

Ω_{ij}: mean rate of rotation tensor

Ω_D: diffusion collision integral

References

[1] **C. E. Schlumberger**, Air transport alternative fuels annals (2010)

[2] **A. Frassoldati, A. Cuoci, T. Faravelli, A. Ferrante, M. Stachurska, M. Redaelli, L. Riviello**, In-flight validation of rotorcraft emission predictions and low-pollutant mission, 41 st European Rotorcraft Forum (2015)

[3] http://www.icao.int/ENVIRONMENTAL-PROTECTION

[4] EMICOPTER project (CS-GA-2009-251798), Final report (2013)

[5] http://www.wikipedia.org

[6] CTI Reviews, Mechanics and Thermodynamics of propulsion, 2nd edition (2016)

[7] **C. M. Soares**, Gas turbines in simple cycle & combined cycle application

[8] cset.mnsu.edu

[9] http://www.aeronautica.difesa.it

[10] A look back at development of the Model 250 Turbine Engine, Allison convention (2009)

[11] Model 250-C20R, Power for the AgustaWestland A109C, Bell 206B III, MD Helicopters MD500E, MD520N, Kamov Ka-226 and PZL SW-4 (2007)

[12] **S. M. Correa**, Power generation and aeropropulsion gas turbines: From combustion science to combustion technology, Symposium on combustion (1998)

[13**] D. Golden, M. Cerza, D. Myre**, An Experimental study of water Injection into a Rolls-Royce model 250-C20B turboshaft gas turbine, 44th AIAA/ASME/SAE/ASEE Joint propulsion conference & exhibit (2008)

[14] **P.C. Hendrick**, User experience with the Allison 250-C20R/1 turboshaft on the Belgian Army Agusta A109, RTO AVT Symposium, Ottawa, Canada (1999)

[15] **M. J. A. Islin, M. Cerza, P. E. Jenkins**, An experimental study on the effects of Fischer-Tropsch (FT) blends with diesel #2 and JP5 on the performance of a Rolls-Royce model 250-C20B gas turbine engine, Proceedings of ASME Turbo Expo (2010)

[16] Simulation of turbulent flows, Stanford University, Stanford, USA

[17] **S.p E. Jella**, Emissions predictions in turbulent reacting industrial gas turbine combustor flows using RANS and LES methods, Montreal, Quebec, Canada (2008)

[18] http://www.cfd-online.com

[19] **N.G. Wright, G.J. Easom**, Non-linear k–ε turbulence model results for flow over a building at full-scale (2003)

[20] **T.-H. Shih**, A new k-e eddy viscosity model for high Reynolds number turbulent flows, Computers & Fluids (1995)

[21] **V. Yahkot, S. A. Orszag**, Renormalization group analysis of turbulence, Journal of Scientific Computing (1986)

[22] **A. A. Majhool**, Advanced spray and combustion modelling, Manchester University (2011)

[23] http://www.sharcnet.ca

[24] **F. A. Williams**, Combustion theory, Addison-Wisley Publishing Co., London (1985)

[25] **G. I. Barenblatt**, Self-Similarity, and intermediate asymptotics, Consultants Buro, New York (1979)

[26] **P. J. O'Rourke**, Collective drop effects on vaporizing liquid sprays, Princeton University (1981)

[27] **G. I. Taylor**, The shape and acceleration of a drop in a high speed air stream (1963)

[28] **R. D. Reitz**, Mechanisms of atomization processes in high-pressure vaporizing sprays (1987)

[29] **M. W. Lee, J. J. Park, M. Farid, S. Yoon**, Comparison and correction of the drop breakup models for stochastic dilute spray flow, Seoul, South Korea (2012)

[30] **P.J. O'Rourke, F. V. Bracco**, Modelling of drop interaction in thick sprays and comparison with experiment (1980)

[31] **A. B. Liu, D. Mather, R. D. Reitz**, Modelling the effect of drop drag and break up on fuel sprays, International congress and exposition (1993)

[32] **A. Aissa, M. Adelouahaba, A. Noureddine, M. Elganaoui, B. Pateyron**, Ranz and Marshall correlations limits on heat flow between a sphere and its surrounding gas at high temperature (2013)

[33] **C. E. Fontes, R. D. A. Bacchi**, Best practice guidelines for combustion modeling, Atibaia, Brazil

[34] Fluent user manual

[35] **Y. R. Sivathanu, G. M. Faeth**, Generalized state relationships for scalar properties in non-premixed Hydrocarbon/Air flames, Combustion and Flame (1990)

[36] **N. Peters**, Turbulent Combustion, Cambridge University Press (2000)

[37] **L. Wang, H. Pitsch**, Prediction of pollutant emissions from industrial furnaces, San Diego, California, USA (2007)

[38] **E. Bighè**, Simulazione di un combustore aereonautico con codici fluidodinamici FLUENT ed OPENFOAM: analisi dei modelli, Politecnico di Milano (2012)

[39] **M. R. Johnson, R. K. Cheng, L. W. Kostiuk**, Low NO_x production through lean premixed combustion, Alberta, Canada

[40] **R. K. Hanson, S. Salimian**, Survey of rate constants in H/N/O systems (1984)

[41] **G. G. De Soete**, Overall reaction rates of NO and N2 formation from fuel nitrogen, International symposium on combustion (1975)

[42] **F. Backmier, K. H. Eberius, T. Just**, Comb. Sci. Tech (1973)

[43] **P. C. Melte, D. T. Pratt**, Measurement of atomic oxygen and nitrogen oxides in jet stirred combustion, 15th Symposium on combustion (1974)

[44] **S. K. Liew, K. N. C. Bray**, A stretched laminar flamelet model of turbulent non-premixed combustion (1984)

[45] MAEM-RO project, Methodologies and applications of emission measurements on rotorcraft

[46] **C. N. Ng**, CFD simulation of a gas turbine combustor, Carleton Institute for Mechanical and Aerospace Engineering, Canada (2003)

[47] **D. W. Naegeli, L.G. Dodge, M.C. A.**, The effect of fuel properties and atomization on low temperature ignition in gas turbine combustor, Agard (1991)

[48] **H. Bockhorn, A. D'Anna**, A. F. Sarofim, H. Wang, Combustion generated fine carbonaceous particles (2007)

[49] **S. Humer, A. Frassoldati, S. Granata, T. Faravelli, E. Ranzi, R. Seiser, K. Seshadri**, Proc Combust Inst (2007)

[50] **G. Mairinger, A. Frassoldati, A. Cuoci, E. Pucher, K. Seshadr**, Autoignition of jet fuels and surrogates in nonpremixed flows at elevated pressures, College Park, Maryland (2017)

[51] **A. H.Lefebvre**, Gas turbine combustion, Taylor and Francis, Philadelphia (1999)

[52] **A. M. Mellor**, Turbulent-combustion interaction models for practical high intensity combustors, 17th Symposium on combustion (1978)

[53] http://www.creckmodeling.chem.polimi.it

[54] **T. Shimizu, F. A. Williams, A. Frassoldati**, Concentrations of Nitric Oxide in laminar counterflow Methane/Air diffusion flames

[55] **B. F. Magnussen,B. H. Hiertager**, On mathematical modeling of turbulent combustion, 16th Symposium on combustion - The Combustion Institute, Pittsburgh (1976)

[56] **A. Beretta, N. Mancini, F. Podenzani, L. Vigevano**, The influence of the temperature fluctuations variance on NO predictions for a gas flame, Combust. Sci. and Tech (1996)

[57] **J. Slotnick, A. Khodadoust**, CFD Vision 2030 study: A path to revolutionary computational aerosciences (2013)

[58] **G. Amdahl**, Validity of the single processor approach to achieving large-scale computing capabilities, Spring joint computer conference (1967)

[59] **D. Manca**, The solution of very large non-linear algebraic systems. Computers & Chemical Engineering (2009)

Acknowledgements

Desidero innanzitutto ringraziare il Prof. Frassoldati, relatore di questa tesi, per la grande disponibilità e cortesia dimostratemi, e per tutto l'aiuto fornito durante la stesura. Lo ringrazio, insieme al Prof. Faravelli e a tutto il gruppo creck modelling, anche per avermi affidato questa tesi e per, in un certo senso, fatto incontrare e amare il mondo della combustione.

Un ringraziamento ai compagni di studi, per essermi stati vicini in questo lungo percorso di crescita e per aver condiviso momenti che resteranno indelebili: sono stati per me più veri amici che semplici compagni.

Un ringraziamento agli amici di una vita. Quelli che passano gli anni ma loro restano. Quelli che per nominarli tutti mi ci vorrebbe una pagina intera. Quelli che sanno che sto parlando di loro.

Un ringraziamento ai miei ex-compagni di liceo che si sono trasformati nell'appuntamento fisso del venerdì e che sono stati un esempio da seguire durante la mia carriera universitaria. Ex-compagni che, in un caso specifico, sono diventati molto di più.

Infine, desidero ringraziare con affetto i miei genitori e i familiari tutti per il sostegno ed il grande aiuto che mi hanno dato.

Dedico questa tesi alla persona che più di tutte ha creduto al raggiungimento di questo traguardo; dedico questa tesi a mio papà.